The development of a real-time fibre-optic shaft monitor using cross-correlation techniques.

M. L. Everington

A thesis submitted in the partial fulfilment of the requirements of Kingston University for the degree of Doctor of Philosophy

February 2005

Abstract

A review of non-contact rotation measurement techniques has been undertaken. A non-contact sensor utilising optical fibres for the measurement of angular frequency and torsional strain in rotating shafts has been devised and tested. Initially a system was developed capable of measuring angular frequency over a range from 5 Hz to 1000 Hz to a resolution of 1Hz by monitoring variations in the intensity of the reflected light produced by the surface profile of the rotating shaft. Signal processing techniques such as windowing and auto-correlation were investigated in detail and proved beneficial in the reduction of noise thus enhancing the visibility of the peaks in the Fast Fourier Transform (FFT) spectrum. It was found that the best results were obtained using a Hamming window. In order to identify automatically the peak in the Fourier spectrum representing the rotation rate an algorithm was devised that enabled this to be determined when the peak containing the greatest energy was not necessarily that with the lowest frequency.

The addition of a second identical channel enabling data to be collected at a different point along the axis of the shaft allowed the two signals to be cross-correlated and hence changes in the relative phase of the two points deduced. A digital cross-correlation technique was implemented on a PC. From this information torques up to 0.12 Nm have been measured, with a system resolution of 0.02 Nm and a response time of 1.5 seconds.

For my mum and dad.

Acknowledgements

It is so long ago that I started working on this research program that I cannot really remember why. It must have seemed a good idea at the time and Andy Augousti must share some of the responsibility. It is he who has encouraged me throughout with his patience, wisdom and good humour and I must thank him for that. I have learnt a lot about scientific research in general and electronic instrumentation in particular.

All the other people who have taken an interest in my work also require a special thank you: these include my family at home, friends at the rowing club and the wider circle of those involved with the Kingston University Physics Department. The easy going atmosphere surrounding education and science enjoyed by many in the Physics Department has now gone and will be hard to replace.

Table of Contents

Chapter Three

Chapter Four

Chapter Five

Chapter Six

Chapter Seven

Appendices

Chapter 1

Introduction

1.1 Background

The aim of this project has been to develop a real-time, non-contact fibre optic sensor capable of measuring angular velocity, angular acceleration and torsional strain of rotating shafts. The sensor functions through the detection of naturally occurring changes in the level of reflected light caused by blemishes or tarnishing on the shaft surface and variations in the surface texture of the shaft. Initially the reflected light is converted to an electronic signal so that the signal may be sampled, stored and various computational techniques for signal processing applied. The signal processing technique of Fast Fourier Transforms was implemented as a method for determining the angular velocity of the shaft. Cross correlation was used to determine the torsional strain through detecting changes in the relative phase difference of the signals collected at two separate points along the axis of the shaft. Once the torsional strain has been determined the resultant torque on the shaft may be calculated through knowledge of its dimensions and torsional stiffness.

1.2 The need for shaft monitoring

Moral and political pressure is increasing around the world aimed at the protection of our global environment. The main force of this pressure is focused on the reduction of the emission of greenhouse gases through more efficient usage of energy. There are countless machines containing rotating shafts in existence, many involved in transportation and many involved in the power generation industry itself. A small improvement in the machine efficiency would have a significant impact on energy

consumption thus helping to reduce general exhaust emissions and providing savings on fuel costs for the consumers themselves.

The industrial market for torque sensors is already well established [1] and from the list presented in Table 1.1 it can be seen that there are already a wide variety of torque sensors available, with those systems employing strain gauge transducers accounting for the greatest proportion. Gaining a foothold in this mature market might prove difficult and would probably not be profitable unless currently unexploited openings can be identified. It is my belief that a niche exists for a cost-effective instrument capable of being employed in hazardous or inaccessible environments that may be installed without interrupting the normal operation of the machinery.

Traditionally torque sensors have been used in systems for testing motors immediately after manufacture at the factory or in systems for commissioning machinery in its operating environment. Now, with advances in strain measuring transducers and in electronic instrumentation, the continuous monitoring of rotating machinery parameters such as speed and torque can be used to determine the power being transferred and then evaluate the efficiency of the machinery or the process as a whole. The calibration of the performance parameters of the system at various speeds and loads can be used to ensure operation at maximum efficiency by setting benchmarks for detecting the degradation of normal operation. If degradation in performance is detected remedial adjustments to the system may be made and if this has no effect servicing may be planned at a convenient time before system failure occurs. This helps reduces costs through increasing machine availability and performance. Also the frequency of regular shutdowns that are an expensive part of traditional maintenance

Table 1.1 List of commercially available torque sensors

Company	Transducer type	Sensor coupling	Max speed rpm	Max torque N.m	Application
MCRT – Himmelstein	Strain gauge	Rotary transformer	15k	450k	Industrial shafts
MCRT-Himmelstein	Strain gauge	Rotary transformer	15k	5k	Automobile type wheel
MCRT-Himmelstein	Strain gauge	Rotary transformer	15k	113	Belt, chain pulley
MCRT-Himmelstein	Strain gauge, fixed flange reaction	Fixed electrical	10k	300k	Dynamometer
Eaton Lebow	Strain gauge	Slip rings,	24k 8k	170 1352	Motors, dynamometers
Eaton Lebow	Strain gauge	Rotary transformer	27k	255 22600	Motors, dynamometers
Eaton Lebow	Strain gauge, shaft reaction	Fixed electrical	10k		Sprocket, pulley
Eaton Lebow	Strain gauge	Slip ring or rotary transformer	10k 20k	30k	Automobile wheel
Bently Nevada	Strain gauge	FM telemetry	20k 10k	1000 100k	Rotating machinery
Interface	Strain gauge	Rotary transformer	8000 1200	1360 226k	Shafts
GKN Westland Aerospace	Strain gauge	Slip rings	10k 500	20 300k	Shafts, dynamometer
GKN Westland Aerospace	Strain gauge	FM telemetry	25k		Shafts, gearboxes
GKN Westland Aerospace	Strain gauge	FM telemetry	25k		Helicopter
Cooper Instruments	Strain gauge	Slip rings	5k	2260	Shafts
Industrial Measurement Ltd	Strain gauge	Rotary transformer slip rings, telemetry	30k 12k		Steel mills, marine, aero, automotive, petrochemical
Binsfield	Strain gauge	FM telemetry	20k	10k	Shafts
Key Transducers	Strain gauge	Slip rings, rotary transformer	10k 20k	20k 20k	
GSE Inc	Magneto elastic	Sensor fixed on casing	10k	500	Shafts
LEM Instruments	Stator current	Direct from motor			Electrical motor drives
Vibro-meter	Variable, differential transformer	Rotary transformer	50k 10k	20 500(	Shafts, dynamometer
Fast Technology	Embedded magnetic domain	Non-contact	100k	1000	Shafts
Vibrac	Optical grating	Non-contact	10k	100	Rotating machinery
Sensor Technology	Optical grating	Non-contact	20k	10mN-10k	Rotating machinery
Sensor Technology	Surface acoustic waves	Non-contact	50k	200k	General industrial
Torquetronic	Phase shift	N/a	30k	N/a	Aeroengines

regimes may be significantly reduced. There are examples of such systems operating successfully in various industries such as aerospace [2], automotive [3], power generation [4], petrochemical [5] and steel production [6]. Another possible application for such systems is the continuous monitoring of cutting tool wear in drills and lathes [7] giving warning of tool degradation and possible failure. Whilst these examples exist on the whole there does not seem to be any widespread urgency in the industrialised world in moving towards improving efficiency and further government advertising or punitive taxation against energy wastage would seem to be necessary.

The standard transducer used in most industrial applications where torque sensing is required remains the strain gauge. These are cheaper than the alternatives, whilst offering good accuracy and reliability. In the engineering industry there is still a great deal of reluctance to change from the tried and tested and strain gauges are the most common device that people are familiar with. The cost of existing strain gauge systems start at £2500 for a rotary sensor of mid-range load capacity [8] using slip rings for data transmission. Custom built sensors or systems for very high or low load capacities are more expensive. Strain gauge systems using rotary transformers or telemetry to transmit data from the sensor start at about £3500 for set ups with a mid-range load specification [9]. These systems require either the unit to be fitted in line with the drive train or a collar that is anchored to the outside world fixed around the shaft. This means that in most cases the sensor must be considered in the initial design process of the system and once a particular unit has been deployed it is unlikely that it may be re-used elsewhere.

The advantages given by the system that we have developed stem from the use of optical fibres. These include employability in environments that are hazardous in terms of the dangers of explosion or corrosiveness, either to the operators of the system or to the device itself. The optical signals transmitted are not affected by common electromagnetic interference and may be monitored remotely from the safety of a secure control room. However the main benefit is the flexibility of the system in that it may be retrofitted to existing devices without disturbing the operation of the machinery being monitored. This means that major modifications do not have to be made to the machine in order to fit a sensor thus avoiding significant loss of production and meaning that normal running is not affected once the sensor is working in situ. The setting up process is simple as long as the rotating shaft is exposed and the simplicity of the device and components means that the cost of the system is cheaper than the commercially available alternatives.

1.3 Rotation monitors

1.3.1 Velocity sensors

The first recorded forms of rotation controls were used in windmills [10] during the seventeenth century and known as governors. These regulated the gap between the millstone and the bedstone using revolving fly-ball weights whose radius of rotation expanded with increased rotational speed. In the late eighteenth century the Scottish engineer James Watt used this principle to control his steam engines. The rotating balls were linked to a valve that regulated the steam pressure as balls spun outwards or inwards.

One common form of velocity sensor in everyday use is the car speedometer. It is a form of tachometer [11] that measures the rate of rotation of the drive shaft and the

speed of the car is derived from that and knowledge of the diameter of the car tyre. The traditional form of car speedometer consists of a flexible cable that is connected via a gear cog to the drive shaft at one end with a magnet attached to the other. The magnet rotates within a drum producing a magnetic field that tends to rotate the drum. A spring, to which the indicator needle is attached, restrains the drum. Higher shaft rotation rates produce more tension in the spring and therefore produce a greater indication of speed. An electrical version of this idea uses the rotating magnet to induce a voltage that activates a galvanometer that is calibrated to indicate speed. In the most recent models an analogue to digital converter converts the voltage to a numerical value or a bar graph display symbolising the speed.

The following sections, 1.3.1.1 to 1.3.1.5, discuss various commercially available systems that have the capability of monitoring the angular velocity of rotating shafts.

1.3.1.1 Optical sensors

Optical rotational velocity sensors employed in industrial systems require a light source, usually an LED, and a photo-detector. These monitor the passing of reflective spots [12] if operating in a reflective mode or the rate of change of the light signal transmitted through transparent sections in a collar attached to the shaft when operating in transmission mode. Some commercial [13] and experimental [14] set-ups use optical fibres as light guides. Due to the excellent bandwidth of up to 100 MHz for a high speed photodiode speeds of rotation up to 100 kHz can comfortably be detected to a high resolution by these sensors. The systems mentioned above use one reflective marker on the shaft meaning that the measurement can only be updated once per revolution. Limited accuracy results at low speeds or if the speed is varying rapidly.

This could be improved with the addition of more reflective spots on each revolution. A drawback with such assemblies is the necessity of making attachments or modifications to the shaft.

1.3.1.2 Incremental and absolute shaft encoders

Incremental shaft encoders [15] comprise a disc with a ring of alternate transparent and dark segments mounted on a shaft. An LED and a photo-detector are positioned on either side of the ring and a square wave signal is produced as the shaft rotates. Through counting the periods of the signal the angular position and rotational velocity of the shaft may be determined. These devices are widely used in machine tools and printers. Absolute encoders are similar but use a series of binary discs to give a unique code indicating the angular position of the shaft. The absolute encoders are more expensive but are widely used in control applications where accurate knowledge of exact angular position is required. In both forms of encoders consideration must be given to protection of the segment markings if used in damp or dirty environments.

1.3.1.3 Hall-effect devices

Hall-effect devices are commonly used in many industrial shaft monitoring systems, functioning as proximity sensors by detecting the presence of gear cogs or magnets attached to moving parts. They respond to the presence or interruption of magnetic fields by producing either an analogue or digital output proportional to the field strength [16]. Through monitoring the rate of change in the output of the sensor it is simple to determine the speed of rotation of a moving part and the sensors are often mounted in the stator of electric motors to detect the passing of the rotor. Hall-effect sensors are also used in conjunction with strain gauges [17] in proprietary torque

meters providing the data concerning the speed of rotation. Their performance is affected by extremes of temperature and since the effects of vibrations or shaft misalignment may be a problem [12], they must be positioned close to the shaft under observation.

1.3.1.4 Potentiometers

A potentiometer may be formed by attaching a ring of resistive material to the end of a rotating shaft and using a stationary electrical contact as the pointer. As the shaft rotates the resistance between the end of the resistive ring and the contact varies with angular position. From this information the angular position and velocity may be calculated. These are quite cheap devices but limited in accuracy due to difficulties in obtaining a reliable contact and subject to rapid wear between the contact and the resistive material especially at high speeds.

1.3.1.5 Resolvers

Resolvers are a type of rotary transformer [18] that are configured in such a way that the orientation of the shaft is indicated by the degree of coupling between the rotor and the stator. The rotor windings are supplied with a reference ac voltage signal that induces a voltage in the stator windings that varies in amplitude proportionally to the relative angles of the rotor and stator. Electrical contact with the shaft may be made either by slip rings or through a separate inductive connection. Through tracking changes in the relative phase the angular velocity and acceleration of the shaft may be calculated. Industrial applications for resolvers [19] are numerous and include uses in the simulation and testing of avionics equipment, fire control systems, and synchronisation systems. Resolvers are relatively bulky devices that have to be

included in systems from the design stage meaning they are inflexible and not retrofittable.

1.3.2 Torque sensors

There are two main methods of directly detecting the torsional strain present in rotating shafts. One involves the measurement of localised strain over a particular region of the shaft, the other the measurement of the torsional deflection along a given length of shaft. Prior to the late 1950s the measurement of torque was mainly undertaken during the development and testing process by the system designer, their greatest usage being in the aerospace industry [20]. A dynamometer would be used to load the machine and a torque table would mechanically measure the resultant force exerted on the outside world. However, the introduction of reliable strain gauges and associated bonding techniques meant that affordably priced sensors capable of being attached to rotating objects could be introduced into many systems. Apart from strain gauges a variety of other forms of strain measuring transducers have been developed some of which are described in Chapter 2. Those most favoured industrially rely on surface acoustic waves (SAW) [21] or embedded magnetic domain (EMD) [22] detection.

Torsional deflection systems employ sensors monitoring the shaft at different points along the axis of the shaft and calculate the torsional strain from changes in the relative phase of the two signals. These set ups, also known as phase displacement torquemeters, have been experimented with since the 1930s [23]. A system was installed on the liner Queen Mary and torquemeters were used on aeroengines during the Second World War. Rolls Royce developed a reliable system in the 1950s that still forms the basis of those used for testing engines in the aerospace industry [24]. The

system works through measuring the twist between a pair of toothed flanges attached to a shaft of known stiffness. In this case Hall effect sensors produce sinusoidal signals as the teeth pass and electronic circuitry calculates the changes in phase between the two signals. In the system developed in this project the phase displacement principle is used with optical reflections from the rotating shaft providing the signals to be processed.

The main advantage of the torsional deflection systems is that they do not require any contact with the rotating shaft meaning that they are retrofittable and that there is no interference with the normal operation of the machinery. Since the sensors are secured away from the rotating parts this type of system is very reliable, requiring little maintenance, being suited to high-speed operation and capable of withstanding high temperatures. This makes them well suited to condition monitoring of large turbomachinery in the oil, gas and petrochemical industry in addition to their widespread use in the aerospace industry. The disadvantages include limitations to their use at low speeds and poor transient response. Also the initial calibration can be time consuming and for the most accurate a long axial separation is required between the sensors.

Transferring electrical signals to and from rotating machinery has obvious difficulties since direct connections are impossible. Initially rotating torsional strain transducer systems required the use of slip rings to connect the shaft to the outside world. Slip rings wear relatively quickly thus requiring regular maintenance although they are still used in many low speed applications such as the monitoring of machines used to control automatic assembly lines. A number of non-contact methods of communication

have been devised with FM telemetry or rotary transformer systems now commercially available for transmitting the output signal from the transducer to the control unit. These systems are quite expensive compared to slip rings but offer higher speed of operation and require less maintenance. Phase displacement measurement systems avoid the problem of transmitting the signal between the shaft and the outside world altogether since no physical contact with the shaft is required.

1.4 Torque Sensor Market Survey

Table 1.2 shows the estimated worldwide sales of torque sensors between 1991 and 1995 as published by Frost and Sullivan in their report on the overall world sensor market [1]. It can be seen that sales increased steadily over that period but the 1995 figure of $25.2 million represents a very small fraction of the overall sensor market. However, with the cost of sensors decreasing and their reliability improving it would be hoped that as the world economy grows and more legislation is aimed at safety and energy efficiency torque sensor sales could grow more strongly.

Year	Total Revenue ($ millions)
1991	21.0
1992	22.0
1993	23.8
1994	24.0
1995	25.2

Table 1.2 World Market for Torquemeters [1]

Table 1.1 gives a list of various torquemeters available on the market. The list is by no means exhaustive but gives a good representation of the various forms of sensors being advertised in the trade press and on the World Wide Web. It also quotes the maximum

torque rating offered and the maximum operating speed, usually referred to as bandwidth, that the manufacturers offer in their standard list of products. The survey confirms that strain gauge devices are the most prevalent and are used in a variety of applications. Where a company offers systems with both slip ring and non-contact rotary transformer or telemetry connections it may be noted that the non-contact system will have the higher bandwidth. Factors that tend to influence customers in making their choice are cost, familiarity and ease of use.

Sensor Technology Ltd, a company based in Oxfordshire, England, produces both optical grating torque transducers and surface acoustic wave torque transducers [25]. The company maintains that their optical transducers are superior to strain gauge transducers using either slip ring or telemetry transmission due to the optical system offering higher bandwidth and the better frequency response. However the cost of an optical transducer system is up to £5000 and requires a skilled operator so is not competitive compared to a cost of less than £3000 for a similar standard strain gauge system. Their surface acoustic wave systems use telemetry so have good bandwidth and are cheaper in price with comparable performance to that of strain gauge systems and, according to the company, are beginning to be supplied to industrial operators.

So it would appear that in the short to medium term strain gauge transducer based devices will continue to be the industry standard with systems using telemetry or rotary transformer based signal output gradually taking over from slip ring contacts. SAW or EMD transducers may make small inroads into the industrial market and systems such as the Torquetronic phase shift torquemeter will continue to occupy specialist areas such as aero-engine testing.

1.5 Fibre optic sensors

There are two basic categories of fibre-optic sensors, these being extrinsic, also known as hybrid, and intrinsic [26]. Extrinsic fibre-optic sensors use optical fibres to project light onto the object being monitored. The light beam is then modulated in some way dependent on the properties of the object and the light, which may have been reflected from or transmitted through the object, is collected and returned back to a photo-detector for processing. In the case of this project the light beam is modulated by change of intensity; other forms of modification to the beam might include frequency, phase, spectral composition or polarisation. Intrinsic sensors use an optical fibre to transmit light into the region under investigation and the light beam is altered by some physical effect whilst it is still being transmitted within the fibre.

Fibre-optic sensors bring to measurement systems many of the advantages that optical fibre technologies have brought to communications systems. Because the signal bandwidth is high optical fibres allow a huge amount of measurement information to be passed down a single fibre. Optical fibres are made of dielectric material so they are not usually affected by electromagnetic waves that might be present in the sensing environment and cause interference with a traditional electronic sensor. Corrosive or toxic atmospheres that can destroy metallic compounds have minimal impact on optical fibres and fibre optic sensors can operate under conditions of extreme temperature and pressure. Fibre-optic sensors are intrinsically safe in explosive conditions because they do not cause sparks; they are flexible, strong, lightweight, compact and provide the potential for cost savings over traditional electronic or mechanical sensors [26].

Fibre-optic sensors can match or better the performance of most conventional sensors and as well as rotation sensing they may be used to monitor other physical variables including temperature, pressure, liquid level, electrical current, acoustic field and position or proximity. Also there are many instruments employing optical fibres for sensing the chemical and biochemical composition of various substances. Uses in medical diagnosis are expanding where fibre optic sensors are replacing those traditional sensors that involve electrical contact with people due to the fact that they cannot cause electric shocks because of their electrically insulating nature.

The most promising areas for new fibre-optic sensors lie in applications where at the moment no feasible working sensors exist. The main examples of these novel devices are embedded fibre optic sensors where the optical fibres are inserted into a structure during its manufacture and can then be used to monitor various operating parameters during the normal working operation of the structures. These perform important safety control tasks in materials such as concrete or fibreglass composites, which are used mainly in structures like aeroplanes and buildings where public safety is an issue.

1.5.1 Relevance of fibre optic sensors to this application

In the system developed during this project a polished head consisting of two jacketed optical fibres is used. The output signal from an infra red LED is directed down one of the fibres onto the surface of the shaft. The reflected signal is collected by the other optical fibre and transmitted back to a photodiode where the light signal is converted into an analogue electronic signal. This signal is fed into an analogue to digital converter and digitised so that the data values can be stored in sequence in computer memory. The computer then performs the processing algorithms required for

determination of the rotational frequency of the shaft and the torque applied to the shaft.

Considering the potential applications mentioned in the previous section that fibre optic sensors are suited to it can be seen that there are opportunities for a sensor system similar to ours to be deployed in locations such as hazardous environments or areas where electromagnetic interference is a problem. The signal containing the measurement data can be transmitted away from the machine environment to an area with cleaner conditions for processing. Also due to the flexibility of optical fibres shafts can be reached in areas where access is blocked by obstructions. An important advantage is that the system may be retrofitted to the existing machinery without the need to modify or alter the machinery in any way.

1.5.2 Market Survey of Fibre Optic Sensors

The use of optical fibres has not advanced quickly into the sensor market in the way it has taken over the telecommunications market. Fibre-optic sensors are not widely used in proprietary devices or advertised in trade magazines. Whilst some of the benefits of fibre optic sensors mentioned above have helped the market to grow by small amounts over the past decade it has not yet developed into the billion-dollar-a-year industry over-optimistically predicted by some analysts in the late 1980's.

The situations in which fibre optic sensors are employed are usually developed in house to fulfil the needs of specific purposes with their development being motivated because existing sensors do not work well, examples of this being fibre optic strain sensors being embedded in structures such as bridges. Other sensors are being

developed for novel applications now practicable due to the special properties of fibre optics that other materials do not possess. A good example of this is fibre optic gyroscopes. As regards to direct replacements for existing devices widespread industrial acceptance has been limited due to customers being unconvinced that the benefits will be large enough to justify the replacement of tried and trusted equipment. The lack of standardisation or modularity and the costs that small volume productions entail add to this problem. Areas in which they are being introduced most readily are those with hostile or corrosive environments and in locations where electromagnetic discharge is a problem.

Estimates of the size vary widely. The most conservative is Technical Insight [27] according to whom world-wide sales of fibre optic sensors were $122 million in 1988 rising to only $126 million in 1992 and $140 million in 1995. Technical Insight suggests it is unlikely that the figures have improved significantly since then, the main reason for this disappointing lack of growth being the high cost of ancillary equipment such as lasers and detectors. More upbeat are Frost and Sullivan [28] who suggested that the market was valued at $252 million in 1995 and expect it to grow at around 10% per year up to 2002. The main contribution to this figure came from displacement, position and proximity sensors used in the packaging and in the electronics and automotive manufacturing industries. Winn Hardin writing in the SPIE Web OE Report [29] quotes the Japanese Opto-Electronic Industry and Technology Development Association as estimating that the global fibre optic sensor market was worth $920 million in 1994 and he quotes estimates that the market will rise to $5 billion by 2010. The sums given in these surveys were obtained from figures returned by companies contacted by the organisation performing survey. So presumably the

discrepancies arise from how extensive the actual list of companies was and whether the figures relate to actual sales or whether the possible values or costs of systems developed in house were included.

1.6 Overview of thesis

This thesis describes the development and characterisation of the sensor. Chapter 1 has discussed the need for shaft monitoring and given an appraisal of techniques available for torque and rotation measurement and a survey of the commercial market at present. This chapter finished with a brief discussion, and a review, of the market for fibre optic sensors in general. Chapter 2 gives a theoretical background to the scientific and mathematical principles that are most relevant to this work. Chapter 3 gives a more detailed description of the various techniques for rotation measurement and vibrometry with particular emphasis on devices employing fibre optic sensors. Chapter 4 describes the experimental development and characterisation of a device using a single fibre optic sensor for monitoring shaft rotation and the investigation of a range of techniques for signal processing including methods for frequency determination and the extraction of the original signals from a noisy background. Chapter 5 describes the manner in which the system may be extended with the addition of a second identical sensor at a different point along the axis of the rotating shaft so that the two separate signals may be cross-correlated to determine the twist and torque acting on the shaft. The thesis concludes with a summary of the work undertaken, suggestions for future investigation, and an assessment of the future prospects for this approach. References are listed at the end of each chapter.

1.7 References

[1] Technical report: Frost and Sullivan Inc., "Sensor Market Source Book", Frost and Sullivan Inc., Mountain View, CA., 1996.

[2] Product data: GKN Westland Aerospace, "Industrial Torque Measurement System," Aviation Support Division, Isle of Wight, UK, 1996.

[3] Product data: Sensor Development Inc., "Automotive Sensors, transmission evaluations," Michigan, USA, 1998.

[4] B. L. Agrawal, J. A.Demcko, R. G. Farmer, and D. A. Selin, "Shaft torque monitoring using conventional digital fault recorders," *Trans. Power Syst.*, 7, (3), 1211 (1992).

[5] Product data: Indikon Company, "Web deflection system," http://www.indikon.com/webdeflection.stm, Massachusetts, USA, July 2000.

[6] Product data: Industrial Measurements Ltd, "Torque measurement," Derby, UK, 2000.

[7] K. F. Hale and B. E. Jones, "Tool wear and monitoring sensors," *Proceedings of 2nd International Conference COMADEM 90*, Brunel University, July 1990, Chapman and Hall, London.

[8] Reply to product information request: Paul Armstrong, Amber Instruments Ltd, Chesterfield, UK, February 2002.

[9] Product data: Binsfield Engineering Inc, "Binsfield Price List," http://.www.binsfield.com, Maple City, MI, USA, Feb 2002.

[10] Frederick Stokhuyzen "The Dutch Windmill," http://www.tem.nhl.nl/~smits/windmill.htm.

[11] Encyclopedia Britannica on Line, F. Landis, "Tachometer", http://search.ebi.eb.com/ebi/article/0,6101,37605,00.html.

[12] Ahmed Bebn Sasi, B. Payne, A. York, Fengshou Gu, A. Ball, "Condition Monitoring of Electric Motors Using Instantaneous Angular Speed," *Proceedings of the 5th Annual Maintenance and Reliability Conference (MARCON 2001),* Galtinburg, Tenessee, USA, May 2001.

[13] Product Information: Bently Nevada Corporation, "Transducer Systems," Minden, Nevada, USA, March 1992.

[14] G. C. Madzer, "A fibre optic sensor for non-contact measurement of shaft speed, torque and power," LEW-15099, National Technical Information Center, Springfield, VA, 1992.

[15] Product information: US Digital Corporation, Optical Encoders, http://www.usdigital.com/, Vancouver, WA, USA, February 2002.

[16] Product information: Honeywell Inc., "Active Speed and Position Sensors for Engine Management," http://content.honeywell.com/sensing/prodinfo/auto/engine_man.asp, February 2002.

[17] Product data: Lebow Products, "Load Cell and Torque Handbook No. 600A," PO Box 1089, Troy, Michigan, US.

[18] Application Data: R. Zimmerman, "Resolvers as Velocity and Position Encoding Devices," Control Sciences Inc., http://www.csiconverters.com/resolvers.html, Chatsworth, CA, US, February, 2002.

[19] Product data: FT280 Synchro/Resolver Test Set, http://www.fttech.co.uk/ft280.html, F T Technologies Ltd, Middlesex, England, February, 2002.

[20] J.J. Rebeske Jr, "Investigation of a NACA High-Speed Strain-Gauge Torquemeter," *Lewis Flight Propulsion Laboratory, Cleveland, Ohio*, National Advisory Committee for Aeronautics, Washington, USA, January 1950.

[21] Product data: Sensor Technology Ltd, "Raleigh Wave Rotary Torque Transducer," http://www.sensors.co.uk/pdf/TSE2279R.pdf, Banbury, UK, July 2000.

[22] Product data: Fast Technology, "Embedded Magnetic Domain," http://www.fast-sensors.com/tec/works.htm, Livonia, MI, USA, August, 2000.

[23] T. Allen, "Torque Measurement," *Industrial Measurements*, http://www.industrialtechnology.co.uk/torque.htm, September 1995.

[24] Product data: Torquetronic Inc, http://www.tti.rotor.com/, Woodlands, TX, US, February 2002.

[25] Personal correspondence: Tony Ingham, Sensor Technology, 26th March, 2002.

[26] E. Udd, "An Overview of fiber optic sensors," *Review of Sientific Instruments*, 66, (8), p. 4015-4030, 1995.

[27] Technical Insight, "Sensor Market Forecast: Fiber-Optic Sensors," John Wiley and Sons, New York, 1999.

[28] Press release: Frost & Sullivan Inc, "Going from Niche Applications to the Main Stream with Fiber Optic Sensors," www.frost.com/verity/press/industrial/pr531932.htm, March 11, 1997.

[29] R. Winn Hardin, "Fiber optic sensors seek to prove their utility," *SPIE Web*, www.spie.org/web/oer/october/oct98/fiberop.html, October 1978

Chapter 2

Theoretical Background

2.1 Light propagation at optical boundaries

The nature of this project involves interrogating rotating shafts optically in order to establish their rotational characteristics. This optical interrogation is achieved via the use of optical fibres, which act in this instance as simple light guides, thereby classifying this system as a form of *extrinsic* fibre optic sensor. It is therefore necessary to briefly review the nature of light transmission in optical fibres, leading particularly to a consideration of numerical aperture of the fibre, which affects the amount of light coupled between the sensor and the rotating shaft. The chapter begins with a brief review of the propagation of light in transparent dielectric materials, and goes on to consider the properties of optical waveguides.

2.1.1 Refractive index

The refractive index, n, of a transparent material may be defined as the ratio of the speed of light in a vacuum, c, to the speed of light in that material, v.

$$n = c/v \qquad \text{.....(1)}$$

The speed of light through a material in always slower than in a vacuum so the refractive index is always greater than one. The refractive index varies with the wavelength of the light and wavelength dispersion occurs, for example, when white light is shone through a prism. Also the material may absorb some of the light as it passes through.

At an atomic level the slowing of light as it is transmitted through a material may be thought of as a continuous process of photons being absorbed and emitted as they encounter the atoms of the material. In the space between the atoms the photons travel at *c* but during their interaction with the atoms they are absorbed and near-instantaneously re-emitted causing a delay at each atom which manifests itself as a general slowing in the speed of the photons and consequently the speed of light. The refractive index may be defined as a complex number taking into account the phase of the wave with the imaginary part corresponding to the absorption of the material. The absorption of glass is very small so for our purposes a real refractive index is sufficient.

2.1.2 Geometrical optics

To simplify matters in many situations light may be thought of as rays travelling in the same direction as the flow of energy. This is convenient when considering the macroscopic distribution of light energy but does not predict the behaviour of light when concentrated into small regions of space. However ray theory is useful for describing the properties of most optical systems in an intuitively easy manner.

Thus, using the ray theory approach when light arrives at the boundary of two materials with different refractive indices some of the light may be transmitted across the boundary and some may be reflected at the boundary, as shown in Figure 2.1.

The Laws of Geometrical Optics state that:

(1) The angle of incidence, θ_i, of the light to a line perpendicular to the boundary will be equal to the angle of reflection, θ_r.

$$\theta_i = \theta_r \qquad \text{.....(2)}$$

(2) The angle of the transmitted ray, θ_t, is given by Snell's Law such that:

$$n_i \sin\theta_i = n_t \sin\theta_t \qquad \text{.....(3)}$$

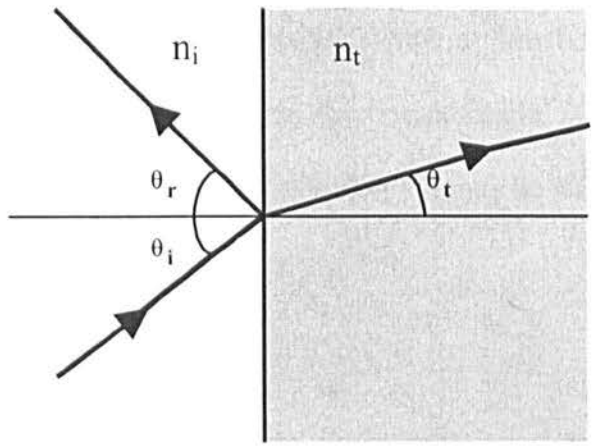

Refractive index $n_t > n_i$

Figure 2.1 Geometry of reflection and refraction

A material whose refractive index is greater than another is described as being optically denser whereas one whose refractive index is less is described as being optically rarer. Light travelling into an optically denser material would be refracted towards the normal whilst light entering an optically rarer material would be refracted away from the normal.

It is possible to rewrite Equation 3 as follows:

$$\sin\theta_i = \frac{n_t}{n_i}.\sin\theta_t \qquad \text{.....(4)}$$

If instead of the case shown in Figure 1 the light were to be travelling from the denser material into the rarer one then $n_i > n_t$. Supposing the angle of incidence were to be increased towards 90^o then to satisfy Equation (4) at some point the sine of the angle

would have to have a physically impossible value of greater than one. This situation is avoided since all of the light is consequently reflected at the boundary with no light being transmitted into the rarer medium and total internal reflection is said to take place. There exists a critical incident angle, less than 90°, at which the refracted beam travels along the boundary. This angle of incidence at which the transmitted ray is refracted along the boundary is known as the critical angle, θ_{crit}, giving an angle of transmission of 90° by definition. Since sin(90°) = 1 it may be written:

$$\sin(\theta_{crit}) = {}^{n_t}\!/_{n_i} \qquad \text{.....(5)}$$

2.1.3 Optical fibres

Optical fibres are transparent, dielectric waveguides capable of transmitting light over long distances relying on internal reflection. Glass is the most common material used in optical fibres but plastic is also used. If a fibre of uniform refractive index were to be used surrounded by air only, then light could be lost at any point where the fibre touched a solid surface or support, or due the presence of dust or other surface contaminants or scratches. To overcome these problems a cylindrical layer of material whose refractive index is lower than the core surrounds the central core of the fibre, and this medium is known as the cladding. The cladding is then coated with a protective jacket. The most common form of optical fibre is known as step-index fibre since the refractive index undergoes a step-change discontinuity at the core-cladding interface. The path of a ray of light down a step index optical fibre with a central core, refractive index n_{core}, and cladding of refractive index n_{cl} is shown in Figure 2.2.

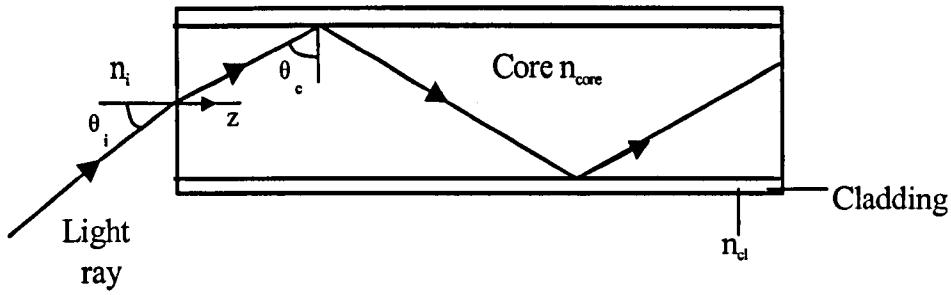

Figure 2.2 Ray reflected within optical fibre

A necessary requirement is that θ_c is equal to or greater than the critical angle, θ_{crit}, so that transmission of the light rays is achieved through internal reflection. Although it may initially appear that the fibre is capable of sustaining all rays incident at an angle greater than the critical angle, this is not in fact the case. This is because an additional requirement exists for constructive interference of the transverse component of the ray. This means that the transverse component of the ray must have the same phase following two transverse transits and two reflections across the fibre. When this second requirement, which is not obvious, and based on the stability of the ray as it travels down the fibre, is considered it then follows that the number of stable paths is limited, sometimes to a single ray. A fibre in which many paths, termed modes, exist is called a *multimode* fibre with the transmission time of each mode depending on θ_i. Rays with greater angles of acceptance have longer path lengths and are internally reflected more often, thus taking a longer time to pass down the fibre than rays that travel along the axis of the fibre. This effect is known as intermodal dispersion, or modal dispersion for short. Consequently the mode angle of propagation will depend upon the wavelength of light and the diameter of the fibre.

Considering Equation 5 and Figure 2.2 it can be seen that the magnitude of the critical angle is determined by the difference in the refractive indices between the core and the cladding. The fractional refractive index difference is given by:

$$\Delta = \frac{(n_{core} - n_{cl})}{n_{core}} \qquad \text{.....(6)}$$

Equation 5 for the critical angle may be used to calculate the angle of the cone of light that will be transmitted along the fibre with a fractional difference Δ. If the ray shown in Figure 2.2 strikes the boundary between the core and cladding at the critical angle, θ_c, and its angle of incidence on the optical fibre is θ_i then from Snell's Law:

$$n_i \sin\theta_i = n_{core} \sin\theta_c = n_{core} \sin(90^o - \theta_{crit}) \text{.....(7)}$$

$$= n_{core} \cos(\theta_{crit}) \qquad \text{.....(8)}$$

$$= n_{core} \sqrt{1 - \sin^2(\theta_{crit})} \qquad \text{.....(9)}$$

From Equation 5 $\sin(\theta_{crit}) = n_{cl}/n_{core}$ so

$$n_i \sin\theta_c = \sqrt{n_{core}^{\ 2} - n_{cl}^{\ 2}} \qquad \text{.....(10)}$$

The numerical aperture, NA, gives a measure of how much light will be accepted by an optical system, in this case an optical fibre. It is defined as the product of the refractive index of the incident medium and the sine of the maximum angle of acceptance that a ray might possess:

$$NA = n_i \sin(\theta_{max}) \qquad \text{.....(11)}$$

Generally the ray will be incident from air so to a good approximation $n_i = 1$. Therefore:

$$NA = \sqrt{n_{core}^{\ 2} - n_{cl}^{\ 2}} \qquad \text{.....(12)}$$

2.1.4 Modes in optical fibres

As mentioned in the previous section, whilst all light waves whose ray direction meets the core-cladding boundary between the critical angle and 90° will initially be caught within the fibre due to internal reflection not all of these waves will propagate down the fibre. The condition for the propagation of a wave along the fibre is that the phase shift of the wave between the points of reflection is an integral number of 2π radians. This may be considered similar to laser cavity resonance with the reflections at the core-cladding boundaries of the fibre causing propagation of the wave in a three-dimensional interference pattern. As the light waves progress down the fibre interference occurs, when it is in phase constructive interference takes place, when it is out of phase it occurs destructively. The result of this is that a standing wave pattern exists along the fibre. As the angle of incidence of a wave changes the path length of the wave between the points of reflection alters thus varying the phase shift present. As this happens the phase shift will be a multiple of 2π for a series of distinct angles of incidence that constitute the permitted modes of propagation for the fibre. Those waves whose angles of incidence are not a multiple of 2π will dissipate due to the destructive interference.

Maxwell's equations govern this process of light propagation with the various modes of the fibre corresponding to the solutions of the equations in cylindrical co-ordinates for the electromagnetic field across the fibre. These solutions, which are harmonic functions in space and time, are of the form

$$E(r,\varphi, z) = f(r).\cos(\omega t - \beta z + \gamma).\cos(q\varphi).....(13)$$

where ω is the angular frequency of the light in radians per second such that $\omega=2\pi\nu$, ν is linear frequency. β is the z component of the wave propagation constant k where

$$k = 2\pi/\lambda_o \qquad \text{.....(14)}$$

λ_o being the wavelength of light in a vacuum. γ is a phase constant that provides the correct amplitude at time t=0 and position z=0, and q is an integer. The solutions show that propagation will occur only those modes for which

$$n_{cl} < \beta < n_{core} \qquad \text{.....,.(15)}$$

The condition $\beta = n_{cl}k$ defines the cut off boundary between the modes that may be transmitted and those that will leak into the cladding for which β is less than $n_{cl}k$.

Light waves may be classified as transverse waves with their electric and magnetic fields both mutually perpendicular to each other and the direction of their propagation. If the component of the electric field along the fibre in the z direction of a given mode is zero, $E_z = 0$, that mode is known as a transverse electric or TE mode. If the component of the magnetic field along the fibre in the z direction of a given mode is zero, $H_z = 0$, that mode is known as a transverse magnetic or TM mode. If both E_z and H_z are non-zero the mode is known as a hybrid mode symbolised by HE or EH depending on whether the magnetic or electric field makes a larger contribution to the transverse field.

The characteristic waveguide parameter or the normalised wavenumber, V, is an important factor in determining the modes that will be supported by a fibre. It is defined as

$$V = k.a.NA = k.a.\sqrt{n_{core}^2 - n_{cl}^2} \qquad \text{.....(16)}$$

where a is the radius of the core and NA the numerical aperture of the fibre. V is a dimensionless quantity that indicates the number of modes that a given fibre will

support for a given wavelength of light. The normalised propagation constant is shown as a function of V for some low order modes in Figure 2.3. The number of modes that will propagate is determined by the number curves that cross a given V value. It can be seen that if V < 2.405 only the HE_{11} mode is in existence. This condition defines a single mode fibre.

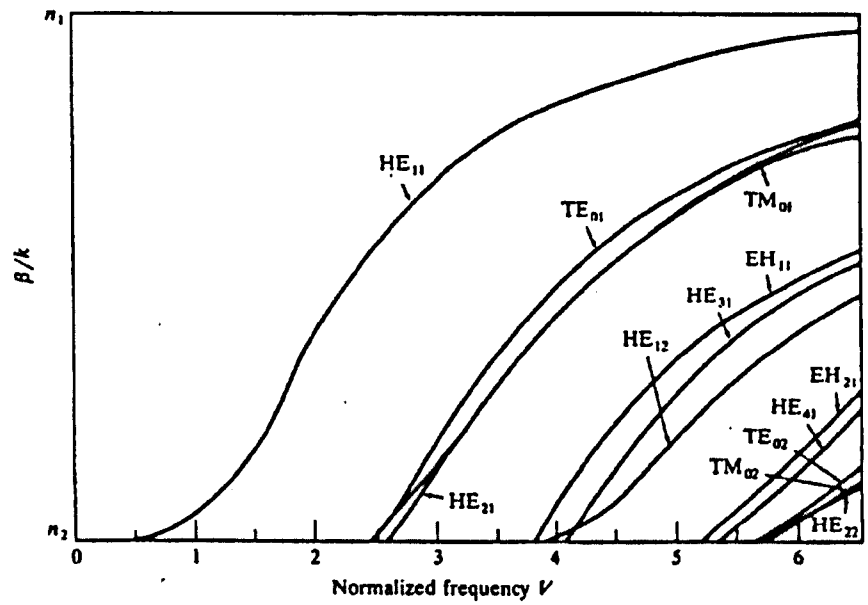

Figure 2.3 Propagation constant as a function of V, from [1]
(n1: core refractive index, n2: cladding refractive index)

During the course of the experimentation carried out for this project, however, in the fibres employed the diameter of the core was always very large compared to the wavelength of the light signal meaning that the V number would be relatively large. This means the existence of a large number of modes so that in this case ray optics offers an adequate description for the propagation of the light through our sensor.

2.1.5 Materials used in optical fibre

The three commonest types of step index fibre are all-glass, plastic-clad silica (PCS), and all-plastic. The all glass fibres have a glass core clad with a glass of slightly lower refractive index. PCS fibres have a silica glass core clad with plastic cladding and all-plastic fibres have a plastic core clad with another plastic. The range of refractive indices available is higher for plastics than glass meaning that it is possible to fabricate plastic and PCS fibres with higher NA than that of glass fibres. However the dispersion effects and pulse spreading in glass fibres are normally lower than those in PCS fibres. The losses associated with plastic fibres are generally higher than those of glass or PCS fibres.

Due to their superior transmission characteristics, with attenuations of less than 0.5 dB/km at wavelengths around 1400nm, all glass fibres are chosen for optical communication systems covering distances greater than a few hundred metres. PCS fibres would be used over shorter distances because their higher NA gives a higher source coupling efficiency. The high propagation losses associated with all-plastic fibres limit their use to lengths of a few metres but their large cores and potentially high NA make them suitable for optical sensors due to their high coupling efficiency.

2.2 Signal Processing

As this project progressed the main focus of the work undertaken shifted rapidly from the development of the electronic instrumentation associated with the sensor onto the development and application of the signal processing algorithms to be applied to the signals obtained by the sensor. These algorithms concentrated on the determination of the frequency, and methods of improving the clarity of the underlying periodic signals inherent in the data. Therefore a brief description of these algorithms is presented here.

2.2.1 Frequency Determination

The simplest method of frequency determination is that of measuring the interval at which a signal passes through the zero value. This is termed a zero-crossing technique and is extremely simple since it only involves noting the occurrence of successive samples that have opposite algebraic signs. Assuming a pure sinusoidal signal is being analysed, and counting from a given change of sign there will be two changes of sign per period. However, not all signals consist of a single tone. If higher order harmonics, DC offsets from the A/D converter or other sources, and in particular 50 Hz mains hum, are added the distortions may cause the signal to change sign more than twice per period. Therefore methods of spectral analysis were investigated in order to provide a better understanding of the spectral content of the signals obtained from the sensor.

2.2.2 The Fourier series

The use of the Fourier series is an effective method of representing time domain signals in the frequency domain. If a signal, $f(t)$, is periodic it may be represented as the sum of an infinite number of sine and cosine terms plus a constant term. This is known as the Fourier series [1], which may be defined as

$$f(t) = a_o + \sum_{n=1}^{\infty} a_n cos(n\omega_o t) + \sum_{n=1}^{\infty} b_n sin(n\omega_o t) \quad ....(17)$$

$f(t)$ could represent any continuous waveform, for example the output voltage signal from an electronic instrument. t is an independent variable that usually represents time. ω_o is the fundamental angular frequency, also known as the first harmonic, such that $\omega_o = 2\pi / T_p$, which is related to the fundamental frequency, f_o, by the relationship $\omega_o = 2\pi f_o$. T_p is the period of repetition of the waveform.

The coefficients a_o, a_n, and b_n may be calculated from the formulae

$$a_o = \frac{1}{T_p} \int_{-T_p/2}^{T_p/2} f(t)dt \quad .....(18)$$

$$a_n = \frac{2}{T_p} \int_{-T_p/2}^{T_p/2} f(t) cos(n\omega_o t)\, dt \quad .....(19)$$

$$b_n = \frac{2}{T_p} \int_{-T_p/2}^{T_p/2} f(t) sin(n\omega_o t)\, dt \quad .....(20)$$

a_o is a constant representing the average value of $f(t)$ over the duration of one period. This might be a constant dc voltage level superimposed on an oscillating voltage signal. The series of frequencies $n\omega_o$ are known as the higher order harmonics of ω_o. Equation 17 therefore represents an infinite series of sinusoidal and cosinusoidal terms of amplitudes a_n and b_n at the positive harmonic frequencies of $n\omega_o$. Using De Moivre's theorem, which states that $e^{jn\omega_0 t} = \cos(\omega_0 t) + j\sin(\omega_0 t)$, it is possible to express the Fourier series in a more compact form using exponential notation such that

$$f(t) = \sum_{n=-\infty}^{\infty} d_n e^{jn\omega_0 t} \qquad \text{.....(21)}$$

where

$$d_n = \frac{1}{T_p} \int_{-T_p/2}^{T_p/2} f(t)\, e^{-jn\omega_0 t}\, dt \qquad \text{.....(22)}$$

d_n has a complex value, being related to the trigonometric expression by

$$d_n = (a_n^2 + b_n^2)^{1/2} \qquad \text{.....(23)}$$

and

$$\varphi_n = -tan^{-1}(b_n/a_n) \qquad \text{.....(24)}$$

where φ_n is the phase angle of the n^{th} order harmonic, which is derived from the inverse tangent of the ratio of the real and imaginary parts of d_n. Therefore each harmonic order of the waveform is defined through its amplitude and phase angle.

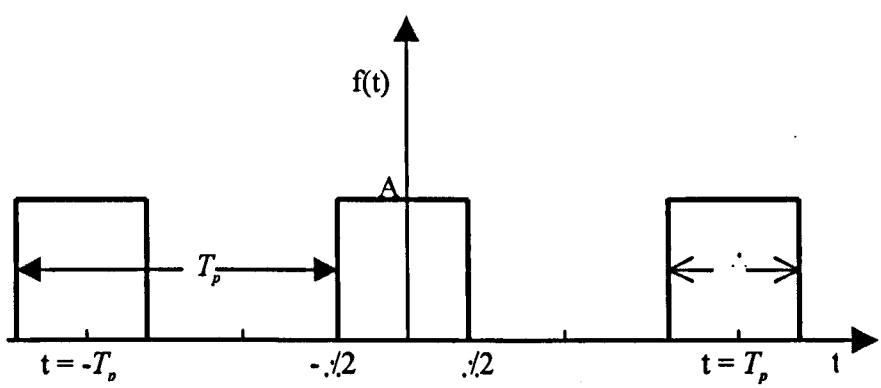

Figure 2.4 Continuous series of periodic square wave pulses

As an example the Fourier coefficients for a rectangular pulse from a periodic series of pulses may be determined. This is a commonly occurring waveform, which, as will be seen later, is of importance to signal processing. A portion of a series of square wave pulses is shown in Figure 2.4. The period of repetition of the waveform is T_p and the pulse width is τ. The Fourier series analysis may be applied as defined by Equation 21

with the Fourier coefficients, d_n, being given by Equation 22. The integration interval is chosen as $-T_p/2$ to $T_p/2$.

Therefore

$$d_n = \frac{1}{T_p}\int_{-T_p/2}^{T_p/2} f(t)e^{-jn\omega_o t}\,dt$$

$$= \frac{A}{T_p}\int_{-T_p/2}^{T_p/2} e^{-jn\omega_o t}\,dt \qquad = \frac{A}{T_p}\left[\frac{e^{-jn\omega_o t}}{-jn\omega_o}\right]_{-\tau/2}^{\tau/2}$$

$$= \frac{A}{n\omega_o T_p}\frac{e^{jn\omega_o\tau/2} - e^{-jn\omega_o\tau/2}}{j} \qquad = \frac{2A\tau}{n\omega_o T_p}\sin\left(\frac{n\omega_o\tau}{2}\right)$$

$$= \frac{2A\tau}{T_p}Sa\left(\frac{n\omega_o\tau}{2}\right) \qquad \text{.....(25)}$$

where $Sa\left(\frac{n\omega_o\tau}{2}\right) = \frac{\sin(n\omega_o\tau/2)}{n\omega_o\tau/2}$. This is known as the sampling function of the argument $n\omega_o\tau/2$, or also as the sinc function, where $sinc(x) = sin(x)/x$.

The effects of varying the duration of the rectangular wave pulse, whilst keeping the frequency of repetition constant, on the Fourier coefficients are shown in Figure 2.5. This shows that the signal power is spread out more over the frequency spectrum as τ decreases. The spacing between the individual spectral lines remains constant independently of τ. Figure 2.6 shows the outcome when T_p is increased whilst τ remains fixed. As T_p is increased the spacing of the spectral lines decreases with their magnitude also decreasing. The general shape of the spectrum does not change with T_p as long as τ is kept constant.

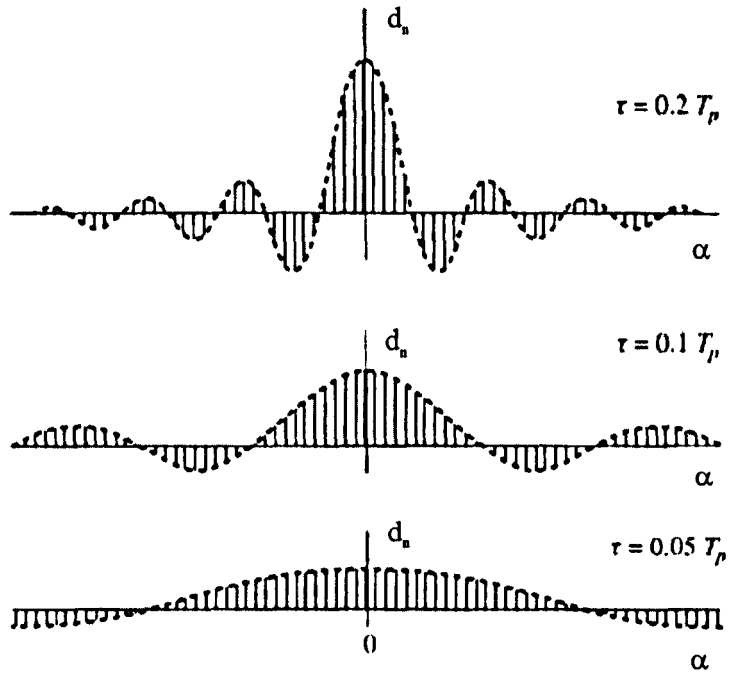

Figure 2.5 Fourier coefficients of series of rectangular pulses when τ is decreased while T_p is kept constant (Adapted from (2))

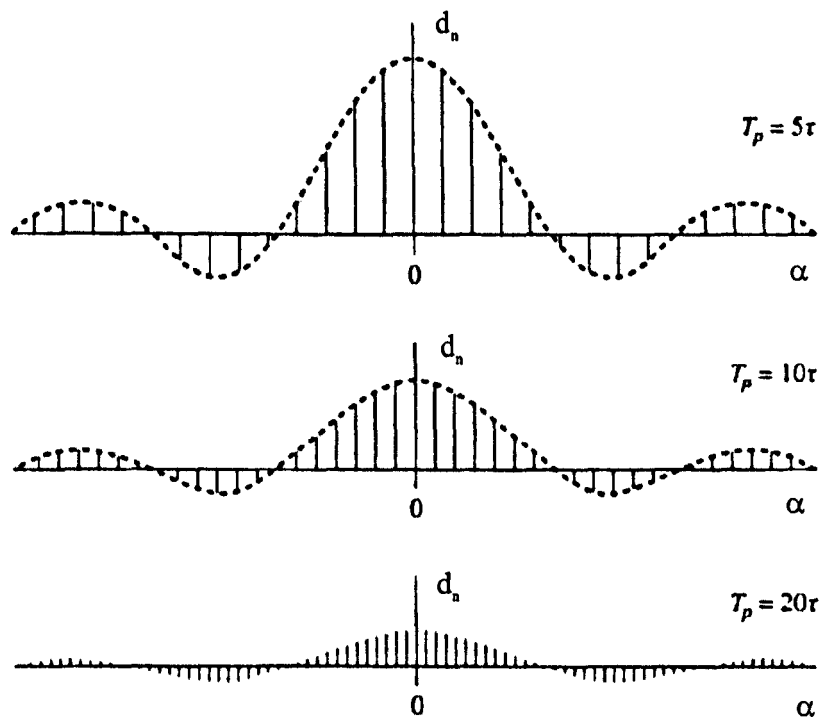

Figure 2.6 Fourier coefficients of series of rectangular pulses with fixed width τ while T_p varies. (Adapted from (2))

The dashed lines shown in Figures 2.5 and 2.6 represent the envelope of the coefficients.

These effects have been demonstrated with reference to a series of square wave pulses but they also generally hold to be true for any arbitrary waveform.

2.2.3 Fourier transforms

As shown in the previous section a periodic signal may be represented by a linear, harmonic series of complex exponentials known as the Fourier series. Due to their periodicity these signals may be decomposed into spectra of equidistant lines in the frequency domain. The spacing between the lines, as shown in Figure 2.6, represents the fundamental frequency of the signal. This is also the inverse of the fundamental period of the waveform, i.e. $1/T_p$. Therefore the fundamental period determines the number of spectral lines per unit of frequency present in the spectral function.

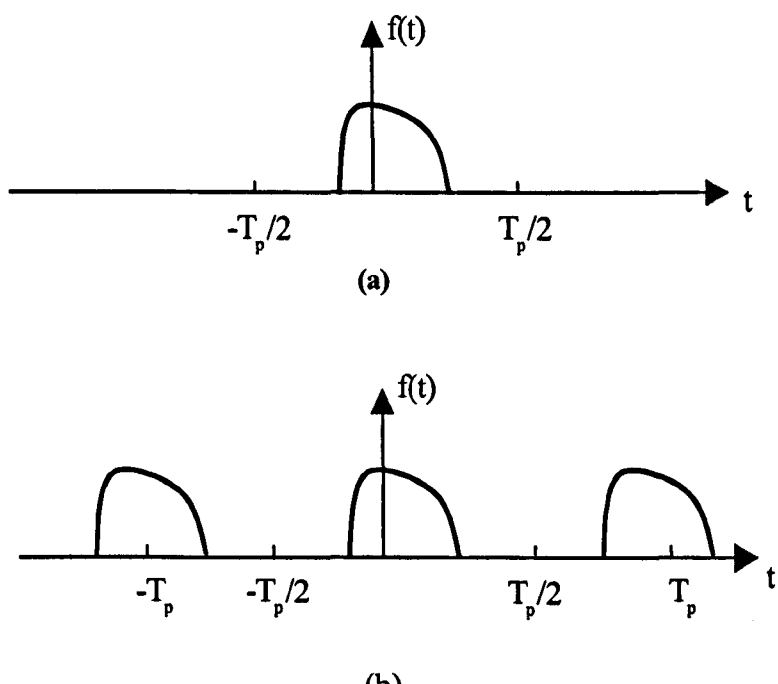

Figure 2.7 (a) Aperiodic waveform, f(t), (b) periodic signal, $f_p(t)$.

The single rectangular pulse waveform, $f(t)$, shown in Figure 2.7(a), is aperiodic. From this a periodic waveform, $f_p(t)$, with period T_p, may be created, as shown in Figure 2.7(b). It may be assumed that at the limit as $T_p \rightarrow \infty$ adjacent pulses virtually never occur and that the periodic function is reduced to a single isolated pulse. As the period is increased towards the limit, the line spacing tends towards zero. When the period reaches infinity, the signal becomes aperiodic and the frequency spectrum becomes a continuous function identical to the envelopes identified earlier. Using this approach the spectra for single pulses or transients may be obtained by allowing the signal to repeat itself with a period T_p and is described mathematically as follows.

If we take the Fourier series expression for $f_p(t)$, then

$$f_p(t) = \sum_{n=-\infty}^{\infty} d_n e^{jn\omega_0 t}, \qquad \omega_o/2\pi = 1/Tp \quad \text{.....(26)}$$

where

$$d_n = \frac{1}{T_p} \int_{-T_p/2}^{T_p/2} f_p(t)\, e^{-jn\omega_0 t}\, dt \quad \text{.....(27)}$$

As T_p becomes very large the spacing between the spectral lines becomes very small. In the limit as $T_p \rightarrow \infty$ it may be written

$$d\omega = \lim_{T_p \rightarrow \infty} \frac{2\pi}{T_p}, \text{ and } \lim_{T_p \rightarrow \infty} f_p(t) = f(t) \quad \text{.....(28)}$$

For the period $-T_p/2 < t < T_p/2$ Equation 27 may therefore be written

$$d_n = \frac{1}{T_p} \int_{-T_p/2}^{T_p/2} f(t)\, e^{-jn\omega_0 t}\, dt \quad \text{.....(29)}$$

The value of $f(t)$ may be defined as zero for times such that $|t| > T_p/2$. Therefore the limits of the integral in Equation 29 may be replaced by ∞ and $-\infty$ giving

$$d_n = \frac{1}{T_p} \int_{-\infty}^{\infty} f(t)\ e^{-jn\omega_0 t}\, dt \qquad \text{.....(30)}$$

As $T_p \rightarrow \infty$ the line spectrum becomes a continuous spectrum and the discrete variable $n\omega_0$ becomes a continuous variableω. In order to overcome the problem of the Fourier series coefficients disappearing as T_p becomes infinitely large a new function $F(\omega)$, known as the *Fourier transform* of $f(t)$ is defined. The value of the coefficients, d_n, are scaled in the following way and a substitution is made into Equation 30 such that $\lim_{T_p \rightarrow \infty} T_p.d_n(n\omega_o) = F(\omega)$. Therefore

$$F(\omega) = \int_{-\infty}^{\infty} f(t)\ e^{-jn\omega_0 t}\, dt \qquad \text{.....(31)}$$

This integral expression may also be written

$$\Im[f(t)] = F(\omega) \qquad \text{.....(32)}$$

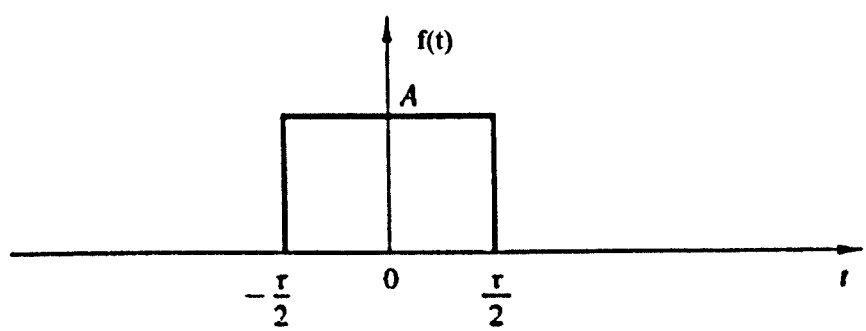

Figure 2.8(a) A rectangular pulse (Diagram taken from(2))

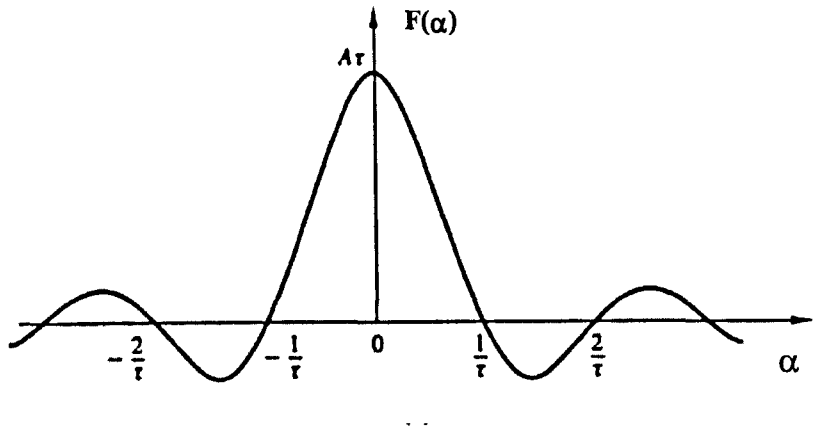

Figure 2.8(b) Fourier transform of (a) (Diagram taken from(2))

Figure 2.8(a) shows a rectangular pulse signal and Figure 2.8(b) shows its Fourier transform, which is recognisable as the shape of a sinc function. The frequency spectrum is the envelope of the Fourier coefficients of the periodically repeated signal at interval T_p as shown in Figure 2.4.

By sampling the continuous variable $F(\omega)$ at increasing multiples of ω_o the Fourier coefficients, d_n, may be obtained. Comparing Equations 30 and 31 it can be seen that

$$d_n = \frac{1}{T_p} F(n\omega_0) \qquad \text{.....(33)}$$

In order to make the return transformation from the frequency domain back to the time domain Equation 28 is again considered for the case where T_p approaches infinity.

$$\lim_{T_p \to \infty} \frac{1}{T_p} = \frac{d\omega}{2\pi} \qquad \text{.....(34)}$$

Equation 26 may be rewritten, $\lim_{T_p \to \infty} f_p(t) = \lim_{T_p \to \infty} \sum_{n=-\infty}^{\infty} d_n \, e^{jn\omega_0 t}$ .....(35)

so that $$f(t) = \frac{1}{2\pi} \int_{-\infty}^{\infty} F(\omega) e^{j\omega t} d\omega \qquad \text{.....(36)}$$

This integral is known as the *Fourier integral* or *inverse Fourier transform*. It may also be written in the form $\Im^{-1}[F(\omega)] = f(t)$ or $F(\omega) \leftrightharpoons f(t)$.

For any function, *f(t)*, a set of conditions known as the *Dirichlet conditions* must be satisfied to guarantee the existence of the Fourier transform *F(t)*. These are

(1) The signal f(t) has a finite number of discontinuities in any finite time interval.

(2) The signal f(t) has a finite number of maxima and minima in any finite time interval.

(3) The signal f(t) is absolutely integral, i.e. $\int_{-\infty}^{\infty}|f(t)|dt<\infty$.

2.2.3.1 Summary

Time domain signals may be represented in the frequency domain using the Fourier series or Fourier transforms. The Fourier series may be employed to obtain the frequency spectra of a periodic signal as a sum of harmonically weighted sinusoidal components, relatively weighted proportionally to the strength of each harmonic. The Fourier transform should be used to characterise the frequency spectra of an aperiodic signal provided it has finite energy.

2.2.4 Frequency analysis of discrete-time signals

Since an ideal analogue waveform contains an infinite number of contiguous points its practical representation is impossible using current computational methods. In practice the waveform must be sampled at regular time intervals by an analogue to digital converter (ADC), converting the analogue level into a binary digital format, which may then be processed by a standard computer or a dedicated digital signal processor (DSP). The rate of sampling of the waveform must be high enough to adequately represent the waveform. This necessary rate is known as the Nyquist rate and equals

$2f_{max}$ where f_{max} is the frequency of the highest frequency component present in the waveform. A version of the Fourier transform exists that is convenient for application by computer and may be used to process finite series of digital data. This is known as the discrete Fourier transform (DFT).

2.2.5 Discrete Fourier transforms

The discrete Fourier transform may be considered to be the equivalent of the continuous time Fourier transform for signals sampled at N points separated by time interval T. This series of data points is therefore finite. If $f(t)$ is the continuous signal from which the data is sampled, then the N samples are denoted $f[0], f[1], f[2],..., f[k],..., f[N-1]$.

The Fourier transform of $f(t)$ is defined as

$$F(\omega) = \int_{-\infty}^{\infty} f(t)\ e^{-j\omega t}\, dt \qquad \text{.....(37)}$$

If each of the samples, $f[k]$, is regarded as a single *impulse* of area $f[k]$, then, since the function only exists at the sample points

$$\begin{aligned} F(\omega) &= \int_{0}^{(N-1)T} f(t)\ e^{-j\omega t}\, dt \\ &= f(0)e^{-j0} + f(1)e^{-j\omega T} + \ldots + f(k)e^{-jk\omega T} + \ldots + f(N-1)e^{-j\omega (N-1)T} \\ &= \sum_{k=0}^{N-1} f(t)e^{-j\omega kT} \qquad \text{.....(38)} \end{aligned}$$

As described previously the Fourier coefficients for a continuous signal may be evaluated over the period $-T_p/2$ *to* $T_p/2$ when the signal is periodic. Since the data exists as a finite series of points, it is treated by the DFT as if it is periodic with the interval $0 < n < N-1$ being the same as the interval $N < n < 2N-1$. Figure 2.9(a) shows a

sequence of eight points that constitutes one period of the periodic sequence depicted in Figure 2.9(b).

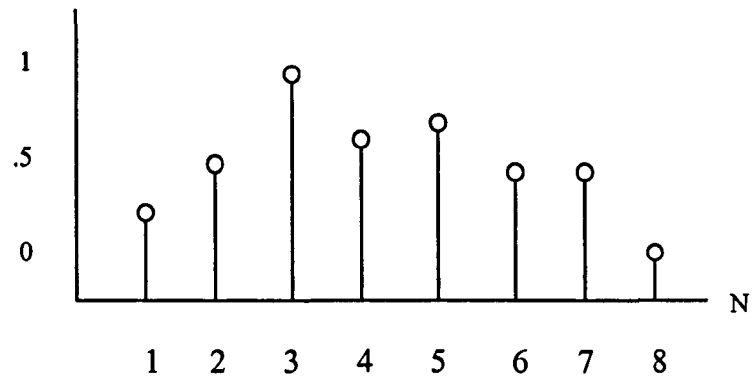

Figure 2.9(a) Data sequence of 8 samples.

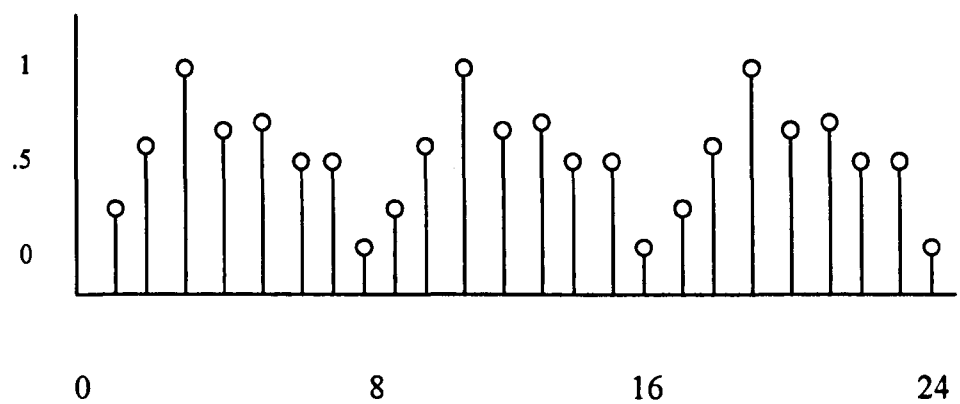

Figure 2.9(b) Data sequence demonstrating the periodicity implied by the data sample shown in Figure 2.9(a).

Since the data is considered to be periodic the DFT coefficients are evaluated at the fundamental frequency of one cycle per sequence, i.e $\frac{1}{NT}$ Hz or $\frac{2\pi}{NT}$ rad/sec, and the higher order harmonics. The d.c. component, or average value of the sequence, where $\omega = 0$ should also be evaluated. Therefore the points at which the frequency spectrum is calculated are

$$\omega = 0,\ \frac{2\pi}{NT},\ \frac{2\pi}{NT}\times 2,\ \ldots\frac{2\pi}{NT}\times n,\ \ldots\frac{2\pi}{NT}\times(N-1).$$

Usually the DFT equation is written in the form

$$F(n)=\sum_{k=0}^{N-1} f[k]e^{-j\frac{2\pi}{N}nk} \qquad 0<n<N-1 \quad \text{.....(39)}$$

where *F(n)* is the discrete Fourier transform of *f[k]*, remembering that k is the index of measurement in the time domain and n is the index of measurement in the frequency domain. To reconstitute the time domain signal from the frequency spectrum the inverse discrete Fourier transform must be used the equation for which is

$$f[k]=\frac{1}{N}\sum_{n=0}^{N-1} F(n)e^{j\frac{2\pi}{N}nk} \qquad 0<k<N-1 \quad \text{.....(40)}$$

2.2.6 Fast Fourier Transforms

The evaluation of the DFT is computationally time intensive due to the large number of multiplications involved. This number is directly proportional to N^2, where N is the length of the sample being transformed. In this application N was chosen to be 1024, in order to allow a good representation of the signal to be obtained, meaning that computational efficiency becomes an important consideration. Algorithms that are highly efficient have been developed that rely on the fact that the DFT includes many redundant calculations. These are known collectively as the Fast Fourier Transform (FFT).

Equation 39 may be rewritten as

$$F(n)=\sum_{k=0}^{N-1} f(k)W_N^{nk} \quad \text{.....(41)}$$

where $W = e^{-j\frac{2\pi}{N}}$. As the summation proceeds various combinations of the indices n and k produce an equal results meaning that some values of W_N^{nk} are calculated more

than once during each computation of a frequency spectrum. Also only N distinct values need to be calculated due to the periodicity of W_N^{nk}. If the case when $N = 8$ is considered, $W_8^0 = 1$ and $W_8^1 = e^{-j\frac{2\pi}{8}} = e^{-j45^\circ} = \frac{1-j}{\sqrt{2}}$

For convenience let $\frac{1-j}{\sqrt{2}} = a$, then $a^2 = -j$, $a^3 = -j\,a = -a^*$, $a^4 = -1$,

$$a^5 = -a, \quad a^6 = j, \quad a^7 = j\,a = a^*, \quad a^8 = 1$$

Thus, it may be seen that

$$W_8^4 = -\,W_8^0$$

$$W_8^5 = -\,W_8^1$$

$$W_8^6 = -\,W_8^2$$

$$W_8^7 = -\,W_8^3$$

As mentioned above if the product nk is not in the range $0 < nk < 7$ one of the above values will still result. For example if $n = 5$ and $k = 7$, then $W_8^{35} = a^{35} = (a^{4x8}).\ a^3 = a^3$.

If Equation 39 is expanded and written in the more convenient matrix form it may be represented as follows

$$\begin{bmatrix} F(0) \\ F(1) \\ F(2) \\ F(3) \\ F(4) \\ F(5) \\ F(6) \\ F(7) \end{bmatrix} = \begin{bmatrix} W_8^0 & W_8^0 & W_8^0 & W_8^0 & W_8^0 & W_8^0 & W_8^0 & W_8^0 \\ W_8^0 & W_8^1 & W_8^2 & W_8^3 & W_8^4 & W_8^5 & W_8^6 & W_8^7 \\ W_8^0 & W_8^2 & W_8^4 & W_8^6 & W_8^8 & W_8^{10} & W_8^{12} & W_8^{14} \\ W_8^0 & W_8^3 & W_8^6 & W_8^9 & W_8^{12} & W_8^{15} & W_8^{18} & W_8^{21} \\ W_8^0 & W_8^4 & W_8^8 & W_8^{12} & W_8^{16} & W_8^{20} & W_8^{24} & W_8^{28} \\ W_8^0 & W_8^5 & W_8^{10} & W_8^{15} & W_8^{20} & W_8^{25} & W_8^{30} & W_8^{35} \\ W_8^0 & W_8^6 & W_8^{12} & W_8^{18} & W_8^{24} & W_8^{30} & W_8^{36} & W_8^{42} \\ W_8^0 & W_8^7 & W_8^{14} & W_8^{21} & W_8^{28} & W_8^{35} & W_8^{42} & W_8^{49} \end{bmatrix} \begin{bmatrix} f(0) \\ f(1) \\ f(2) \\ f(3) \\ f(4) \\ f(5) \\ f(6) \\ f(7) \end{bmatrix}$$

Using the identities that were derived for the W factors the matrix may be simplified as follows. It can be seen that with W^0 always equalling unity and the other three W factors repeated throughout the matrix that clear patterns develop throughout the rows and columns.

$$\begin{bmatrix} F(0) \\ F(1) \\ F(2) \\ F(3) \\ F(4) \\ F(5) \\ F(6) \\ F(7) \end{bmatrix} = \begin{bmatrix} 1 & 1 & 1 & 1 & 1 & 1 & 1 & 1 \\ 1 & W_8^1 & W_8^2 & W_8^3 & -1 & -W_8^1 & -W_8^2 & -W_8^3 \\ 1 & W_8^2 & -1 & -W_8^2 & 1 & W_8^2 & -1 & -W_8^2 \\ 1 & W_8^3 & -W_8^2 & W_8^1 & -1 & -W_8^3 & W_8^2 & -W_8^1 \\ 1 & -1 & 1 & -1 & 1 & -1 & 1 & -1 \\ 1 & -W_8^1 & W_8^2 & -W_8^3 & -1 & W_8^1 & -W_8^2 & W_8^3 \\ 1 & -W_8^2 & -1 & W_8^2 & 1 & -W_8^2 & -1 & W_8^2 \\ 1 & -W_8^3 & -W_8^2 & -W_8^1 & -1 & W_8^3 & W_8^2 & W_8^1 \end{bmatrix} \begin{bmatrix} f(0) \\ f(1) \\ f(2) \\ f(3) \\ f(4) \\ f(5) \\ f(6) \\ f(7) \end{bmatrix}$$

2.2.7 Decimation in time algorithm

In 1965 Cooley and Tukey developed an algorithm [3] that is known as the decimation in time FFT when applied to a series of time domain data. This avoids the computation of the superfluous calculations by taking advantage of the patterns in the equations and functions most efficiently if the size of the data series is an integral power of two. If an N point series of data is split into two sub-series, each with $N/2$ samples and the substitutions $m = k / 2$ when k is even and $m = \frac{k-1}{2}$ when k is odd are made into Equation 25 then

$$F(n) = \sum_{m=0}^{\frac{N}{2}-1} f(2m) W_N^{2mn} + \sum_{m=0}^{\frac{N}{2}-1} f(2m+1) W_N^{(2m+1)n} \quad .(42)$$

Since $W_N^{2mn} = e^{-j\frac{2\pi}{N}(2mn)} = e^{-j\frac{2\pi}{\frac{N}{2}}mn} = W_{\frac{N}{2}}^{mn}$ equation 26 may be written

$$F(n) = \sum_{m=0}^{\frac{N}{2}-1} f(2m) W_{N/2}^{mn} + W_N^m \sum_{m=0}^{\frac{N}{2}-1} f(2m+1) W_{N/2}^{mn} \quad \text{.....(43)}$$

$$F(n) = G(n) + W_N^m H(n) \quad \text{.....(44)}$$

Thus the N point DFT $F(n)$ is obtained from two $N/2$ point transforms, $G(n)$ obtained through transforming the even data samples, $H(n)$ obtained through transforming the odd data samples. For the eight-point transform the calculations for the higher order harmonics may be broken down as follows

$$F(0) = G(0) + W_8^0 H(0)$$

$$F(1) = G(1) + W_8^1 H(1)$$

$$F(2) = G(2) + W_8^2 H(2)$$

$$F(3) = G(3) + W_8^3 H(3)$$

$$F(4) = G(0) + W_8^4 H(0) = G(0) - W_8^0 H(0)$$

$$F(5) = G(1) + W_8^5 H(1) = G(1) - W_8^1 H(1)$$

$$F(6) = G(2) + W_8^6 H(2) = G(2) - W_8^2 H(2)$$

$$F(7) = G(3) + W_8^7 H(3) = G(3) - W_8^3 H(3)$$

This process of dividing each transform sequence into two is then repeated until a series of $N/2$ two point transforms is obtained, these points being taken from the original raw data. This procedure is illustrated in Figure 2.10 with the single $N = 8$ point transform on the right hand side of the diagram and the two $N/2 = 4$ point transforms on the left.

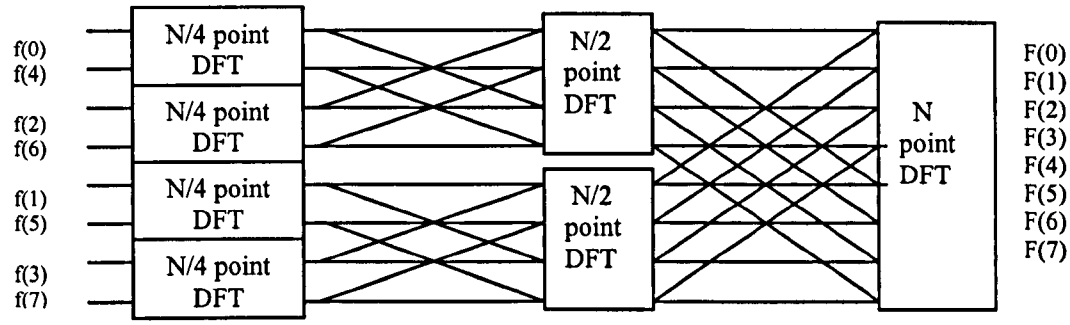

Figure 2.10 DFT flow diagram

The ordering of the sample data is derived as follows. In practice when the FFT algorithm is implemented to produce a frequency spectrum the starting point is the two point transforms. The raw data sequence is reordered into its odd and even halves and the DFT of the pairs of data calculated. Figure 2.11 shows the basis of the computations, as defined in Equation 34, where A and B are complex numbers. Thus each computation involves one complex multiplication and two complex additions and produces two output values.

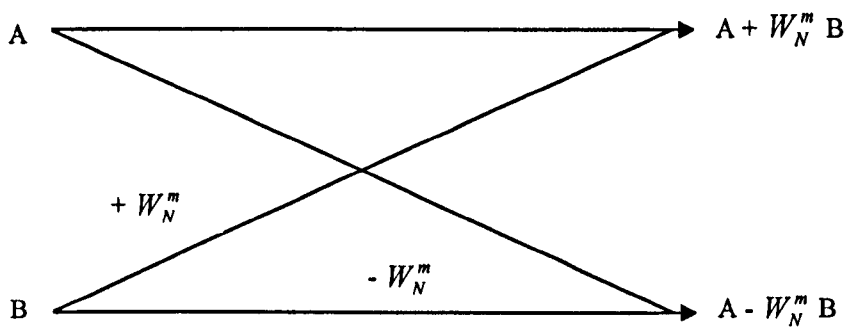

Figure 2.11 Simple two point FFT butterfly computation

The output values of the transform pairs are grouped into sets of four and the DFTs again calculated. This process of doubling up is continued until the final N point transform of Equation 44 is reached as illustrated in Figure 2.10. In the case used in the example where N = 8 three stages of decomposition, or *decimation* as it is known,

would be required to reach the situation where four two point transforms are needed. In general γ stages are required where the total number of points $N = 2^{\gamma}$.

This basic FFT process is known as *decimation-in-time* since it is the input time signals that are being divided up. The equivalent process for the reverse transform from the frequency domain to the time domain is known as *decimation-in-frequency.* The individual calculations that make up the FFT as a whole are known the *butterfly* due to their criss-cross appearance.

The data must be reordered and separated into odd and even groups so that the final output spectrum is in the correct harmonic sequence. A trick for achieving this is to convert the index numbers of the data into binary notation and reverse the order of the binary digits in each number. This is known as "bit-reversed" and is performed at each stage of decimation. By comparing Figure 2.10 with Table 2.1 below it may be seen how reversing the order of the binary digits in the index number of the samples achieves this.

Index (k)	Binary number	Bit-reversed binary	Bit reversed index
0	000	000	0
1	001	100	4
2	010	010	2
3	011	110	6
4	100	001	1
5	101	101	5
6	110	011	3
7	111	111	7

Table 2.1 Illustration of bit reversal process

Care must be taken to ensure that N is a whole number power of two otherwise a three point transform will be required at the end of the computation, thus reducing the efficiency of the transform. If for some reason a series of samples is encountered that does not comply with this then it is possible to pack the data with zeroes at the start and finish edges so that a sample length equalling a whole power of two is obtained.

As mentioned before calculating a DFT spectrum requires N^2 complex calculations. At each stage of decimation of the FFT $N/2$ multiplications are required to produce the transform values for the next stage or the final spectrum. Since there are log_2N stages of decimation the number of calculations required to produce an N point DFT using the FFT algorithm is $N/2 \log_2 N$. Examples of the savings made in terms of the percentage reduction in the number of multiplications that are required when the FFT is used instead of the DFT are shown in Table 2.2 below. As can be seen this is quite significant and increases as the sample size increases.

N	Number of DFT multiplications	Number of FFT multiplications	Percentage saved
8	64	12	84 %
32	1024	80	92 %
256	65536	1024	98.5 %
1024	1048576	5120	99.5 %

Table 2.2 Illustration of the reduction in calculations between DFT and FFT

2.3 Windowing

When a sequence of data points has been obtained through the sampling of a continuous signal, effectively a rectangular window of uniform strength has been placed over a portion of that signal and all values outside the sampled portion are made equal to zero. The sampled data, x(n), represents the product of the original signal, s(n), (over all time) and the magnitude of the window function in time, w(n),

$$x(n) = s(n).w(n) \quad \text{.....(45)}$$

The frequency spectrum produced by the FFT analysis of the sampled data is modified according to the convolution of the Fourier transform of the window and the Fourier transform of the original signal

$$X(n) = \sum_{k=-N}^{N} S(k).W(n-k) \quad \text{.....(46)}$$

where X(n) is the component of the complex DFT spectrum at frequency n, S(k) is the component of the true DFT spectrum at frequency k, and W(n) is the element of the DFT spectrum of the window at frequency n.

The process of sampling with the rectangular window introduces discontinuities at the start and finish in the frequency components whose periods do not exactly fit into the window. When Fourier Transforms are taken the consequence of this is the spectral leakage of the power associated with one frequency into other frequency values. The result of this is that the impulse functions representing the amplitude of a pure harmonic tone are distorted into sampling functions. By altering the weighting of the coefficients of the sampling window the discontinuities can be nullified by tapering the values of the end points towards zero and its Fourier transform can be adapted to gain the most beneficial

and accurate results when the FFT analysis is performed [4]. A number of windows, which incorporate a single or a summation of raised cosine functions, were applied to the data series during processing to determine which had the most beneficial effect on the results. A Hanning window comprising of 64 points is shown in Figure 2.12.

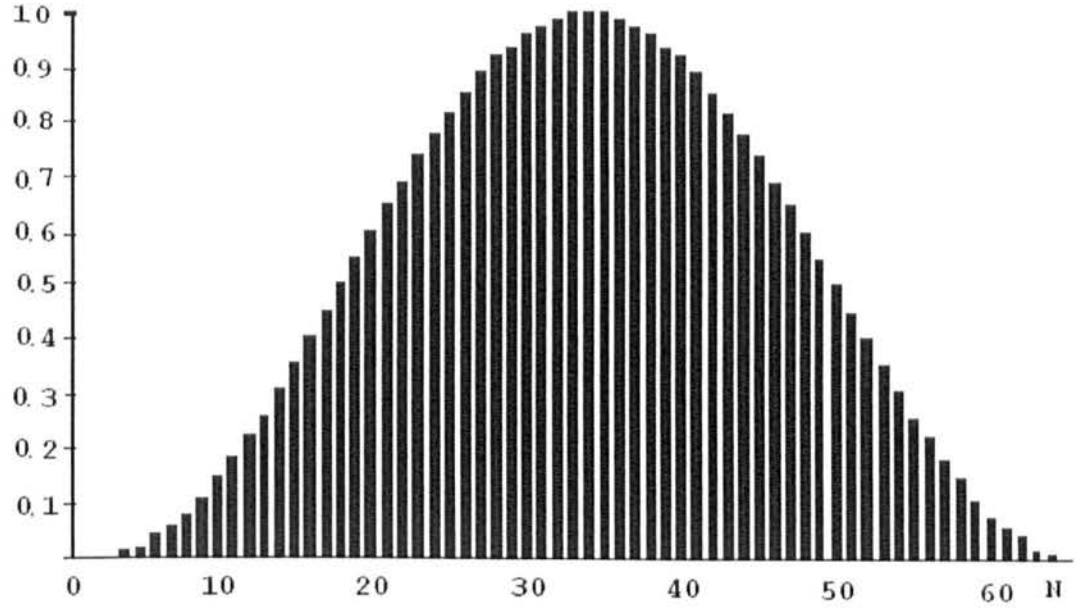

Figure 2.12 64 point Hanning window.

The equation for calculating the Hanning window is:

$$X(n) = \sum_{k=-N}^{N} S(k).W(n-k) \quad \text{.....(47)}$$

As mentioned before, when spectral leakage occurs the infinitely narrow spectral components spread out into sampling functions and the side lobes of these functions that extend into other frequencies may be considered as undesirable noise. The transform of the window in the frequency domain may be considered as a broadband filter and a convenient measure of the amount of leakage is the equivalent noise bandwidth (ENBW)

of the window. This is the width of a rectangular filter with the same peak power gain that passes the same noise power as the window function in question. A good window will have a low noise bandwidth, which is achieved by reducing the side lobe amplitudes. It is possible to compare the amount of spreading caused by different windows through calculating their ENBW.

The processing gain caused by the application of a particular window is defined as the ratio of the signal-to-noise ratio after windowing to the signal to ratio before windowing. This depends upon the shape of the window and is closely linked to the ENBW. The taper reduces the signal power present in the resulting spectrum giving a processing loss, while the presence of the side lobes increases the noise bandwidth. Scalloping loss, or picket fence effect, also has an effect on signal detection. The windowed Fourier Transform may be considered as a series of matched filters that are multiples of the first harmonic component. The frequencies at which these occur are the output points of the spectrum, also known as the transform bins. The scalloping loss is the reduction in processing gain caused through sharing the energy of a frequency component that occurs midway between two bin frequencies between adjacent harmonics. The amplitude density spectrum obtained when a signal with constant spectral density is transformed is illustrated below. As shown in Figure 2.13 it can be seen that the main lobes occurring at the harmonic frequencies have a finite width and that a frequency such as f_{nh} not coinciding with a harmonic multiple cannot be represented directly. This problem may be overcome by careful choice of the sampling frequency. However, when monitoring rotating shafts that have constantly varying speeds of rotation this is not possible. The losses may also be calculated and used to compare different windows.

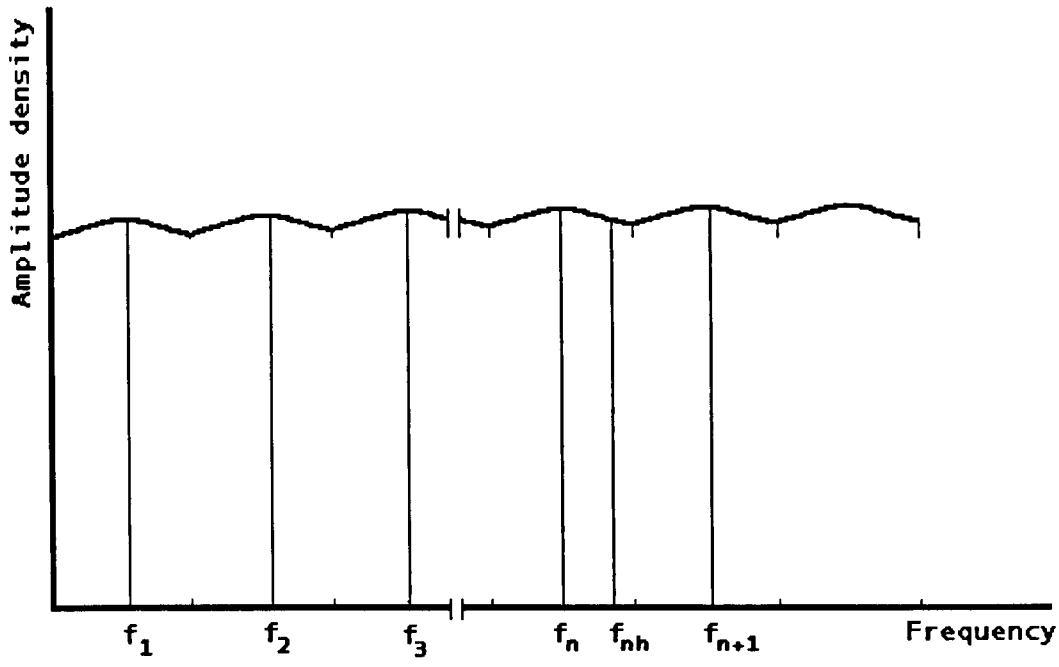

Figure 2.13 The amplitude density spectrum for a signal of constant spectral density

The Hanning window is a member of the $\cos^{\alpha}(X)$ family of windows whose shape depends upon the value of α, where α is normally an integer. α is equal to two in the case of the Hanning window. The benefits of this type of window include the ease of calculation and the ease of predicting the properties of the function in the DFT. As α increases the window becomes smoother, which gives smaller sidelobes but increases the width of the main lobe in the transform.

It is possible to rewrite the Hanning window function as the sum of a number of sequences. This summation may be more easily recognised by considering the DFT of the original function:

$$W(\theta) = 0.5D(\theta) + 0.25\left[D\left(\theta - \frac{2\pi}{N}\right) + D\left(\theta + \frac{2\pi}{N}\right)\right] \quad \text{.....(48)}$$

where:

$$D(\theta) = \exp\left(+j\frac{\theta}{2}\right)\frac{\sin\left[\frac{N}{2}\theta\right]}{\sin\left[\frac{1}{2}\theta\right]} \quad \text{.....(49)}$$

Considering Equations 48 and 49 the 0.5D(θ) term in Equation 48 may be recognised as sampling functions produced by the transform of the constant 0.5 samples and the pair of translated functions those of the single cycle of cosine samples. The translated transform components are centred about the first zero value of the centre function and have half the magnitude of the centre function. Also the sidelobes of the translated functions also have half the magnitude of, and are in opposite phase to, the centre function meaning that when the three functions are summed the side lobe structure tends to be cancelled out. This is illustrated in Figure 2.14. This technique of sidelobe cancellation can be fine tuned by adding more harmonic terms and by altering the weighting of the translated functions to achieve a higher degree of cancellation than that possible with the Hanning window. Two windows that offer such improvements on the Hanning windows are the Hamming and the Blackman windows.

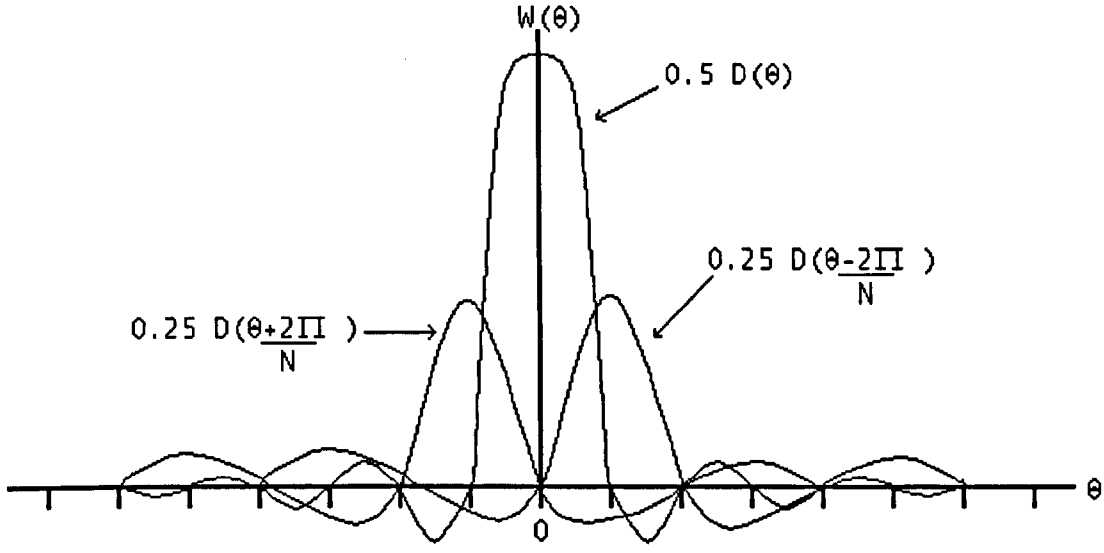

Figure 2.14 Transform of Hanning window as sum of three functions.

The Hamming window is constructed by altering the weighting coefficients of the Hanning window so as to achieve greater sidelobe cancellation. The general equations governing the windows and their transforms are:

$$w(n) = \alpha + (1-\alpha)\cos\left[\frac{2\pi}{N}n\right] \quad \text{.....(50)}$$

$$W(\theta) = \alpha D(\theta) + 0.5(1-\alpha)\left[D\left(\theta - \frac{2\pi}{N}\right) + D\left(\theta + \frac{2\pi}{N}\right)\right] \quad \text{.....(51)}$$

The Hamming window is constructed by letting α=0.54 and an improvement in sidelobe cancellation is achieved over the Hanning window.

As shown in the equation above the transforms of the Hanning and Hamming windows are the summation of three shifted sampling functions. More complicated windows may be calculated by using functions with more components derived from higher order harmonics. Examples of this are the three coefficient Blackman window and the four

coefficient Blackman-Harris or Kaiser-Bessel window. The general equation of the four term window is:

$$w(n) = a_0 - a_1 \cos\left(\frac{2\pi}{N}n\right) + a_2 \cos\left(\frac{2\pi}{N}2n\right) - a_3 \cos\left(\frac{2\pi}{N}3n\right) \ldots\ldots n = 0,1,2,\cdots,N-1 \ldots (52)$$

where the coefficients are chosen to achieve a minimum sidelobe level. The adverse consequence of this sidelobe reduction is the increased width of the centre lobe as the number of coefficients increases.

Window	Highest sidelobe (dB)	Sidelobe fall off (dB/oct)	Coherent gain	ENBW (bins)	3 dB BW (bins)	Scallop loss (dB)	Worst case process loss (dB)
Rectangular	-13	-6	1.00	1.00	0.89	3.92	3.92
Hanning	-32	-18	0.50	1.50	1.44	1.42	3.18
Hamming	-43	-6	0.54	1.36	1.30	1.78	3.10
Blackman	-58	-18	0.42	1.73	1.68	1.10	3.47
Blackman-Harris 3 term	-61	-6	0.45	1.61	1.56	1.27	3.34
Blackman-Harris 4 term	-92	-6	0.36	2.00	1.90	0.83	3.85

Table 2.3 Comparison of figures of merit for various windows

The values of the various figures of merit, as calculated by Harris [4], for different windows are shown in Table 2.3 for the purposes of comparison. The most important figures to our application are the sidelobe attenuation and the width of the central lobe indicated by the 3 dB bandwidth of the central lobe. The other figures relate to the computational efficiency of the overall window and do not affect its ability to resolve individual frequencies directly. It can be seen that the Hamming window appears to have superior characteristics to the Hanning window with a lower sidelobe level but narrower level central lobe. The Blackman window and the Blackman-Harris groups have a lower sidelobe level still but a wider main lobe.

Fast Fourier Transform analysis was carried out on input signals of varying quality with the different windows applied after sampling to see if there was any discernible improvement in the results and whether the results obtained in practice matched the figures given above.

2.4 References

[1] Gerd Keiser, *Optical Fibre Communications, 3rd Edition*, McGraw-Hill, New York, 2000.

[2] J. G. Proakis, D. G. Manolakis, *Digital Signal Processing, Principles, Algorithms, and Applications, 3rd Edition*, Prentice Hall International, 1996.

[3] J. W. Cooley, J. Tukey, "An Algorithm for Machine Calculation of Complex Fourier Series", *Mathematical Computation*, 19, April 1965, pp 297-301.

[4] F. J. Harris, "On the use of windows for harmonic analysis with the discrete Fourier transform", *Proceedings of the IEEE*, 66(1), pp 51-83, 1978.

Chapter 3

Rotation Monitoring

In Chapter 1 the historical development of and the market situation for systems that measure the rotational speed and torque characteristics of shafts was discussed. In this chapter the operation of the sensors and their integration into large-scale industrial systems is reviewed. Some commonly used systems for monitoring other characteristics associated with rotation such as vibration as well as some novel devices for torque measurement currently being developed are also described.

3.1 Devices for measuring speed of rotation

3.1.1 Tachometers

The most common form of rotation monitor that is found in the world today is the vehicle speedometer. Most commonly these are variable magnetic reluctance devices and function by means of electromagnetic induction. The reluctance of a magnetic circuit is affected by the rotation of a ferromagnetic disc that rotates at an angular velocity proportional to that of the wheel. This produces an electromotive force in an electrical coil that powers a galvanometer connected to the indicator needle. This principle is employed in tachometers used in many other applications. However, the accuracy of these sensors is highly frequency dependent with typical outputs being in the order of millivolts at low speeds but potentially rising to 100 V at speeds above 100 mph. This means that the electronic instrumentation required for detection is vulnerable to electromagnetic interference at low speeds.

Anti-lock braking systems, which seek to stop cars skidding by sensing when a wheel has locked up and then releasing and reapplying the brakes, are being fitted as standard to high performance cars. The natural immunity of optical systems from usual electromagnetic interference has prompted their use in devices being developed for detecting the angular speed of the wheels. One such device, a magneto-optical tachometer [1], uses a plastic optical fibre to transmit light from an LED to a photo-detector via a sensor head that causes the light to modulate as the magnetic inductance of a rotating ferromagnetic disc changes. The tachometer can measure wheel speed from 0 to 300 kph. The rotating ferromagnetic disc has 46 non-ferromagnetic cylinders inserted symmetrically near its outer edge to cause this change in inductance, with 46 being the standard number of pulses per wheel rotation in current ABS systems.

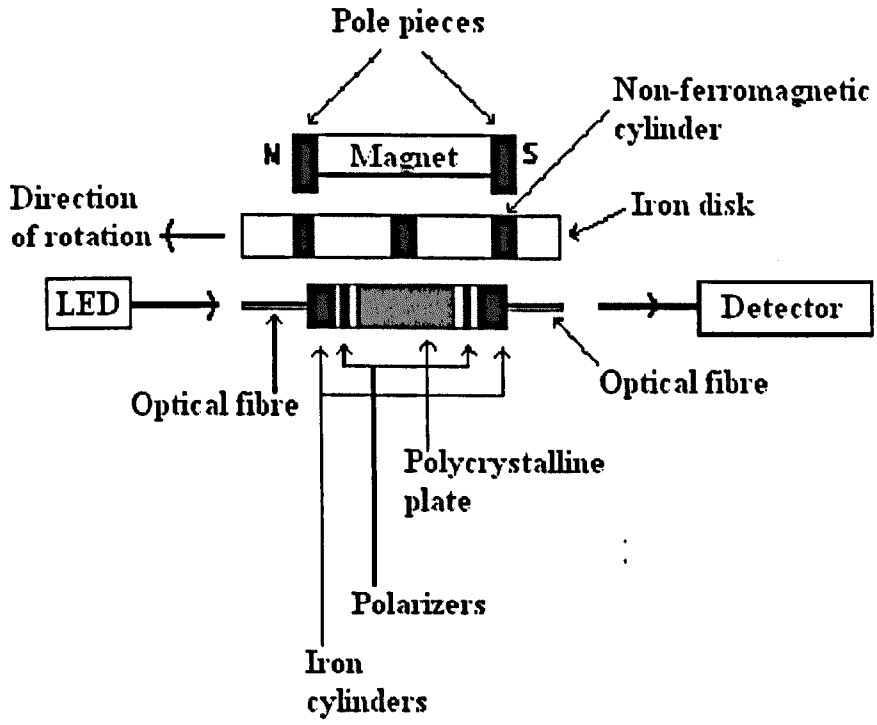

Figure 3.1 Magneto-optical tachometer sensor.

As can be seen from Figure 3.1 the sensor head consists of a polycrystalline plate mounted between two polarizers through which light from an LED source is directed to a photodiode detector. When the non-ferromagnetic discs are level with the pole pieces the magnetic field is coupled through the sensor head. The polycrystalline plate acts as a Faraday rotator so the plane of polarisation of the light beam is twisted when exposed to the magnetic field. When the pole pieces are opposite the ordinary iron disc the sensor is shielded from the field so no light passes through the sensor. This causes the light intensity to be modulated as the disc rotates.

3.1.2 Rotation sensors incorporating optical fibres

A number of systems incorporating optical fibres have been developed that monitor rotating shafts on smaller pieces of machinery that are commonly found in factories and other situations all over the world. Some systems have been developed that utilise optical fibres to illuminate the rotating shaft and then process the reflected light to determine the frequency of rotation. A commercially available unit designed for monitoring timing and phase reference data [2] during the testing of motors and transmission systems uses a high resolution infrared fibre optic sensor with a bandwidth of 50 kHz to measure shaft speed. The passing of machined marks modulates the optical signal and enables the correlation of the instantaneous dynamic motion of the shaft at various points along its length. This system is particularly useful for balancing the operation of shafts with unwanted vibrations.

A non-contact fibre-optic sensor for measuring the twist and speed of rotation of a shaft has been developed by NASA [3] as shown in Figure 3.2. The beam from a helium-neon laser is coupled into two multi-mode optical fibres using a bi-directional

coupler. Graded-index lenses on the ends of each fibre focus the light onto the shaft at two separate points along the axis of the shaft where reflective spots have been applied to the surface. As the spots on the shaft pass through the laser beam the graded-index lens captures pulses of light and bi-directional couplers at each lens allow the reflected light to be transmitted along a second optical fibre to a photodiode. The electronic signals from the photodiodes are digitised and stored for analysis by microprocessor. The speed of rotation is calculated from the period of the pulses of reflected light and the twist is calculated by multiplying the delay between the pulses from the two separate spots by the speed of rotation. The system was tested on a phenolic resin shaft 1.22 m long by 12.7 mm diameter rotating at 19.67 Hz and angles of twist between 0.005° and 10° were detected. The authors reported that increasing the sampling rate improved the resolution and decreasing the spot size of the focused beam increased the accuracy.

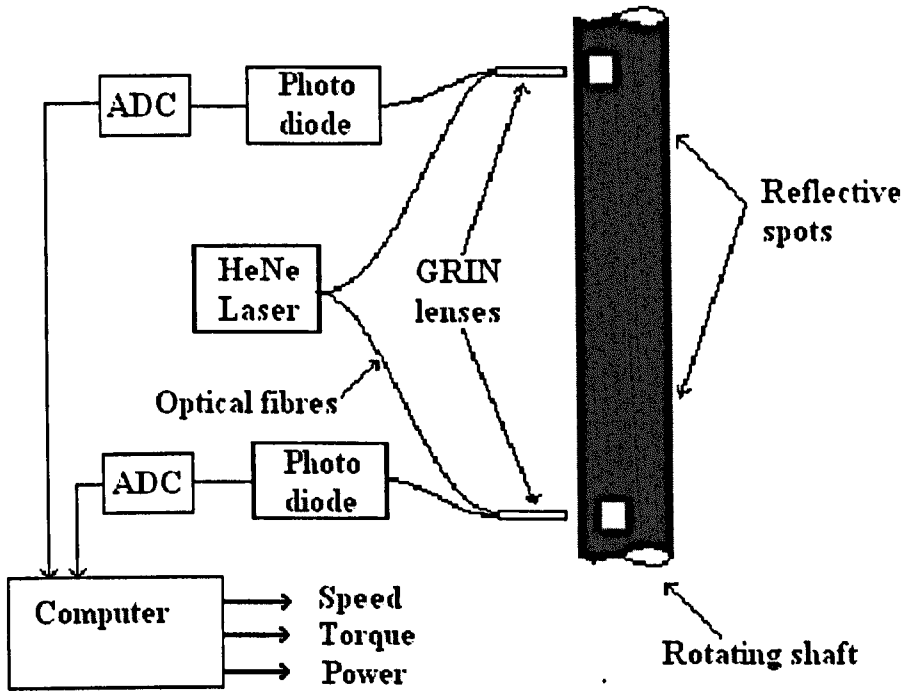

Figure 3.2 Overview of shaft rotation monitoring system.

The manner in which an optical-fibre is used to transmit a light signal onto the surface of a rotating shaft and return the reflections to a photodiode for electronic processing is similar to the basic procedure used in our own project. The components required here though, such as the HeNe laser and the GRIN lenses, are more costly, more fragile and less easy to deploy than those used in our set-up. However the main difference is that our system determines rotational velocity and torque through processing the reflection of the surface profile rather than detecting differences in the periods of rotation of the reflective spots. Any vibrational movement of the spots caused by vibrations acting on the shaft or machinery will cause uncertainty in the calculation of the speed of rotation. With the use of Fast Fourier transforms as in our system the vibrational signals, which are typically at very low frequencies, may be filtered out. One drawback with the Fast Fourier transform method is that at least two complete periods of rotation must be present in each set of samples meaning that the rate of refreshment of the results is slower.

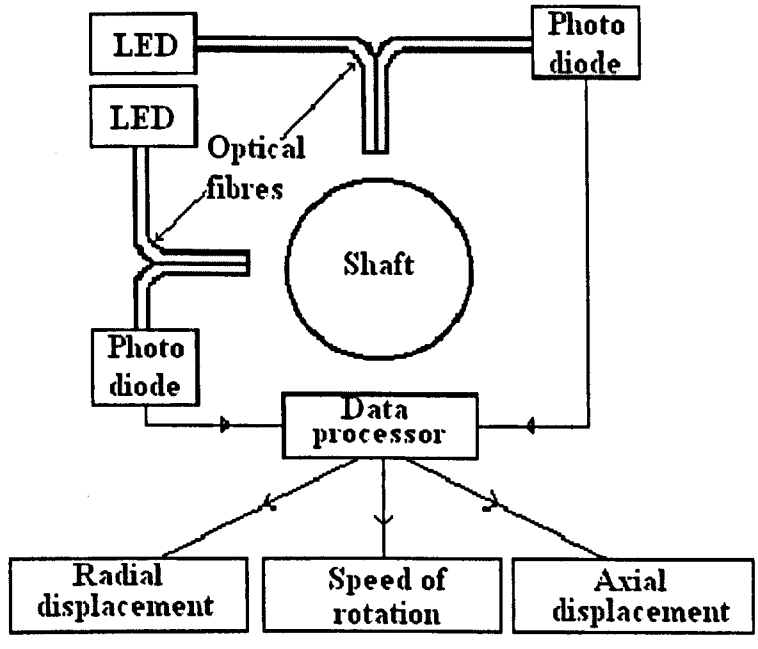

Figure 3.3. End on view of shaft motion analysing system.

Another shaft monitoring system to monitor the motions of a turbopump [4] that utilises optical fibres has been developed by NASA and is shown in Figures 3.3. It is capable of measuring axial and lateral vibrations as well as speeds of rotation up to 200,000 rpm. The system involves two optical sensors positioned so as to collect light reflected from eight reflective isosceles triangles attached to the shaft. The triangles are orientated with their bases aligned along a circumference of the shaft, as shown in Figure 3.4, so that they pass long ways underneath the pair of probe heads. The probe heads consist of two optical fibres pointing at the circumference of the shaft, one vertically from above, the other horizontally from the side. The frequency of passage of the triangles determines the speed of rotation of the shaft. Axial vibrations are detected from changes in the periods of passing of the individual triangles; radial vibrations are detected by changes in the ratio of the intensities of the signals collected at the two sensor locations.

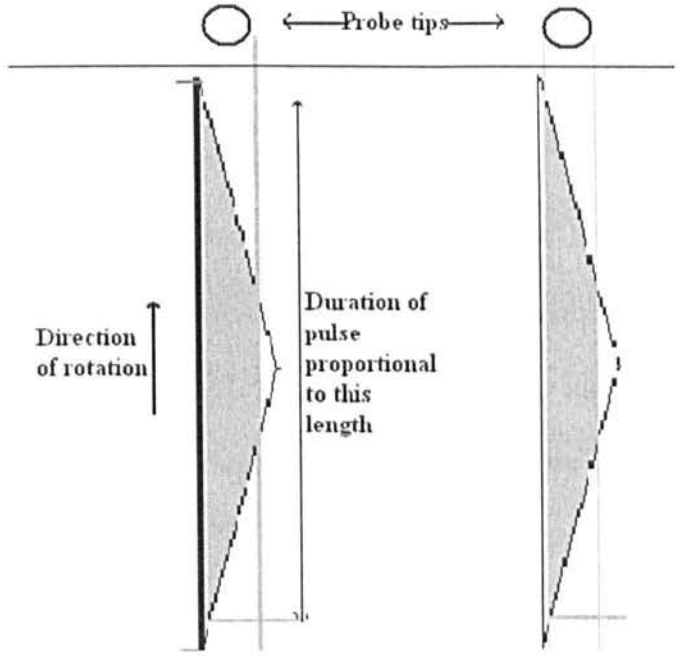

Figure 3.4. View of a section of the shaft surface showing patterns as seen by sensors

As with the previous system this system is similar to ours in that it uses optical-fibres to transmit a light signal to the shaft under investigation and return the reflected signal to opto-electronic circuitry for processing. The system appears to use simple components whilst having been designed to operate on a specific machine. The eight reflective triangles must be located extremely accurately meaning that retro-fitting the sensors to machines already in operation would be extremely time consuming and difficult in situations where accessibility is restricted. Also the reflectivity of the triangles would be greatly affected by dirt or oil contamination. The system as reported does not have a torque measurement capability although this could be achieved using another sensor located at a different axial position if the necessary processing algorithms were developed.

3.1.3 Laser Doppler velocimeters and vibrometers

With the advent of affordable and portable lasers a solution to the problem of gaining accurate information on vibrating surfaces located in hostile environments or in situations where the surface is rotating or extremely hot so that traditional sensors cannot be attached has been provided. This has been achieved through optical metrology relying on the principle of laser Doppler velocimetry (LDV) [5]. Portable instruments have been devised [6], [7], meaning the time intensive task of attaching transducers is unnecessary and higher frequencies may be monitored since contact resonance problems associated with transducer fixing are avoided. The Bruel & Kjaer device [7] is capable of measuring the velocity of rotation but requires the application of a specially textured reflected tape or paint to the surface being monitored. Other LDV set-ups mentioned may also be used to measure speed of rotation.

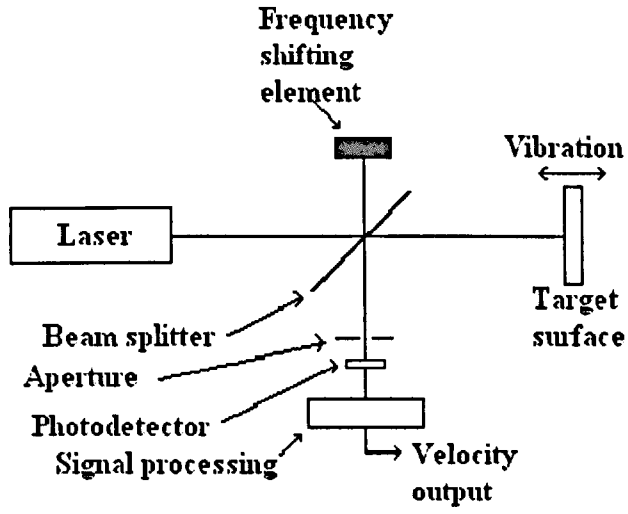

Figure 3.5. Laser vibrometer optical configuration.

The technique involves the measurement of the Doppler shift in the laser light back-scattered from the surface under investigation. On mixing this with a reference beam on a photodiode surface a time resolved vibrometer output proportional to the modulus of the target surface velocity is produced. In order to measure rotational velocity the surface irregularities that cause the back-scattered reflections must be rapidly replaced within the beam spot so that the speckle pattern on the photodiode moves. This causes Doppler frequency broadening to occur, which may be used to measure the velocity of the surface of the shaft. Figure 3.5 illustrates one possible configuration utilizing a Michelson interferometer configuration where the laser beam is split into two parts that illuminate the target and the reference surface. Unless the reference beam is frequency shifted only the amplitude is provided and the direction of the surface movement is left ambiguous. This ambiguity is overcome by frequency shifting the reference beam providing a carrier frequency that is then modulated by motion of the target surface. Methods for providing the frequency shift include the use of Bragg cells [8], rotating diffraction gratings or rotating scattering discs [7], or reflective piezoelectric elements [6]. A system using a laser diode with a self-mixing effect has been developed [9]. In

this a small proportion of the back-scattered light is returned into the laser diode where it mixes with the original wave and the Doppler shift is detected by a photodiode within the laser diode.

A fibre optic laser Doppler velocimeter for analysing three-dimensional fluid flows such as those found in the demanding environment posed by turbomachinery has been reported [10]. A robust probe consisting of three optical fibre channels oriented at different angles relative to the axis of the probe is capable of accessing the constricted space available. Two Doppler difference channels are used to measure the transverse velocity components and a reference beam channel is used to measure the on-axis velocity component.

Laser speckle pattern analysis may also be used for vibration monitoring since it has the advantage of providing a non-contact method and also may be used to cover a larger surface area. A system for vibration monitoring of engineering structures combining the techniques of laser Doppler velocimetry and laser speckle pattern interferometry has been developed [11]. The laser velocimeter and the laser speckle pattern interferometer utilize a shared reference arm and a shared piezoelectric phase modulator. Thus automatic heterodyning is achieved and the system is insensitive to out-of-axis motion.

Since all these sensors rely on interferometry the set-ups are technically difficult to implement and consequently expensive. If the system is to be portable a robust instrument must be produced, such as that of Bruel and Kjaer [7], but simpler technologies such as ours may be employed at a fraction of the price. It is usually

necessary to coat the surface being monitored, which might not always be accessible, with the proprietary reflective coating.

3.1.4 Torsional vibrometers

The measurement of torsional vibrations has long been of interest for monitoring the instantaneous motion of vibrating surfaces. Although torsional vibrometers provide no direct information concerning rotational velocity or torque their application to rotating shafts is of particular interest and much effort has been devoted to providing a reliable non-contact solution. Initially systems were developed that relied on monitoring the passing of slotted discs or toothed wheels connected to the rotating shaft and the signal obtained from these was demodulated to give data about the torsional vibrations occurring. These systems had low dynamic range and suffer from noise problems if the method of fixing of the transducers causes them to vibrate as a solid body with the rotating shaft. Non-contact methods were developed that used either bulk optic sensors or magnetic transducers but as with the velocimeter the advent of the laser provided an ideal coherent light source.

The laser torsional vibrometer, based on the Doppler effect, developed by Halliwell and Eastwood [12] provides an accurate method of overcoming these problems and measuring torsional vibrations on any visible part of a rotating specimen. The system is insensitive to translational vibrations of the rotating specimen or of the laser and transducer part of the instrument. Also the system can function with any cross-sectional geometry of shaft. A system based on this technique is commercially available from Bruel & Kjaer [13]. This purely optical set up uses a low power laser

for illumination and a Michelson interferometer is effected using a beam splitter and a mirror as shown in Figure 3.6.

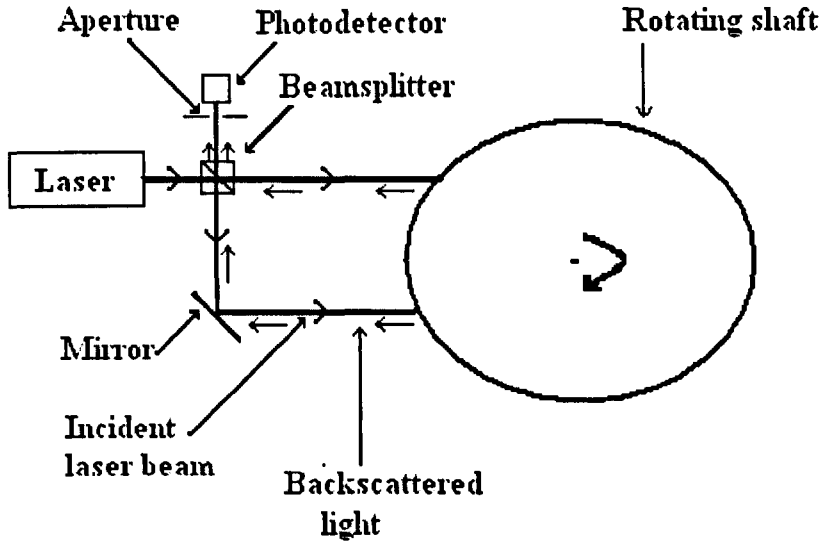

Figure 3.6. Laser Torsional Vibrometer: optical geometry.

Light is backscattered from two parallel laser beams and is collected by a photodiode. The backscattered light undergoes Doppler shifts and when the beams are combined on the surface of the photodiode heterodyning takes places and the signal from the detector is modulated at the frequency difference of the two beams. The two rotational velocity components cancel each other out leaving the torsional vibration value that is known as the beat frequency. Solid body vibrations of the shaft do not affect the output since equal shifts are generated from this form of vibration. This system has been tested [14] on heavy marine diesel engines that require a damping device to be fitted to the crankshaft in order to limit the growth of excessive vibration at torsional resonances. The correct running of the engine can be checked and thus used to diagnose impending failure in the dampers avoiding the need for downtime necessary with traditional maintenance procedures.

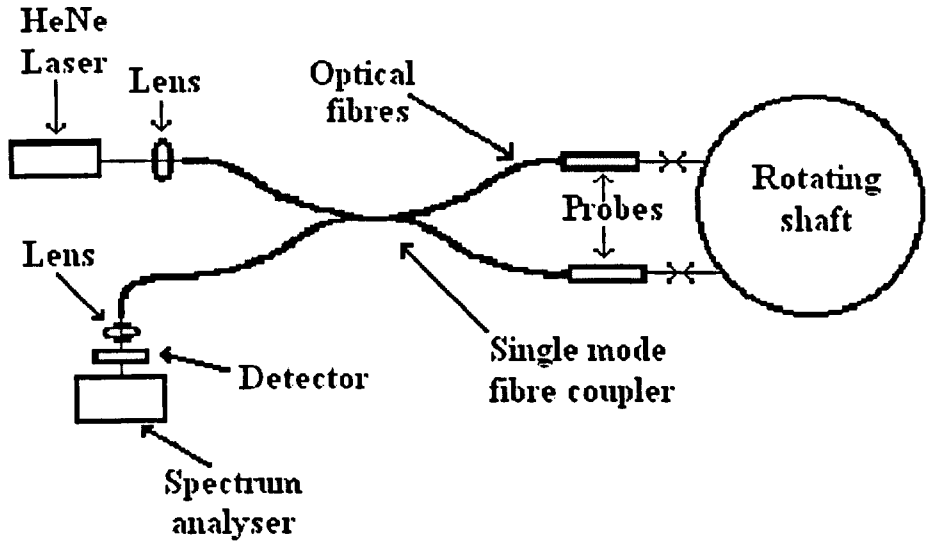

Figure 3.7 Set up of fibre optic torsional vibrometer in differential mode.

A fibre optic vibrometer has also been reported [15]. The implementation is shown in Figure 3.7 and uses a Michelson interferometer arrangement consisting of two single mode fibres with collimating heads on their ends directing beams derived from a 1.5 mW laser onto the shaft separated by 12.55 mm. The heads collect the back-scattered light and the signals from the two fibres are coupled into one fibre, the output from which is focused onto a photodiode. The output signal from the photodiode is amplified and analysed using a spectrum analyser. The fibre optic set-up has the obvious advantage over the bulk optic version is that it can be employed in inaccessible locations as well as not requiring direct line of sight.

As with the bulk optic instruments the backscattered light is Doppler shifted at a rate proportional to the angular frequency of the rotating object, the beam separation and the wavelength of the laser light. This method, as shown in Figure 3.7, is known as the differential mode of operation.

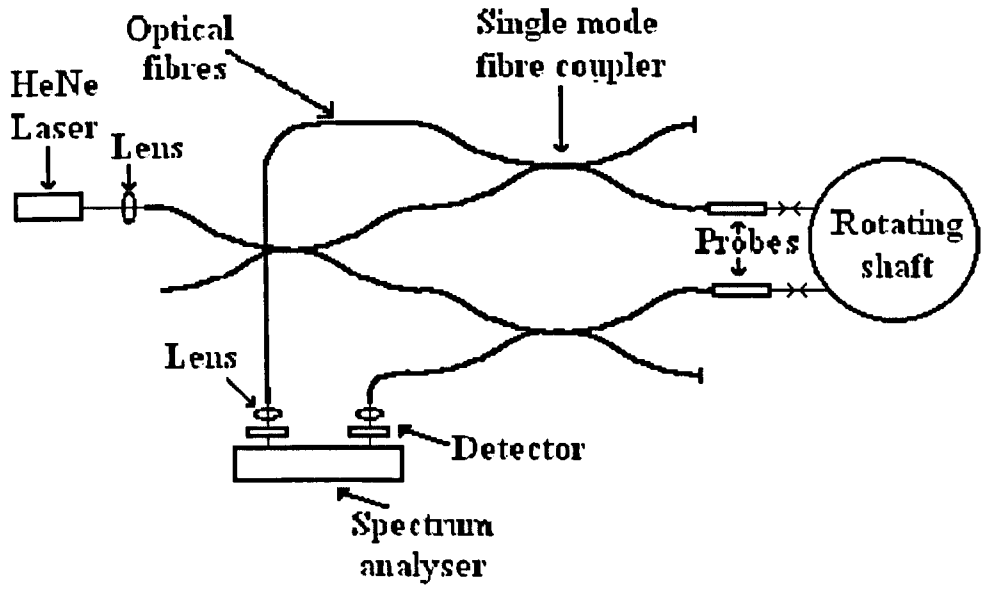

Figure 3.8 Fibre optic torsional sensor in reference mode.

A second mode of operation was also tested, known as reference mode, as shown in Figure 3.8, that has the advantage of needing significantly less optical power. In this set-up two reference beams were used to form separate interferometers and the torsional beat frequency is obtained by electronically combining the two separate frequency shifts.

Torsional vibrometers are not directly comparable with our sensor since they do not directly measure angular velocity or torque. The Bruel and Kjaer instrument is clearly impressive but it as also expensive. The sensors involving optical-fibres are difficult to set up, requiring careful alignment and coupling of the monomode fibres and the application of textured reflective tape to the surface of the shaft. The use of interferometry increases the cost of the sensor due to its complexity and susceptibility to vibration.

3.1.5 Commercially available optical systems

Despite the amount of research being performed into fibre optic rotation sensors it is hard to track down any of the speedometer or tachometer type that is commercially available. In their extensive survey on the general subject of fibre optic sensors [16] Dakin and Culshaw mention three such devices. Optech Inc. are listed as offering a tachometer using a remote chopper and reflector system, Aurora Optics Inc. offer a tachometer using a remote shaft encoder and Polytech Gmbh offer a laser Doppler velocimeter. However, none of these companies offers details of these in their current sales literature. Therefore it must be assumed that any fibre optic rotation sensors in commercial use are either in set ups designed in-house or possibly as a constituent part of a larger industrial system. One such example is a project at the Harbin Electric Machinery Company [17] in which fibre-optic sensors are used to monitor the oil pressure in the thrust bearings of a large generator shafts.

A major commercial use for fibre optic sensors is the application of fibre optic gyroscopes to motion sensing and navigation [18]. Honeywell manufactures fibre optic gyroscopes that are operating on the Boeing 777 and on Dornier commuter aircraft and Hitachi was producing 3000 fibre optic gyroscopes per month in support of automobile navigation systems. JAE has installed fibre optic gyroscopes on remotely piloted helicopters, on lawn mowers for sports fields and on robots for cleaning floors in shopping centres.

Some optically based rotation monitoring systems are commercially available but these do not employ optical fibres. An optical pickup sensor that consists of an LED and a phototransistor mounted in a stainless steel case on a flexible cable is used for

diagnosing vibration and balance problems [2]. The detector must be fixed over a marker such as a notch, keyway, hole or reflective spot on the rotating shaft and this generates a voltage pulse that is used as the reference signal for speed and frequency measurements. If used in conjunction with sensors at other points along the shaft the instantaneous dynamic motion may be calculated from these measurements. This data may be used to analyse the running of the system and any necessary remedial adjustments to the balance may be performed and the system checked again.

As described in the previous section Bruel and Kjaer successfully market their laser velocimeter [7] for monitoring vibrating surfaces and their torsional vibrometer [13] for monitoring torsional vibrations in rotating shafts. Dantek have also marketed a torsional vibrometer [19]. These are purely free space optical devices but, as Liu, Berwick and Jackson have demonstrated [15] the possibility exists for them to be adapted to operate with optical fibres.

3.1.6 Fibre optic systems monitoring industrial rotating machinery

Fibre optic sensors offer advantages over conventional sensors in locations where electromagnetic interference is a significant problem. Such locations include power stations and areas close to heavy-duty machinery and examples of fibre optic sensors being introduced for use in such locations have been reported. An optical accelerometer has been developed and tested [20] in order to monitor and measure vibrations to a high degree of accuracy in hydroelectric power plants. As shown in Figure 2.9, this is set up in an interferometric configuration and the compactness and the inherent immunity from electromagnetic interference of the system make it ideal for this application.

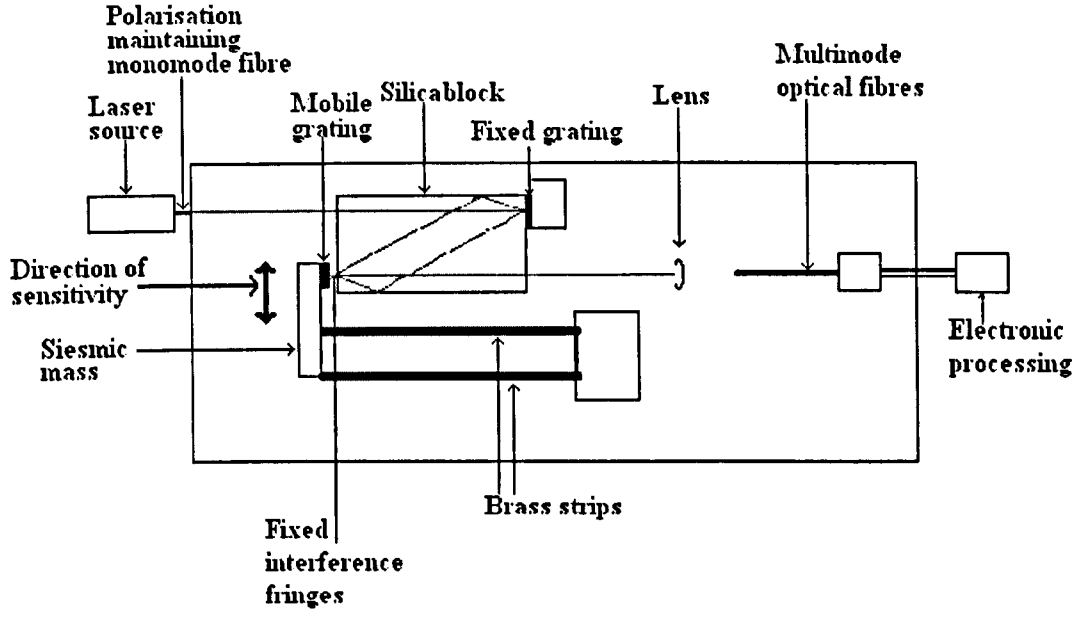

Figure 3.9 An optical accelerometer.

The sensor consists of an opto-mechanical transducer head, optical fibres and an electronic processor. The seismic mass is supported by two parallel strips of brass and for optimum sensitivity the resonant frequency must be in the region of the upper level of the frequency of vibration. In the optical system the beam from a He-Ne is launched into a silica block via a polarisation preserving monomode fibre and a graded index lens. The beam is split into two equal parts by a diffraction grating and these beams recombine after internal reflection in the block on another grating that is attached to the seismic mass. The fringe pattern created by the superposition of the two beams moves with the vibration of the block and produces a beam that is reflected through the block. The two multimode fibres collect the beam and variations in the relative strength between the two transmitted signals may be processed to extract the frequency of vibration of the system. This information may be compared to known existing data to check that the machinery is running consistently.

The development of another fibre-optic sensor for use in an electric power station as a monitor on a hydro-generator has also been described [21] from the initial fabrication of the sensor right through to its in situ testing. This simple device uses an optical fibre as a cantilever and has no seismic mass. The transducer requires only simple electronic processing for detecting the intensity modulation and then applies compensation techniques, which provide good stability and accuracy.

3.2 Torque Sensors

As far as industrial torque sensors are concerned "non-contact" is taken as meaning that there is no physical connection between the rotating shaft and the stationary outside world. The most common forms of non-contact systems available involve inserting a shaft of known flexibility with strain sensors already attached into the drive assembly [22]. It is possible that a strain sensitive transducer may be bonded to the surface of the shaft or that the shaft surface be covered with a strain sensitive coating but systems such as these are liable to contamination or corrosion in industrial situations.

The transducers used may be highly sensitive and accurate but difficulty occurs in passing the output signal to the outside world. Commonly a slip ring is attached to the shaft and the signal transmitted to the control unit via brush contacts [23]. This process is susceptible to electromagnetic interference with regular maintenance being required. Friction losses, which also cause heating and the inherent mass of the rings may limit the maximum speed of the system. At present there exist two main alternatives to overcome the problems inherent with slip rings. One solution involves rotary transformers linked by inductive transmission [23]. The signal from the strain gauge is

encoded into an ac voltage signal that excites the primary coil wrapped around the shaft. The secondary coil is fixed in position around the rotating shaft and receives the signal which may then be decoded. Similar systems using radio telemetry have also been developed whereby the encoded data from the strain gauges is transmitted to the control box by a VHF radio signal [2]. These systems are complicated and the need for electronic filtering during the decoding of the signals limits the bandwidth of the system.

As mentioned in the previous chapter another approach is to measure the torsional deflection over a given length of shaft through monitoring changes in the relative phase of signals collected at either end of the shaft. This method, the basis of the system developed in this project, avoids the problems of contamination and corrosion through the benefit of remoteness and the lack of any direct contact with the shaft whatsoever. Several other non-contact optical techniques have been developed profiting through having immunity from electrical noise, low mass and high bandwidth. These systems, being totally non-contact, are capable of being retrofitted whereas with the strain gauge type systems often it is impracticable to insert or apply the sensors into an existing system due to lack of space or the inaccessibility of the rotating parts. This means that the utilisation of optical and fibre optic systems can open up new areas of possible use in challenging environments.

3.2.1 Sensorless control of induction motors

Whilst the aim of this project has been to develop a sensor for the measurement of torque there is much research activity aimed at developing "sensorless" control of induction motors [24]. This involves using high speed microprocessor based sensing

and control of the stator and rotor currents in conjunction with a highly accurate model of the motor behaviour.

The DC motor was the original workhorse in many industrial applications such as the powering of mixers, pumps and production line drives where variable speed and torque control is required. The control is achieved through varying the armature and field currents. However the use of brushes with the commutator means that periodic maintenance is required and DC motors being unsuitable for use in explosive or corrosive environments. Also their operating speed is limited and encoders are needed to provide positional feedback. DC motors have now largely been replaced following the development of controllable AC induction motors that can emulate the operation of DC motors but offer greater economy and robustness. The most common AC drives use pulse width modulation where the constant AC supply input is rectified, filtered and then reconverted into a signal of variable voltage and frequency. Using microprocessor management in conjunction with sensors giving feedback on angular speed and position accurate control of the motor speed and torque may be achieved. Systems are commercially available [25] but have to be specified in advance to meet the desired purpose and there is little chance for retrofitting. Further developments of the technology have been reported [26].

Now more advanced "sensorless" control systems are being developed to control speed and torque of the shaft [24] that use models of the motor performance through accurate knowledge of stator resistance, mutual inductance, and motor inertia and take into account factors like temperature compensation. This is achieved without any external shaft mounted transducers and is known as direct torque control [27].

3.2.2 Strain Gauges

Strain gauges are devices whose electrical resistance varies in proportion to the amount of strain exerted on the device. The most common type of strain gauge is the bonded metallic strain gauge that consists of a very fine wire or metallic foil arranged in a grid pattern as shown in Figure 3.10. Piezoresistive semiconductor materials are also used. The cross sectional areas of the metallic grids are kept as small as possible to minimise the effects of shear strain and Poisson strain. The grid is bonded to a thin carrier backing that is either bonded directly to the shaft being monitored or to a shaft of known shear modulus that is then inserted into the drive system

Since strain measurements normally involve very small measurements, typically a few millistrains, very sensitive and accurate measurement techniques are required. To assist in avoiding the effects of temperature drift a modified version of the Wheatstone bridge is used with a current or voltage excitation source. To achieve the greatest sensitivity the gauges are mounted on the shaft in pairs orientated at right angles to one another and at 45° to the axis of the shaft. Thus one gauge experiences the maximum tensile strain, the other the maximum compressive strain.

The fact that the transducers need bonding to the surface of the shaft means they are awkward to retrofit to existing machinery if the shaft to be monitored is contaminated in any way or in an a confined locations. They are not capable of measuring rotational velocity so a separate sensor is required to monitor this. In environments subject to electromagnetic interference a low signal to noise ratio can limit the sensitivity of the sensors and the switching of heavy loads can cause electrical spikes resulting in instability of the output of the system. Also the need to transmit the output signal away

from the sensor using slip rings or a non-contact transmission method adds greatly to the cost of the system.

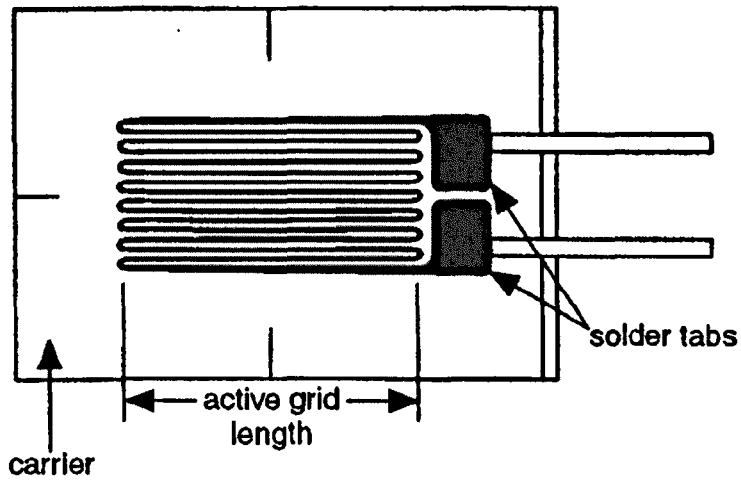

Figure 3.10. A bonded metallic strain gauge.

3.2.3 Optical torque sensors

An optical torque sensor for monitoring rotating shafts developed by Sensor Technology is commercially available [28]. This functions by measuring the light transmitted through a pair of gratings attached to the surface of the shaft as shown in Figure 3.11. The sensor consists of two overlapping discs with the segments that form the grating positioned on the shaft so that at zero torque the opaque segments in one disc are half obscured by the dark segments in the other disc. Light from a stationary source passes through the segments as the shaft rotates and is detected by a photocell. As the torque applied to the shaft is varied the amount of overlap varies thus altering the current produced by the photocell. This set-up has benefit of providing bi-directional detection and avoids non-linearity in the photocell output at low levels of illumination. These devices require fixing in line with the shaft being monitored

meaning that they are unsuitable for retrofitting since the system would have to be modified to accommodate it. Also if used in industrial locations dirt or oil could contaminate the opaque segments causing errors in the results.

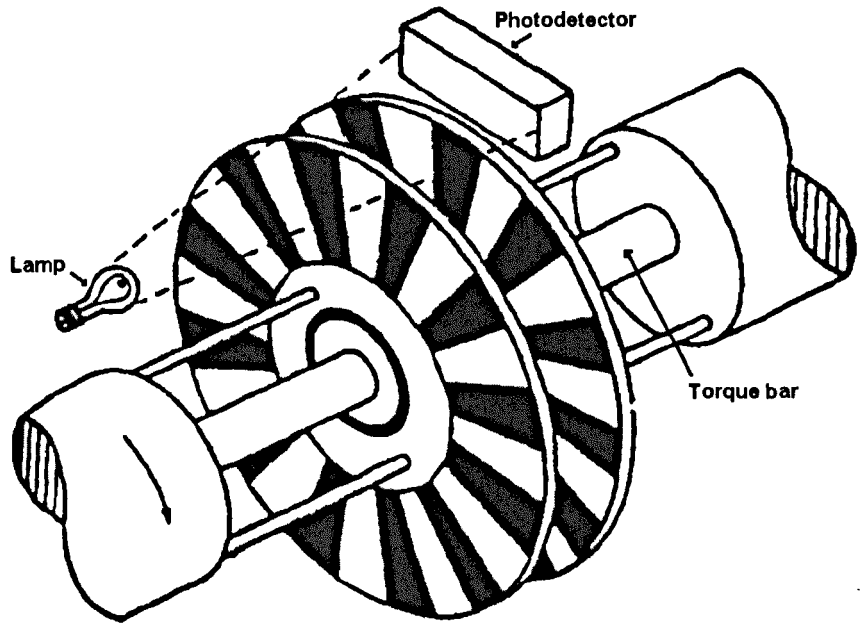

Figure 3.11. An optical grating torquemeter.

In his article on torque measurement [29], published in 1989, Graham Reed describes a number of systems, some of which have reached the market place. A system involving optical fibres and a bi-directional coupler was described; the change in phase in signal modulations produced by reflective segments at one end of the shaft and a pair of polarisers, one fixed, one rotating, at the other end were monitored. Reed mentions a number of systems developed prior to the increasing popularity and commercial viability of lasers and fibre-optics in the late 1980s. For instance Simmonds Precision marketed a system measuring the change in phase difference between light signals reflected from a series of reflective strips fixed on either end of the shaft and a similar

system developed by Peirson in 1980, which monitored just one spot on either end of the shaft.

Reed noted that as early as 1962 Kresek and Tiefermann reported a system developed by NASA [30] used for research into rocket pump and turbine design, capable of monitoring operating speeds of rotation up to 50,000 rpm. It involved a complicated optical set up illuminating two reflective surfaces at either end of the shaft. As the shaft rotated a reflected spot was deflected with increasing torque. He also mentioned a Diffractographic Torque Sensor reported in 1972 by Prior et al [31]. Two halves of a slit were attached to opposite ends of a torsion bar and illuminated by monochromatic light. As the bar twisted the two parts of the slit move with respect to each other thereby varying the resultant diffraction pattern with applied torque.

The system reported by Madzer that was also developed by NASA [3], which has been mentioned previously as a method for measuring rotational velocity, is also capable of measuring torque. It achieves this by measuring changes in the time delay between the sensing of reflective marks fixed at either end of the shaft. Optical fibres are used to transmit the light signal. In another system a miniaturised sensor operating on a similar principle has been developed [32]. The sensor unit is compact having dimensions of only 50 x 15 x 2 mm and consists of photodetectors, laser diode source, a glass integrated optical chip and ball lenses for collimating and beam focusing. The beam from the laser diode is directed onto the machined marks on the shaft surface by the integrated optical chip and torque is detected by changes in the phase shift of the output signal.

3.2.4 Surface acoustic wave sensors

Surface acoustic waves, also known as Rayleigh waves after their discoverer, travel over the plane boundary between an elastic half-space and a vacuum, or a sufficiently rarefied medium such as air. Surface acoustic waves are mechanical, i.e. acoustic, rather than electromagnetic in nature and their amplitude decays rapidly with depth into the solid. A proven system is commercially available [33].

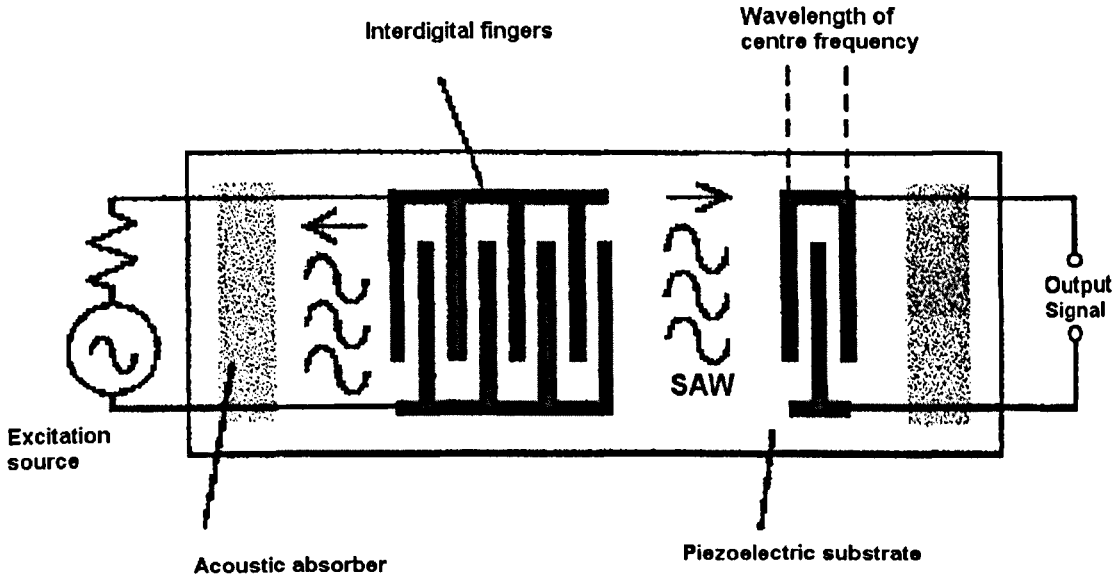

Figure 3.12 Surface acoustic wave torque sensing transducer (Taken from [33])

The SAW transducer consists of two arrays of thin metal electrodes deposited on a piezoelectric substrate such as quartz. The electrodes are positioned, as illustrated in Figure 3.12, like interlocking fingers at a spacing of ½ or ¼ of the wavelength of the central operating frequency of the excitation signal that is applied across the electrodes. The complete transducer set-up must then be bonded onto the surface of the shaft, which is often unmanageable in locations where space is restricted or the

shaft is contaminated. As is shown in Figure 3.13 two transducers are bonded to the shaft at an orientation of 45° to the axis of the shaft and 90° to each other. The transducers operate similarly to traditional strain gauges with each detector forming part of an oscillator circuit whose natural resonance frequency depends on the dimensions of the transducer, temperature and also the strain present in the shaft. As the shaft is twisted one element becomes longer, so that its natural frequency decreases, while the other becomes shorter, so that its natural frequency increases. The difference between the natural frequencies determines the amount of strain. The excitation and output signals of the transducers are transmitted by non-contact RF couplers to and from an electronic control box that is interfaced to a PC. Telemetry adds significantly to the system cost and is prone to noise from electromagnetic interference in the excitation and output signals. The transducer cannot monitor the rotational velocity so a separate sensor would be required for this function.

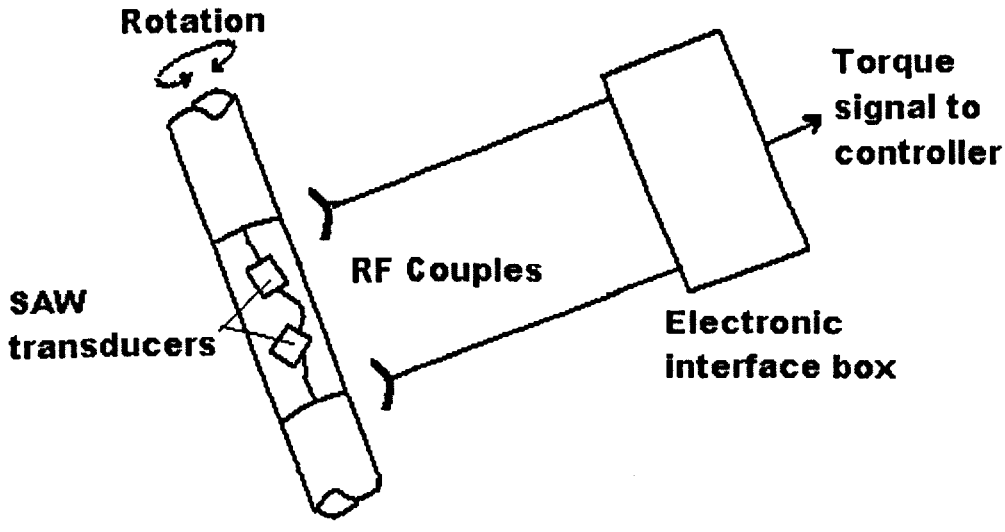

Figure 3.13 Arrangement of SAW transducers and controller

A similar technique using piezoelectric thick films as both the source and detector of elastic waves has also been reported [34]. The principle of operation of the sensor involves measuring changes in the velocity of wave propagation caused by changing torque applied to the shaft.

3.2.5 Torsional variable differential transformer

Torsional variable differential transformers are a type of non-contact torque sensor that are connected in line with the shaft of the system being monitored. The torsional strain is measured by sensing changes in a magnetic field that is induced by a transformer on the surface of the rotating shaft [23]. The shaft has to be made of a non-magnetic material and, as shown in Figure 3.14, is jacketed with three pieces of magnetic material that are separated by narrow gaps orientated at 45° to the axis of the shaft.

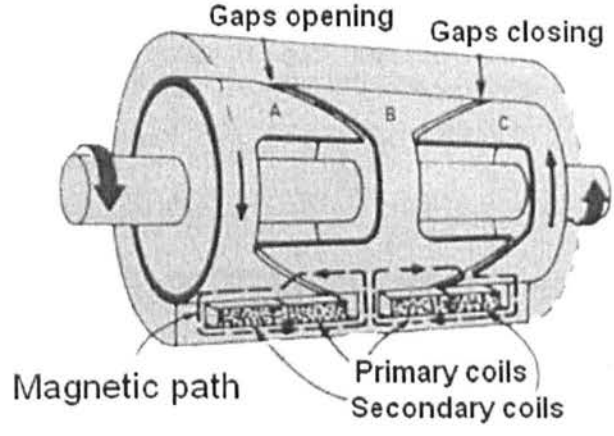

Figure 3.14. Torsional variable differential transformer (Taken from [23])

When torque is applied to the shaft one of the gaps opens and the other closes which causes the magnetic reluctance in the gaps to increase and decrease correspondingly. The changes in reluctance affect the voltage induced in the secondary coil of the transformer and by monitoring the ratio of the primary to secondary voltage signals the magnitude and direction of the applied torque may be deduced.

3.2.6 Magneto-elastic torque sensors

A non-contact torque sensor has been developed that senses changes in the magnetic flux density of a magnetoelastic foil fixed to the surface of a shaft [35]. These changes are detected by external sensor heads that are positioned in close proximity to the shaft at an orientated 45° to the axis of rotation and at 90° to each other. The sensors, as shown in Figure 3.15, consist of a NiFe yoke whose pole pieces contain excitation coils and CMOS MAGFET detectors. The torque is determined by taking differential measurements of the magnetic flux density measured by two sensors. This system requires a suitable section of shaft to be accessible and would be unsuitable for use in areas where there is electromagnetic interference or magnetic fields such as in the vicinity of power generating machinery.

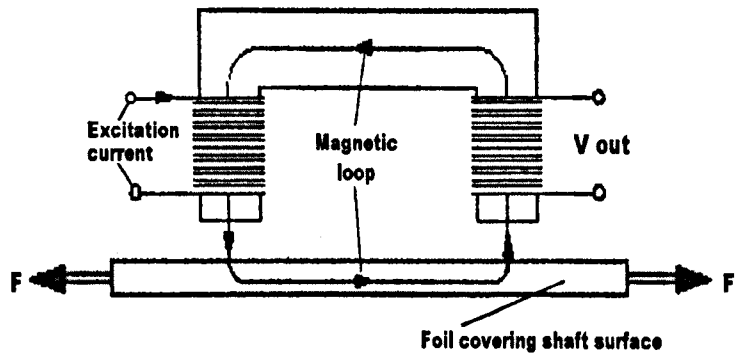

Figure 3.15. Magnetoelastic torque sensor.

A similar system has been developed that does not require any form of shaft coating but uses a proprietary ferromagnetic shaft in conjunction with a magnetic discriminator containing electronic sensors capable of measuring changes in the magnetic permeability of the shaft [36]. The ferromagnetic shaft has magnetic domains whose orientation is altered by the stress caused by applied torque. The shaft has two knurled bands at 45° to the axis of the shaft and 90° to each other around its circumference, one of which is compressed, the other of which is stretched as the torque is applied resulting in a fluctuation of the permeability in each region. These variations in permeability produce changes in the output of the two sensor voltage signals, the difference in which is directly proportional to the applied torque.

3.2.7 Photoelastic torque sensors

Photoelasticity is commonly used as an accurate and reliable method for analysing the stresses and strains present in mechanical components or structures. This technique has been adapted for measuring the torque applied to static or rotating shafts [35]. A photoelastic cylinder is attached to the surface of the shaft under investigation and illuminated by polarised light. As the torque varies the shaft coating exhibits the resultant strain as a two-dimensional fringe pattern when viewed through a polarizer. The strain pattern is a complicated function of the applied torque and a CCD camera is used to acquire the patterns for image processing. A neural network compares the fringe patterns obtained by the image processor with patterns obtained from previously performed calibration tests to make an estimate of the applied torque. This process only produces accurate results on static or slowly rotating shafts and requires an immense amount of processing power to function.

3.2.8 Mechanical Resonator

Tuning fork type resonators may be used as torque transducers since their resonance frequency varies when they are subjected to tensile stress. One such sensor has been developed [38] utilising two metallic tuning forks spot welded at right angles to each other onto a torsion bar that is connected in line with the shaft under observation. Each of the tuning forks consists of three beams with one of the beams being excited by a piezoelectric ceramic chip and the resonance then detected by another chip attached to a second beam. The system would be difficult to calibrate accurately and contamination or vibration could affect the resonance of the forks. The transmission of the excitation signal and output signal from the detector chip and from the shaft is achieved via capacitively coupled plates which is highly susceptible to electromagnetic interference. Hence electronic circuitry containing a voltage-controlled oscillator governed by a phase locked loop is required to control the system and extract the output signal.

3.2.9 Reaction sensors

Reaction torque sensors measure the turning force that is exerted by the motion of the rotating parts on the fixed housing of the motor [23]. This is the reaction force required to stop the housing from rotating when the drive shaft is driven by a power source. One method of measuring this force involves mounting the motor housing on a flange using a deformable sensor. The deformable sensor will twist by a small amount and strain gauges attached to it produce an electrical response proportional to the torque. With this type of sensor care must be taken to account for the inertia of the motor and connections such as power lines which might affect the torque experienced by the flange. If the connections are changed then the system must be recalibrated.

In another common type of reaction torque sensor a dynamometer is mounted on trunnion bearings so that it is free to rotate. A load cell is attached to an arm extending from the side of the dynamometer housing and the reaction torque required to stop the housing from turning is measured. Problems with this sort of sensor include uncertainty over the calibration of the bearing resistance especially at low torque and possible errors in the torque reading caused by electrical and other connections. The frequency response of the system is poor due to its high inertia meaning that this method is not capable of providing accurate readings under conditions of acceleration or deceleration.

Torque tables are a similar type of device consisting of a mounting bed upon which the device under investigation is fixed supported by torque sensitive flexures at each corner. Strain gauges are attached to the flexures forming a strain gauge bridge consisting of four arms. If the device is positioned with the input or output shaft located above the centre of rotation of the table a reaction torque is produced that may be accurately measured by the sensors.

3.2.10 Dynamometers

Dynamometers are devices for measuring the power transmitted from a rotating shaft into or out of machinery, normally used in the design or calibration process. Many products are commercially available [39], [40]. A dynamometer functions through absorbing power supplied to the system under investigation through the application of frictional retardation and measuring the resultant torque. Due to the necessity to measure torque a dynamometer system will always include a torque sensor of some description.

Examples of commonly used methods of retardation include eddy current brakes, direct application of dry friction and the fluid brakes. The eddy current brake is controlled by changing the dc input voltage; it cannot produce any resistance torque at zero speed and only light torque at low speed. The power dissipated usually in the form of heat is removed by cooling oil passed through the gap between the rotor and the stator. The eddy current brake is able to handle higher power and rotational speed than other types of dynamometers.

There are various types of simple mechanical friction brake, such as the Prony brake, where the torque is controlled my manual adjustment of the tension in a leather belt. Torque may be applied at zero speed by this method but it can be unsteady and inaccurate. It is, however, a popular method due to its low cost and simplicity. Fluid brakes use the friction generated when water or air swirls around paddle vanes to dissipate power and create torque. As with the eddy current brake this method is unable to produce torque at zero speed and only light torque at low speed but is capable of handling high rotational speeds and high power ratings.

The most versatile and accurate form of dynamometer is the dc electrical type that can measure either the power delivered out from a motor system or the power supplied into a mechanical system since it is able to function as either a generator or a motor. When functioning as a generator the power produced by the system under investigation may be measured and dissipated in resistance grids or recycled to power something else. Through knowing the power output at various shaft speeds and levels of torque, normally measured by a torque table, the optimum operating conditions for the system may be determined. When used as a motor to drive a system the torque to speed

characteristics of the system may be tested at different speeds under accelerating or decelerating load conditions.

3.3 Continuous monitoring of machine performance and tool wear

As mentioned previously one reason for employing rotation sensors is so that machinery may be allowed to operate continuously whilst the efficiency of its working and safety factors are accurately monitored. The information received may be used to check for the imminence of breakdown that might require attention meaning that the regular shutdown of machinery for maintenance need not occur. An example of this includes the integrated sensor system described earlier operating at the Harbin Electric Machinery Company [17], which employs fibre optic sensors. Further examples of development in this direction include the systems for continuous machine condition monitoring marketed by Future Fibre Technology [41] and a computer controlled system for monitoring the operation of generators in a power station [42].

A related area in which progress has been made is that of continuous monitoring for the detection of tool wear. Tool wear is an undesirable but unavoidable by-product of machining operations that causes degradation in the accuracy of the dimensions of the finished articles and in the quality of the surface finish. As the tool wear increases both the turning torque and the thrust required rise causing increased fatigue to the machine and greater likelihood of tool failure. Therefore monitoring the applied torque is useful in predicting these effects. Two similar non-contact sensor set-ups have been reported that measure this directly by fitting strain gauge bridges to a spacer in between the tool and its holder. One of the devices developed measures drilling torque and thrust [43] and uses an optical system to transfer the data from the rotating parts to a stationary

control unit. The other system reported [44] measures the torque generated by the tools of milling machines and uses telemetry to transfer data continuously from the rotating spindle to a stationary receiver.

Another technique reported is based on monitoring changes in spindle speed for the prediction of tool wear during turning operations [45]. An optical encoder for measuring shaft speed is fixed on the spindle and interfaced to a PC for signal processing and calculation of results. Compensations for lathe transmission ratio, the electrical configuration of the motor and the torque to speed relationship of the lathe are made. A number of tests were made with different combinations of cutting speed, feed rate, depth of cut and material hardness and the actual wear measurements match the predictions made by the system well.

Other systems have been developed for monitoring tool wear using optical fibres. A relationship has been established between the energy of the acoustic emissions produced during milling operations and the tool wear [46]. The acoustic emission energy is measured in terms of the rms value and it varies depending on the materials being worked on and the shape of the tool caused by the wear during operation. The sensor consists of a non-contact fibre optic interferometer that detects the acoustic emissions from the tool and workpiece. The sensor has the advantage of taking absolute calibrated readings unlike traditional piezoelectric acoustic emission transducers that are liable to variable frequency response and fluctuations in the transmission path.

Another non-contact system monitors the tool wear in lathe machining operations using a fibre-optic sensor in conjunction with a multilayered neural network [47]. As the tool wear increases the dimensions of the finished workpiece will also increase leading to a taper forming. This process happens over a long period of time and can be checked against the tolerance limits. The sensor consists of two bifurcated bundles of fibres, illumination is provided along one bundle by a laser source and a photodiode measures the intensity of the signal reflected back along the other bundle. The fibre-optic probe moves along with the tool monitoring the separation between the probe head and the part of the workpiece just finished. The signal is digitised and together with other cutting parameters is fed into the neural network. Good correlation has been obtained between the results predicted by the neural network and the dimensions measured under a microscope.

3.4 References

[1] H. Guerrero, J. L. Escudero, E. Bernabeu, "Magneto-optical tachometer using plastic optical fibre," *Measurement Science and Technology*, 4, 133-135, 1993.

[2] Product data: Bently Nevada Corporation, "Transducer Systems," Minden, NV, March 1992.

[3] G. C. Madzer, "A fibre optic sensor for non-contact measurement of shaft speed, torque and power," LEW-15099, National Technical Information Center, Springfield, VA, 1992.

[4] R. L. Randall, J. J. Collins, P. T. Coleman, E. J. Rosschak, "Shaft motion analysing system," LEW-15065, Lewis Research Center, 1992.

[5] F. Durst, A. Melling, J. H. Whitelaw, "Princples and practice of laser Doppler anemometry," Acedemic Press, 1981.

[6] J. R. Baker, R. I. Laming, T. H. Wilmshurst, N. A. Haliwell, "A new, high sensitivity laser vibrometer," *Optics and Laser Technology,* 22 (2), 241-244, (1990).

[7] Application note: Bruel & Kjaer, "The Laser Velocity Transducer, Its Principles and Applications," DK-2850, Naerum, Denmark, 1995.

[8] M. A. Nokes, B. C. Hill, A. E. Barelli, "Fibre optic heterodyne interferometer for vibration measurement in biological systems," *Review of Scientific Instruments*, 49, 722-728, (1978).

[9] S. Shinohara, A. Mochizuki, H. Yoshida, Masao Sumi, "Laser Doppler velocimeter using the self-mixing effect of a semiconductor laser diode," *Applied Optics*, 25 (9), 1417-1419, (1986).

[10] S. James, R. P. Tatam, R. L. Elder, "Design considerations for a three dimensional fiber optic laser Doppler velocimeter for turbomachinery applications," *Review of Scientific Instruments*, 68 (8), 3241-3246, (1997).

[11] J. D. Valera, A. F. Doval, J. D. C. Jones, "Combined fibre optic laser velocimeter and electronic speckle pattern interferometer with a common reference beam," *Measurement Science and Technology*, 4, 578-582, (1993).

[12] N. A. Halliwell, C. J. Pickering, P. G. Eastwood, "The laser torsional vibrometer: a new instrument," *Journal of Sound and Vibration*, 93 (4), 588-592, (1984).

[13] Product data: Bruel & Kjaer, "Torsional Vibration Meter: type 2523, BP 0958," DK-2850, Naerum, Denmark, 1995.

[14] N. A. Halliwell, P. G. Eastwood, "Marine vehicles and offshore installations: laser diagnostics of machinery health," *Optics and Lasers in Engineering*, 16 (), 337-350, (1992).

[15] T. Y. Liu, M. Berwick, D. A. Jackson, "Novel Fiber-optic torsional vibrometers," *Review of Scientific Instruments*, 63 (4), 2164-2169, (1992).

[16] J. Dakin, B. Culshaw, "Optical Fiber Sensors Volume Four: Applications, Analysis, and Future Trends," Artech House Publishers, London, 1997.

[17] M. Hobel, K. Haffner, "An on-line monitoring system for oil-film, pressure and temperature distributions in large-scale hydro-generator bearings," *Measurement Science & Technology*, 10 (5), 393-402, May 1999.

[18] A. Tebo, "High quality fiber optic gyros no longer just a dream," *SPIE Web*, www.spie.org/web/oer/february/feb97/tebo.html, february 1997.

[19] Dantek Technical News, "Laser Rotation Meter," April 1988, Dantek Electronic, Tonsbakken, 16-18, DK-2740, Skovlunde, Denmark.

[20] F. Vallet, J. Marcou, "A low-frequency optical accelerometer," *Journal of Optics-Nouvelle Revue d'Optique*, 29, (3), 152-155, Jun 1998.

[21] J. M. Lopez Higuera, M. A. Morante, A. Cobo, "A Simple low-frequency optical fiber accelerometer with large rotating machine monitoring applications," *Journal of Lightwave Technology*, 15, (7), 1120-1130, Jul 1997.

[22] D. Juckenack, "Sensors for measuring torque," *Sensors, Volume 7*, Edited by H. Bau, N.F. deRooij, J.N. Zemel, p.483-512, VCH Weinheim (1992).

[23] Product data: Lebow Products, "Load Cell and Torque Handbook No. 600A," PO Box 1089, Troy, Michigan, US.

[24] Application notes: LEM Instruments, "Digital torque sensing provides dynamic and static torque values without the use of mechanical sensors," Milwaukee, USA, (2000).

[25] Product data: Allied Controls Group, "Industrial and Automation Controls," http://www.allied-controls.com/documents/acs.pdf, Ontario, Canada, 2000.

[26] M. J. Corley, R. D. Lorenz, "Rotor position and velocity estimation for salient-pole permanent magnet synchronous machine at standstill and high speeds," *IEEE Transactions on Industry Applications*, 34 (4), 784-789, (1998).

[27] C. French, P. Acarnley, "Direct torque control of permanent magnet drives," *IEEE Transactions on Industry Applications*, 32 (5), 1080-1088, (1996).

[28] Product data: Sensor Technology Ltd, "E-Series Optical Rotary Torque Transducer," PO Box 36, Banbury, Oxon, UK, 1998.

[29] G. Reed, "Torque measurement in rotating shafts – the optical alternatives," *Design Engineering*, May 1989, 69-72.

[30] Secondary reference from [29], source no longer available.

[31] Secondary reference from [29], source no longer available.

[32] Guenther Ebi, Sensoplan GmbH, Hohentengen, Germany, Hans P. Zappe, CSEM, Zurich, Switzerland "Integrated optical noncontact torque measurement microsystem," *Optical Engineering*, 38 (2), 240-245, 1999.

[33] Product data: Sensor Technology Ltd, "A Primer on SAWs," PO Box 36, Banbury, Oxon, UK, 1998.

[34] B. Morten, G. Decicco, M. Prudenziati, "A novel torque sensor based on elastic waves generated and detected by piezoelectric thick films," *Sensors and Actuators A: Physical*, 41 (1-3), 33-38, (1994).

[35] P. Rombach, W. Langhinrich, "An integrated sensor head in silicon for contactless detection of torque and force," *Sensors and Actuators A: Physical*, 42 (1-3), 410-416, (1994).

[36] Product data: Hare Industrial Products Ltd, "Non contact Rotary Shaft Torque Sensor," http://www.hare.com.au/se0105.htm, 1998.

[37] D. Chung, F. L. Merat, F. M. Discenzo, J. S. Harris, "Neural net based torque sensor using birefringent materials," *Sensors and Actuators A: Physical*, 70 (3), 243-249, (1998).

[38] N. Whitehead, B. E. Jones, D. Rees, "Non-contact torque measurement on a rotating shaft incorporating a mechanical resonator," *Proceedings of Sensors and their Applications X*, Cardiff, (1999), 17-22.

[39] Product data: "MCRT Torquemeters," MCRT-Himmelstein, Illinois, USA, 1998.

[40] Product data: "Review of Dynamometers," vibro-meter, CA, USA, 1998.

[41] Product information: "Machine Condition Monitoring," http://www.fft.com.au/mcm.html, Future Fibre Technologies, Sydney, Australia.

[42] B. L. Agrawal, J. A.Demcko, R. G. Farmer, and D. A. Selin, "Shaft torque monitoring using conventional digital fault recorders," *Trans. Power Syst.*, 7, (3), 1211 (1992).

[43] K. F. Hale and B. E. Jones, "Tool wear and monitoring sensors," *Proceedings of 2nd International Conference COMADEM 90*, Brunel University, July 1990, Chapman and Hall, London.

[44] D. A. Smith, S. Smith, J. Tlusty, "High performance milling torque sensor," *Journal of Manufacturing Science and Engineering – Trans of the ASME*, 120 (3), 504-514, (1998).

[45] J. E. Kaye, D. H. Yan, N. Popplewell, S. Balakrishnan, "Predicting tool flank wear using spindle speed change," *International Journal of Machine Tools and Manufacture*, 35 (9), 1309-1320, (1995).

[46] T. A. Carolan, S. R. Kidd, D. P. Hand, J .S. Wilcox, P. Wilkinson, J. S. Barton, J. D. C. Jones, R. L. Reuben, "Acoustic emission monitoring of tool wear during the face milling of steel and aluminium alloys using a fibre optic sensor. 1. Energy analysis" *Proceeding of the Institute of Mechanical Engineers Part B – Journal of Engineering Manufacture*, 211 (4), 299-309, (1997).

[47] S. K. Choudhury, V. K. Jain, C. V. V. R. Rao, "On line monitoring of tool wear in turning using a neural network," *International Journal of Machine Tools & Manufacture*, 39 (3), 489-504, (1999).

Chapter 4

Single channel device for rotational frequency determination

4.1 Introduction

4.1.1 Overview

This chapter describes the development of a system to monitor the angular velocity of a rotating shaft by measuring optical reflections from the surface of the shaft. This process uses only naturally occurring variations in the reflectivity of the shaft without any alterations to the shaft whatsoever. The main focus of the research was on the application of the signal processing algorithms for frequency determination and methods of improving the clarity of the underlying periodic signals.

4.1.2 The Detector System

The general configuration of the system is shown in Figure 4.1. The sensor functions employing an optical fibre to capture the optical reflections from the surface of the rotating shaft that are then converted into an analogue electrical signal by a photodiode. Computer programs were developed to run continuously on a desktop PC to control the operations necessary for the determination of the speed of rotation of the shaft. Initially the signal is sampled using an analogue to digital converter (ADC) card residing in the PC digitising the signal to a resolution of 12 bits. This data is then stored as a series of digital values in a memory array before the signal processing operations of windowing and auto-correlation are performed to smooth the data. The frequency of the signal is determined using the mathematical algorithm of Fast Fourier transforms. The computer programs for implementing the signal processing are listed in the appendix.

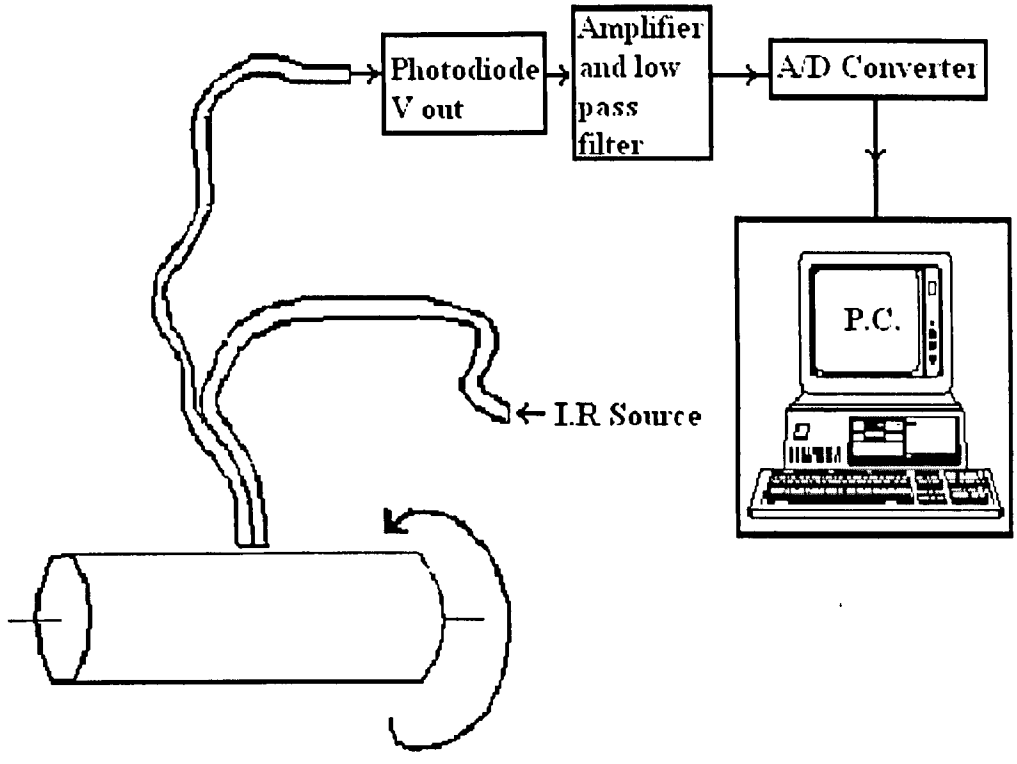

Figure 4.1 System configuration.

A numerical offset inherent in each data sequence is removed by the subtraction of the average of the sequence that is then re-stored in a memory array prior to the numerical processing. The offset occurs because the ADC has an input voltage range between -9 V to +9V. Since the resolution of the converter is 12 bits a digital value of 0 represents -9 V and 4096 represents +9 V meaning that 0 V corresponds to a digital value of 2048. The rate at which the data is converted, known as the sampling frequency (F_s), is controlled by a variable delay loop in the computer program. The effects of altering the sampling rate on the accuracy and resolution of the results were investigated.

The optical signal is obtained using a sensor head formed by jacketing together and then polishing down two separate optical fibres. Typically two 1.5 m lengths of

inexpensive multimode polymer fibre, core diameter 1 mm and numerical aperture 0.47, would be used with the sensor, although this could be altered to suit the application. One of the fibres transmits the output from an I.R. emitting diode, peak wavelength 880 nm, to the shaft where the reflections are captured by the other fibre. The sensor head is positioned to optimise the optical power recaptured with the fibre head usually being secured between 1 mm and 2 mm from the shaft. Typically 50 μW of optical power would be transmitted to the shaft of which 0.1 μW would be returned by the other fibre.

The signal produced by the photodiode is fed into an electronic circuit, as shown in Figure 4.2, which includes an amplifier to generate a signal from the opto-electronic transducer and a low pass filter to cut out unwanted high frequency noise elements. The section of the circuit involving the photodiode and op amp A was taken from a RS data sheet [1]. The photodiode chosen was a BPX65 which offers a high frequency response with peak spectral response in the near IR region. In the circuit the photodiode is reverse biased in order to increase frequency the response. The reverse bias increases the semiconductor depletion layer is increased thus decreasing the junction capacitance. Due to the small current produced by the photodiode, in the order of micro amps, a large gain is provided by op amp A, which operates in a current to voltage amplifier mode, with the input ac coupled in order to provide isolation from changing ambient conditions. The op amp used was a JFET type LF351 which offers good noise reduction characteristics due to its low input bias current and it also offers a high maximum slew rate.

Op amps B, C and D provide further signal conditioning and bipolar dual and quad type MC33172 and MC 33174 op amps were used. Op amp B is a buffer to separate the two halves of the circuit stopping oscillations that occurred at certain operating frequencies when the filter, op amp D, was added. Op amp C is an inverting amplifier with fixed gain of unity and was included in case extra gain might be required. However the ADC card is also capable of providing extra gain, adjusted through software control, but was normally set to unity during the experimentation. Op amp D acts as a low pass filter whose cut off frequency may be adjusted by altering the components. In this set up the 3 dB drop off point is about 300 Hz.

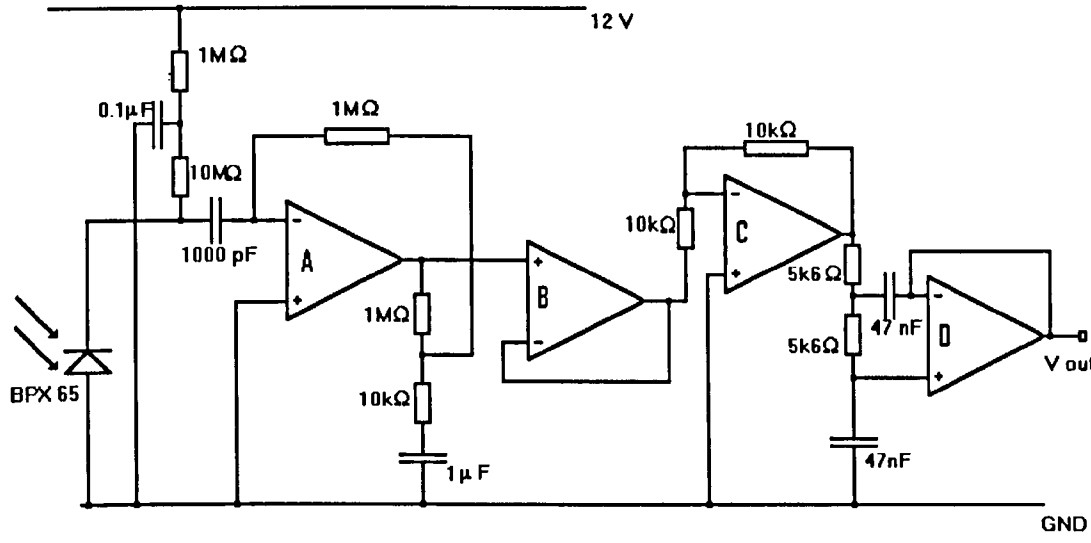

Figure 4.2 Circuit diagram of photodiode amplifier and filter circuit

4.2 Signal Processing

As this project progressed the main focus of the work undertaken shifted rapidly from the development of the electronic instrumentation associated with the sensor onto the development and application of the signal processing algorithms to be applied to the signals obtained by the sensor. These algorithms concentrated on the determination of the frequency, and methods of improving the clarity of the underlying periodic signals inherent in the data. Therefore a brief description of these algorithms and the fundamentals of digital sampling are presented here.

4.2.1 Frequency determination

The simplest method of frequency determination is that of measuring the interval at which a signal passes through the zero value. This is termed a zero-crossing technique and is extremely simple since it only involves noting the occurrence of successive samples that have opposite algebraic signs. Assuming a pure sinusoidal signal is being analysed, and counting from a given change of sign there will be two changes of sign per period. However, not all signals consist of a single tone. If higher order harmonics, DC offsets from the A/D converter or other sources, and in particular 50 Hz mains hum, are added the distortions may cause the signal to change sign more than twice per period. Therefore methods of spectral analysis were investigated in order to provide a better understanding of the spectral content of the signals obtained from the sensor.

Fourier transforms are an effective method of representing time domain signals in the frequency domain and involve integrating a time domain signal to work out the energy density spectrum in the frequency domain. The integration is performed using a finite mesh. However, if a sequence is periodic it is known that it can be represented by a

series of discrete summations known as the Discrete Fourier Transform (DFT) [2] such that

$$X(k) = \sum_{n=0}^{N-1} x(n)\, e^{-j(2\pi/N)nk}, \qquad k = 0,1,2,....,N-1 \qquad .....(1)$$

where the k values represent an ascending sequence of harmonics.

The calculation of the DFT requires a number of operations that increases with the square of the number of samples in the sequence being processed. This would prove time consuming even on a PC if a reasonable sample length is to be used. However Fast Fourier transforms (FFT) reduce the number of calculations required considerably by recognising that many of the calculations are repeated and redundant. The use of the FFT is the basis upon which most of the experimentation undertaken so far has been carried out.

4.2.2 Sampling Considerations

Before the FFT algorithm can be applied the signal must be described in digital form which, as mentioned earlier, was achieved by using an analogue to digital converter. The most important consideration in the conversion process is choosing the most appropriate sampling frequency. The sampling theorem [3] tells us that if the highest frequency component in a signal is f_{max} then the signal must be sampled at a rate greater than $2.f_{max}$ for the samples to represent the signal completely:

$$F_s \geq 2 f_{max} \qquad .....(2)$$

where F_s is the sampling frequency. In this system the highest frequency was governed not only by the speed of rotation of the shaft but also by the degree of surface

resolution required in order that accurate and repeatable results could be produced. If the shaft were rotating with a frequency of 100 Hz and a surface resolution of one degree was required then a sampling rate of 72 kHz would be required.

As a consequence of the sampling process the digitally sampled signal when represented in the frequency spectrum will have the same spectrum as the original analogue spectrum and also repeat itself at multiples of the sampling frequency, F_s. The repeated spectra are centred on multiples of F_s and are referred to as image spectra. If F_s is not high enough then the image spectra overlap into the base spectrum. This is called aliasing and it is impossible to distinguish between the original and the imaged data. The overlap mirrors itself about a point called the folding or Nyquist frequency, that being equal to half the sampling frequency. In any system aliasing will always be a problem due to noise and signals outside the frequency range of interest. The sampling frequency has to be chosen at a suitable value to avoid overlap and the anti-aliasing filter has to be set so as to limit noise and exclude signals of frequency above the range of interest.

Once FFT's are applied the resolution of the resultant frequency spectrum, Δf, which determines the sensitivity of the results obtained from the spectrum, is also dependent on the sampling frequency as well as the sample length. The relationship is:

$$\Delta f = \frac{F_s}{N} \qquad (3)$$

This follows from the definition of the Fourier coefficients given in equation (1) whereby the resultant spectrum is divided up into N multiples of the fundamental frequency. The sampling frequency must be at least twice the Nyquist frequency in

order to avoid aliasing meaning that at least two periods of the fundamental frequency must be present in the data series captured in order for it to be recognised by the calculations.

Since F_s is equal to the number of samples, N, divided by the period of sampling for each series of data, T, it can be seen that the resolution, Δf, equals the reciprocal of T.

$$\Delta f = \frac{1}{T} \quad \text{.....(4)}$$

This implies that if a frequency resolution of 1 Hz is required in the resultant frequency spectrum then the period of sampling must be 1 second.

The maximum speed that the ADC is capable of operating at is about 75 kHz. If the shaft being monitored is rotating at 34 Hz, i.e. about 2000 rpm, at the 75 kHz sampling rate 2200 points would be required to map each period of revolution completely. Higher speeds of rotation might well be encountered and so that at least two full periods may be captured sample lengths of up to 10,000 points might have to be considered. This would put considerable strain on memory capacity and increase the time required for computation too much to achieve an acceptable rate of update. Using a slower rate of capture will create less data therefore speeding up the computation time, however this is at the expense of surface resolution meaning that more periods of revolution must be monitored in order to obtain sufficient data for the calculation of accurate results.

Figure 4.3 below shows a complete sequence of 1024 data points taken from a shaft one cm in diameter rotating at a at frequency of 34 Hz. The sampling rate of the ADC

was 10 kHz. The periodicity of the signal is clear and a large amount of surface detail can be made out. More than three complete periods of shaft rotation are captured meaning a surface resolution of one point per degree is achieved thus providing sufficient data to ensure the calculation of accurate results.

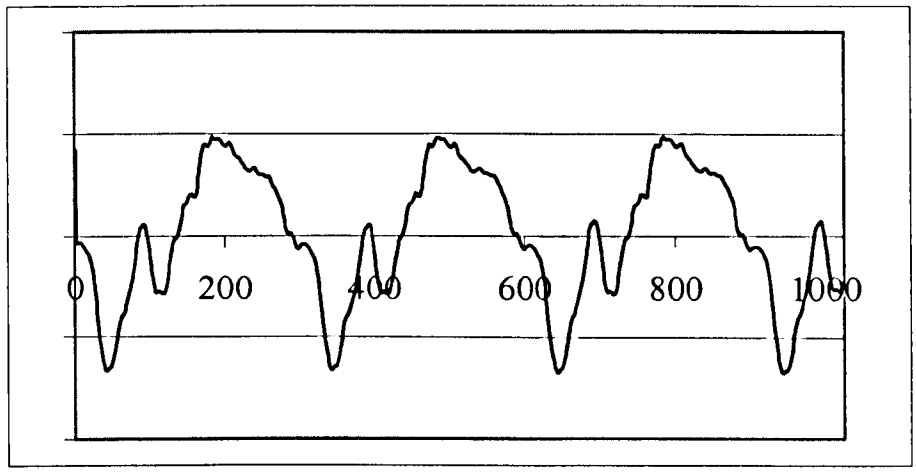

Figure 4.3. 34 Hz signal, Fs = 10.24 kHz.

Figure 4.4 shows the result of applying FFT analysis to the data series shown in Figure 4.3. The scale of the y-axis is arbitrary showing the relative amounts of power for each frequency component present in the signal. The x-axis shows the frequency in steps of k, which are increasing multiples of the fundamental frequency. This defines the frequency resolution of the spectrum, which in this case is 10 Hz.

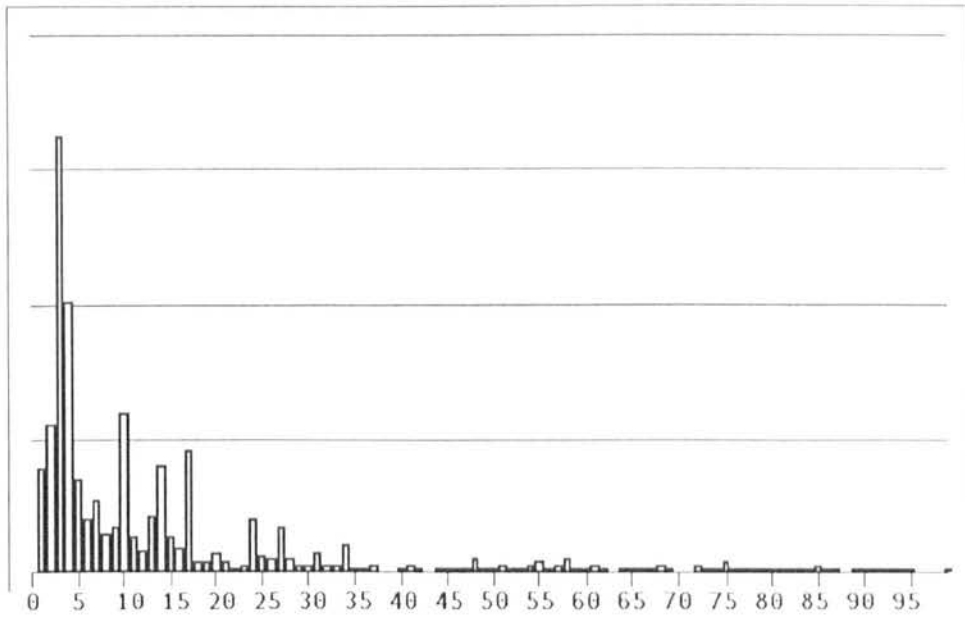

Figure 4.4 FFT of 34 Hz signal, Fs = 10.24 kHz, resolution = 10 Hz/bin.

From the spectrum it can be seen that the FFT analysis has clearly identified the major frequency component as k=4 which represents a frequency between 30 Hz and 39 Hz which includes the known frequency of 34 Hz. The peak for that frequency is a factor of two higher than any other peak and part of its power has spread slightly into the frequency region below. The power in the region where k=0 is zero confirming that the system has been effectively ac coupled. There is a small peak where k=17 corresponding to a frequency of 170 Hz which is generated by the fifth harmonic of the signal. If Figure 4.3 is studied it can be seen that there are five small peaks in each period.

However, if the speed of rotation were to double not enough periods would be present meaning that a longer data series would be required. Since the total number of readings required in a sample set for a FFT calculation must be a power of two 2048 points would therefore have to be taken to ensure enough periods were included. This would

have the effect of improving the frequency resolution of the result spectrum but increase the calculation time required.

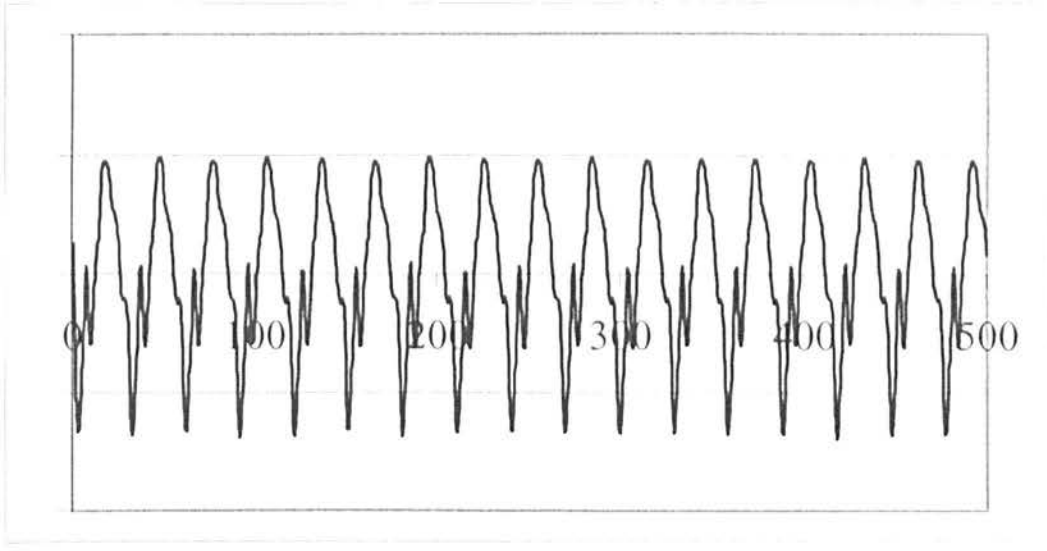

Figure 4.5 500 points out of 1024 point signal of shaft rotating at 35 Hz.

Fs = 1.024 kHz.

A reconstruction of a sequence of 500 data points out of a total series of 1024 points taken from the same shaft also rotating at 35 Hz is shown in Figure 4.5. The sampling rate of the ADC was 1kHz. The periodicity of the signal is clear to see and at least 30 periods are present within the sample and this is more than enough to give accurate results.

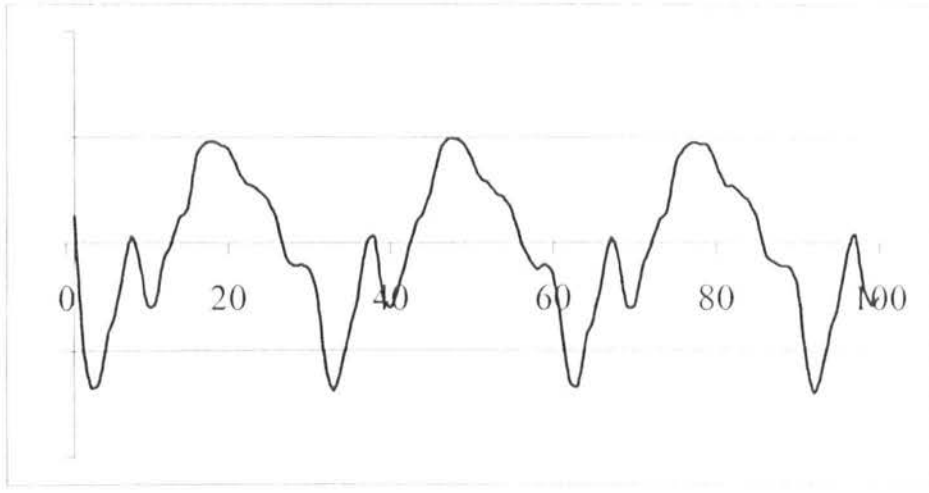

Figure 4.6 100 points out of 1024 point signal of shaft rotating at 35 Hz.

Fs=1.024 kHz.

An expanded view of a portion of 100 points from the signal shown in Figure 4.5 is displayed in greater detail in Figure 4.6. The variations in reflectivity picked up by the sensors are highlighted and it can be seen that there are a number of sub peaks in each of the fundamental periods.

Figure 4.7 below shows the frequency spectrum obtained by performing FFT analysis on the above signal. The fundamental frequency stands out clearly at 34 Hz and the higher order harmonics are visible at increasing multiples of that. It may be noted that the fifth harmonic stands out above the surrounding harmonics. If Figure 4.7 is investigated it may seen that there are five discernible sub-peaks in each period.

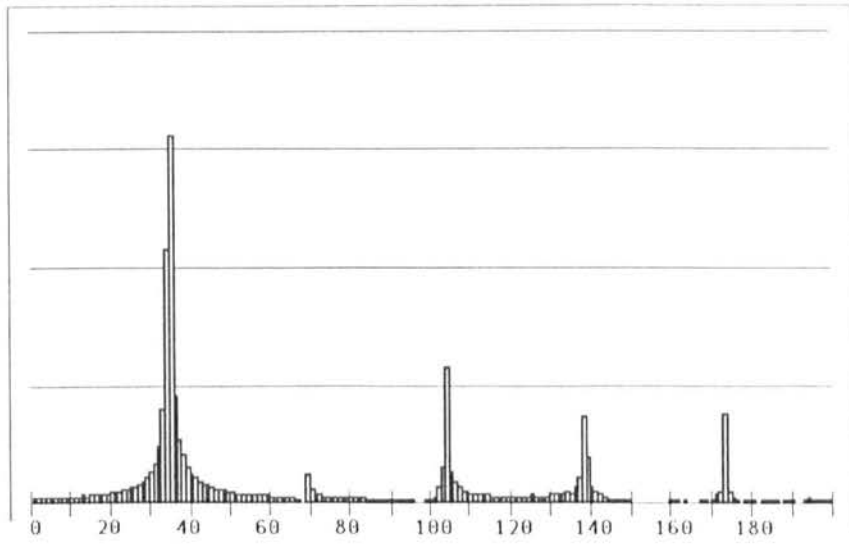

Figure 4.7 FFT spectrum of 35 Hz signal, Fs = 1.024 kHz, resolution = 1 Hz/bin.

With the system configured to take 1024 points per series at a sampling rate of 1024 Hz the resolution of the spectrum will be 1 Hz. Each series takes one second to capture so the rate of update is one second plus the computation time.

From the two examples presented it can be seen that a compromise has to be made between the frequency resolution of the system and the rate of update of the results. A frequency resolution of 10 Hz gives a poor sensitivity to changes in rotational speed since the range of typical shaft rotational speeds tested was between 5 Hz and 100 Hz. A resolution of 1 Hz is much more desirable. To improve the frequency resolution either the sampling rate must be reduced or the sample length increased. Reducing the sampling rate too far causes aliasing whereby components whose frequency is more than half that of F_s will be mistakenly represented as a frequency of less than half F_s. The use of the low pass anti-aliasing filter for the removal of high frequency components alleviates this danger but sets a maximum rotational velocity to the shaft being monitored. The other option, taking more data, increases the duration of sampling for each series and more than doubles the computation time.

4.2.3 Techniques for improving signal clarity

The examples shown in the previous section during the discussion concerning sampling rates gave unambiguous results when the FFT spectrum was analysed with the fundamental harmonic of the signal always containing more power than the higher order harmonics. However, not all sections of shaft give such unambiguous results, often one or more of the higher order harmonics dominate the fundamental signal. This is demonstrated in the following examples.

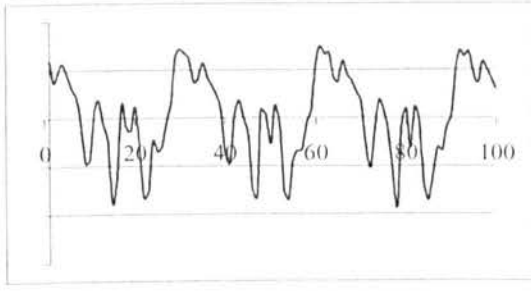

Figure 4.8 Signal producing clear spectrum.

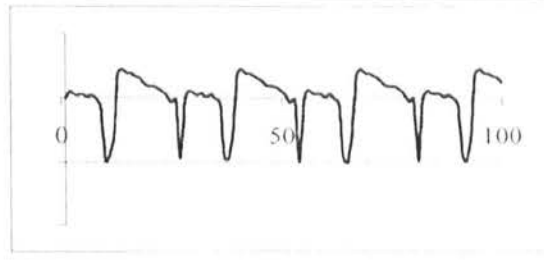

Figure 4.9 Signal producing ambiguous results.

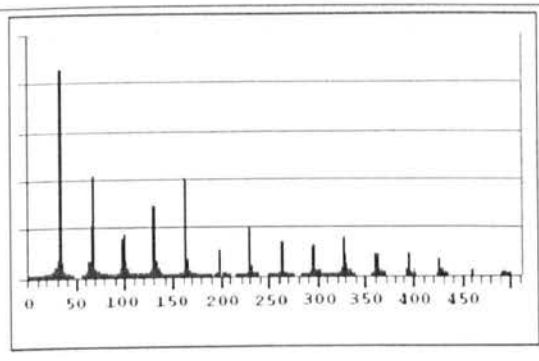

Figure 4.10 Clearly defined result spectrum.

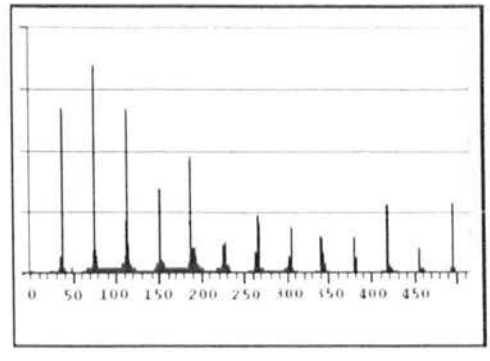

Figure 4.11 Ambiguous spectrum

The signals in Figures 4.8 and 4.9 show portions of 100 points each representative of sample sets of 1024 points taken with a sampling rate of 1.024 kHz from shafts revolving at 38 Hz upon which FFT analysis was performed. It can be seen that the signal shown in Figure 4.8, although having a lot of surface detail visible, gives the

resulting spectrum shown in Figure 4.10 where the fundamental frequency peak at 38 Hz clearly has more power than the higher order harmonics. However, the surface profile shown in Figure 4.9 is smoother with just a couple of sharp dips visible and produces a resulting spectrum where the second and third harmonics at 76 Hz and 114 Hz contain more power than the fundamental peak at 38 Hz. Although there is a clear peak at 38 Hz shown in Figure 4.11 the presence of the more powerful higher harmonics make the determination of the correct frequency difficult since picking the frequency of highest power will produce an erroneous result.

When a segment of a continuous signal is digitally sampled and stored it is as though a window has been thrown over that signal. The operation of windowing has a smoothing effect on the process of Fourier transforms and by modifying the shape of the window applied this effect may be utilised so that the fundamental harmonic stands out more strongly. This operation has been discussed in detail in Chapter 2. Another method for improving signal clarity is auto-correlation. The auto-correlation function is built up through repeated shift and cross multiplication of the signal by itself thus enhancing the periodic components of the signal. This procedure was also investigated and is discussed in the following section.

Even after windowing and auto-correlation have been performed on the sampled data the peak in the Fourier spectrum representing the fundamental frequency may still be outweighed by the stronger higher order harmonic components. In an attempt to overcome this problem an algorithm was developed in order to check the ratios of the frequency of the various peaks present in the spectrum. The fundamental frequency is

differentiated from the harmonics by looking for the peak whose frequency is that of the lowest common denominator of the peaks present.

4.3 Discussion of results

The two sets of graphs, Figures 4.12 to 4.18 and Figures 4.19 to 4.25, demonstrate the effects of various sampling windows on the captured data. Data series of 1024 points captured with a sampling rate of 1.024 Hz were taken from the same section of shaft rotating at speeds of 5 Hz and 37 Hz. Six different data windows were applied to the data, including the case of the rectangular window where the original data is not modified. It can be seen by considering the relative heights of the peaks in the spectra taken at 5 Hz that the process of windowing does not have a significant effect in improving the dominance of the signal from the fundamental frequency. What may be observed is the difference in the width of the peaks and the levels of the background noise. These are factors that can affect the reliability of the results.

Looking at the second set of spectra taken at the higher speed of rotation on the same point on the shaft it can be seen that now the fundamental peak stands out clearly above the higher order peaks giving an unambiguous result. Also there is no significant background noise and the windowing process has clearly attenuated the level of the higher order peaks. This shows the benefit that capturing a high number of complete periods of data in the sample series gives to the final result

Figures 4.26 to 4.32 also show a series of spectra again taken with the same sampling windows on a different shaft rotating at 5 Hz. In this case peak of the fundamental harmonic is much smaller than the peaks representing the higher order harmonics. As

with the graphs shown in Figures 4.12 to 4.18 the relative ratios of the peaks have not been altered significantly by the different windows. With the rectangular window there is less spreading of the peaks, especially in the lower order harmonics. This limits the possibility that a particular frequency may have more total power within the signal but its peak value be lower than a frequency whose power is all concentrated into one bin, thus causing a false result to be obtained. This is illustrated in Figure 4.26. This means there will be less ambiguity in cases where the speed is midway between two frequency bins.

In this set of data the Hamming window gives the best reduction in background noise. At low speeds this can be significant since, with a spectral resolution of 1 Hz, with speeds below 5 Hz the peaks in the spectrum are closely packed so that the sidelobes of one peak may interfere with an adjacent peak. This effect will cause more uncertainty in the results when the power associated with one particular frequency is spread between two bins since the peak level will be lower and there will be less separation between peaks.

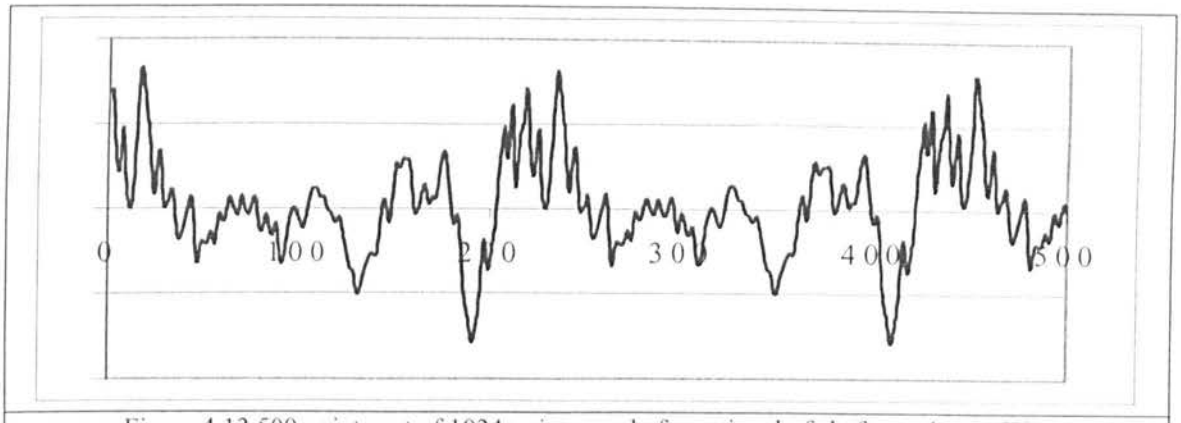

Figure 4.12 500 points out of 1024 point sample from signal of shaft rotating at 5Hz.

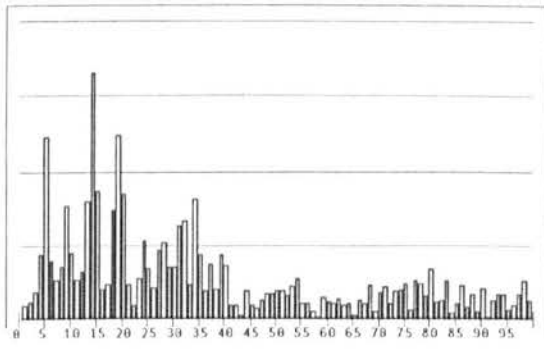

Figure 4.13 Frequency spectrum of above signal sampled using Rectangular window.

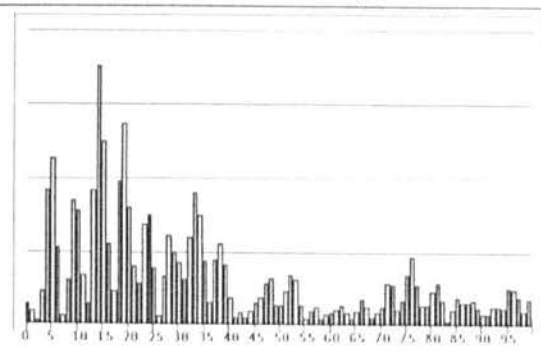

Figure 4.14 Frequency spectrum of above signal sampled using Blackman window.

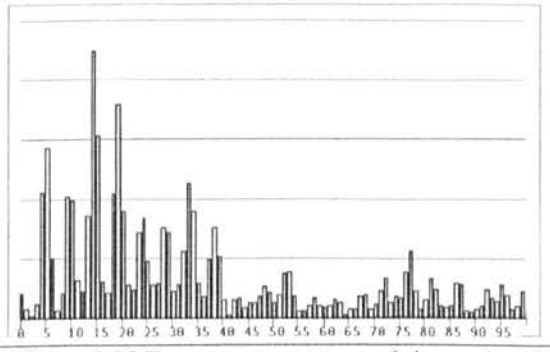

Figure 4.15 Frequency spectrum of above signal sampled using Hanning window.

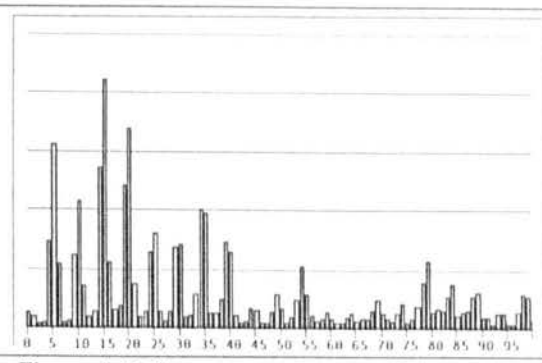

Figure 4.16 Frequency spectrum of above signal sampled using Hamming window.

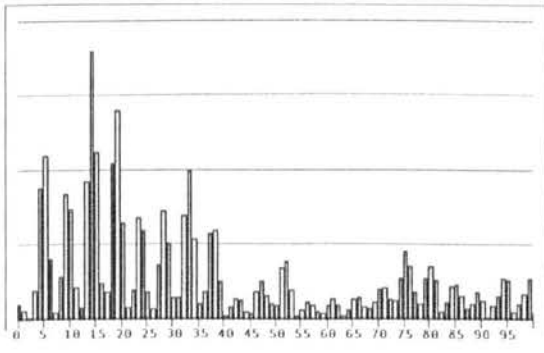

Figure 4.17. Frequency spectrum of above signal sampled using Blackman Harris 3 term window.

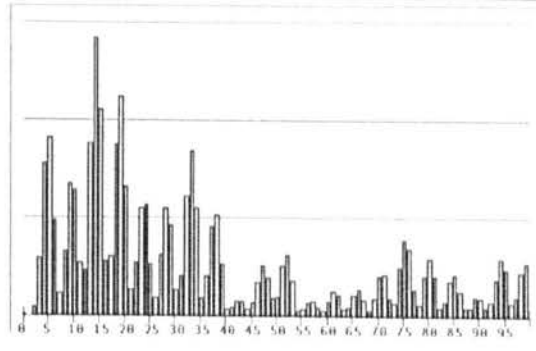

Figure 4.18 Frequency spectrum of above signal sampled using Blackman Harris 4 term window.

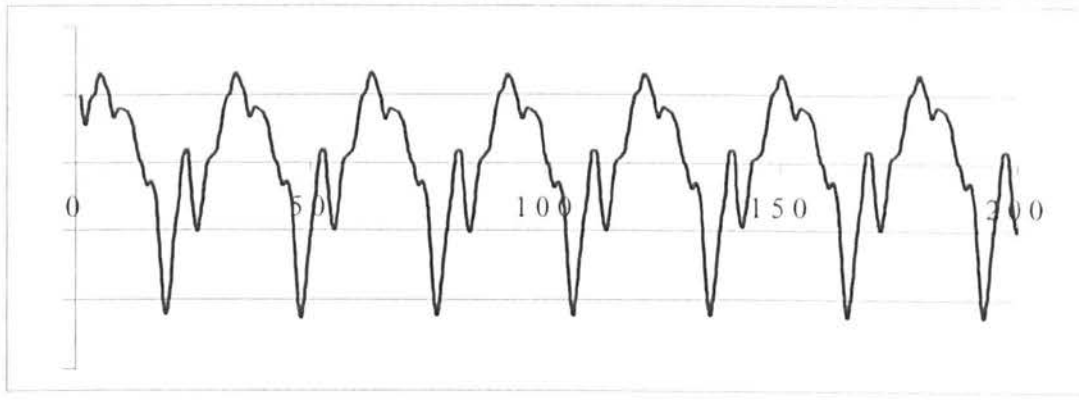

Figure 4.19 200 points out of 1024 point sample from signal of shaft rotating at 37 Hz.

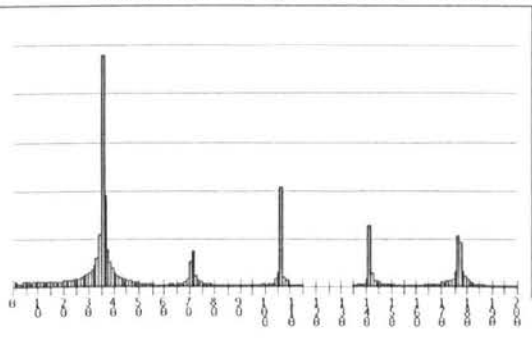

Figure 4.20 Frequency spectrum of above signal sampled using Rectangular window.

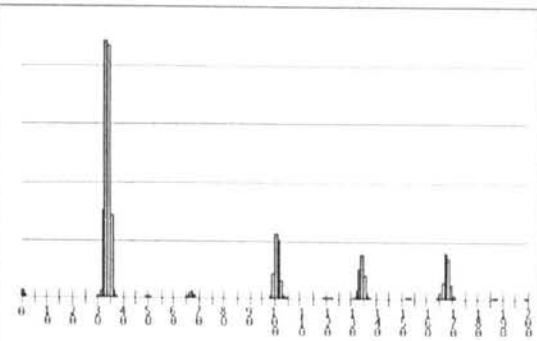

Figure 4.21 Frequency spectrum of above signal sampled using Blackman window.

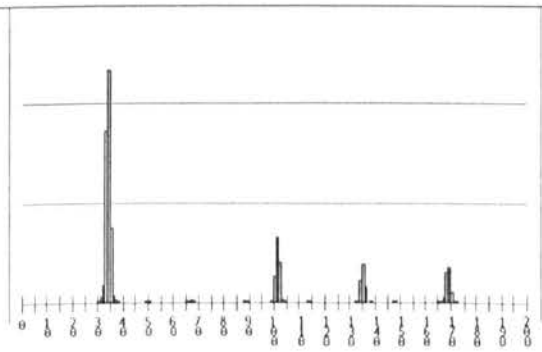

Figure 4.22 Frequency spectrum of above signal sampled using Hanning window.

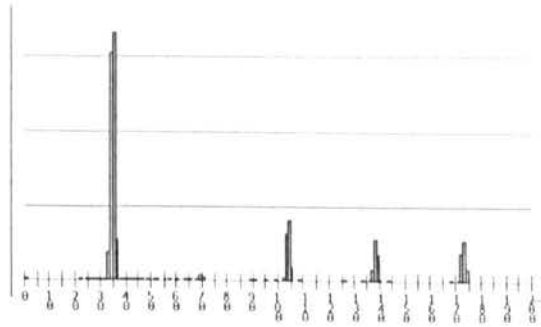

Figure 4.23 Frequency spectrum of above signal sampled using Hamming window.

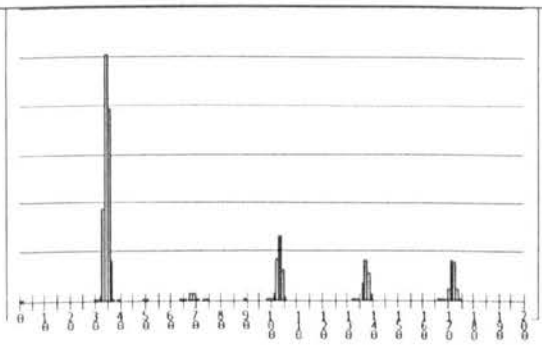

Figure 4.24 Frequency spectrum of above signal sampled using Blackman Harris 3 term window.

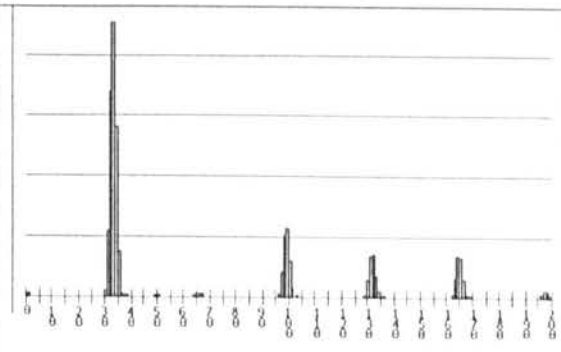

Figure 4.25 Frequency spectrum of above signal sampled using Blackman Harris 4 term window.

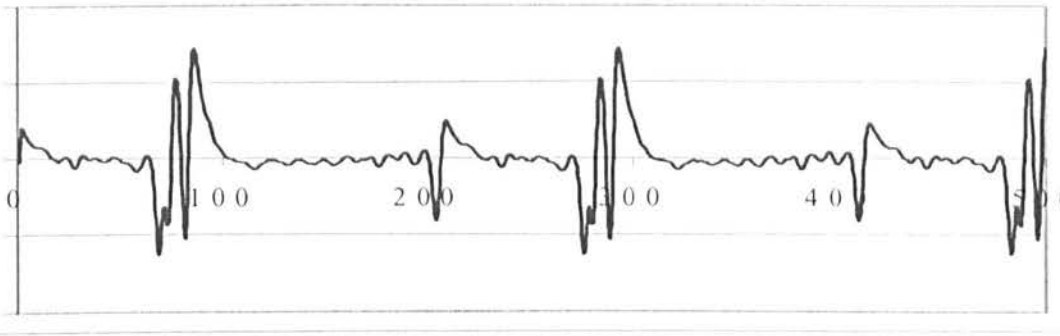

Figure 4.26 500 points out of 1024 point sample from taken signal of shaft rotating at 5Hz.

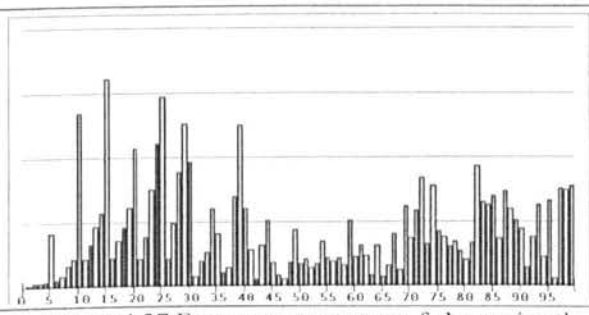

Figure 4.27 Frequency spectrum of above signal sampled using Rectangular window.

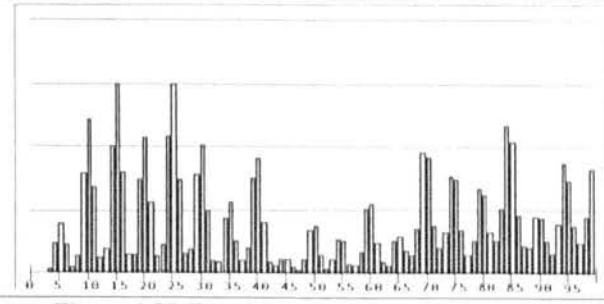

Figure 4.28 Frequency spectrum of above signal sampled using Blackman window.

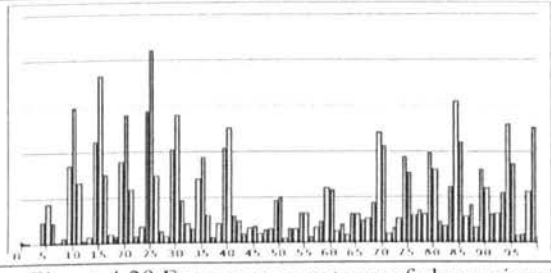

Figure 4.29 Frequency spectrum of above signal sampled using Hanning window.

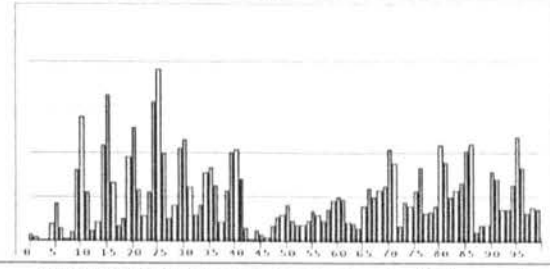

Figure 4.30 Frequency spectrum of above signal sampled using Hamming window.

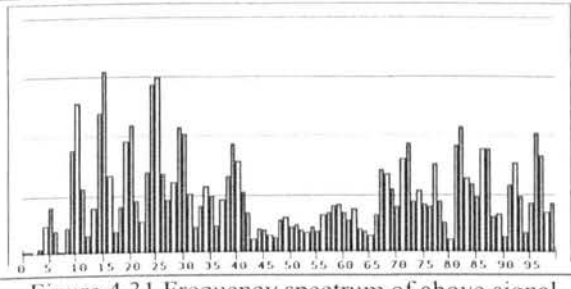

Figure 4.31 Frequency spectrum of above signal sampled using Blackman Harris 3 term window.

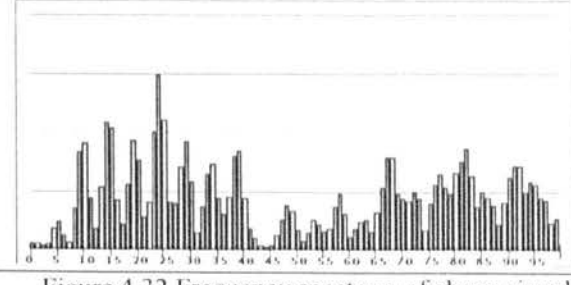

Figure 4.32 Frequency spectrum of above signal sampled using Blackman Harris 4 term window.

Comparison of the spectra taken at 5 Hz and at 37 Hz show that the peak broadening effects on the spectra of the windows are broadly as expected when compared to the theoretical data shown previously in Table 2.3. This is shown in more detail in Table

4.1 where the first twelve frequency bins, encompassing the first two peaks, are plotted.

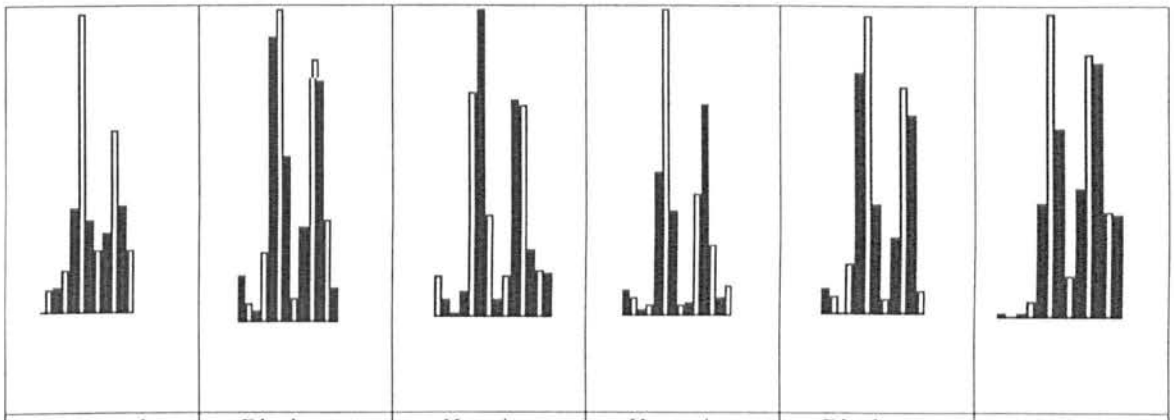

Rectangular window	Blackman window	Hanning window	Hamming window	Blackman Harris 3 term	Blackman Harris 4 term

Table 4.1 Expanded version of the first two peaks of Figures 4.12 to 4.18.

It can be seen from Table 4.1 that with the family of Blackman and Blackman-Harris windows the signal energy has been spread out over four bins whereas the Hanning and Hamming windows keep the signal energy associated with each frequency more concentrated within the central bin. The Rectangular window has the most concentrated fundamental peak but it also suffers from the highest level of background noise. This is because with the shaft rotating at 5 Hz the separation of the harmonic peaks being only 5 Hz the side lobes of the main peaks cause the peaks to merge into each other. This is not crucial in these examples since the peaks are quite distinct but in cases where there is a weak signal or noise contamination the choice of window might prove significant.

The Blackman–Harris 4 term window exhibits a similar merging of peaks with the Hamming window giving the best peak separation. This implies that a lower 3dB

bandwidth is the most important criterion when choosing a window for this purpose since Blackman and Blackman-Harris windows have superior sidelobe cancellation characteristics but gave worse overall results of the spectra captured in terms of the clarity of the peaks.

4.3.1 Detailed harmonic analysis

In order to quantify the relative effects of the various windows considered more detailed readings were taken on a section of shaft rotating at 11 Hz giving a frequency spectrum containing a complicated harmonic response. Typical spectra for each window are shown in Figures 4.33 to 4.38. The raw data for each spectra up to the sixth harmonic peak was analysed to determine the percentage power of the background noise to the highest adjacent harmonic peak. Also the sidelobe fall off was analysed by calculating the percentage of the average power contained in the two bins of the sidelobe on either side of the peak relative to the power of that peak.

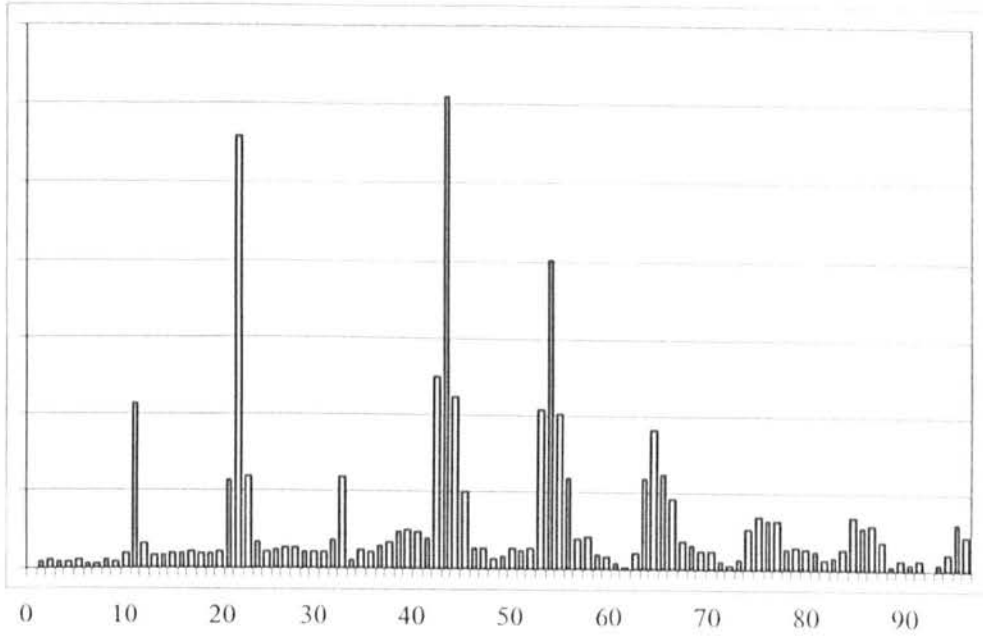

Figure 4.33 Spectrum obtained from shaft rotating at 11 Hz with Rectangular window applied

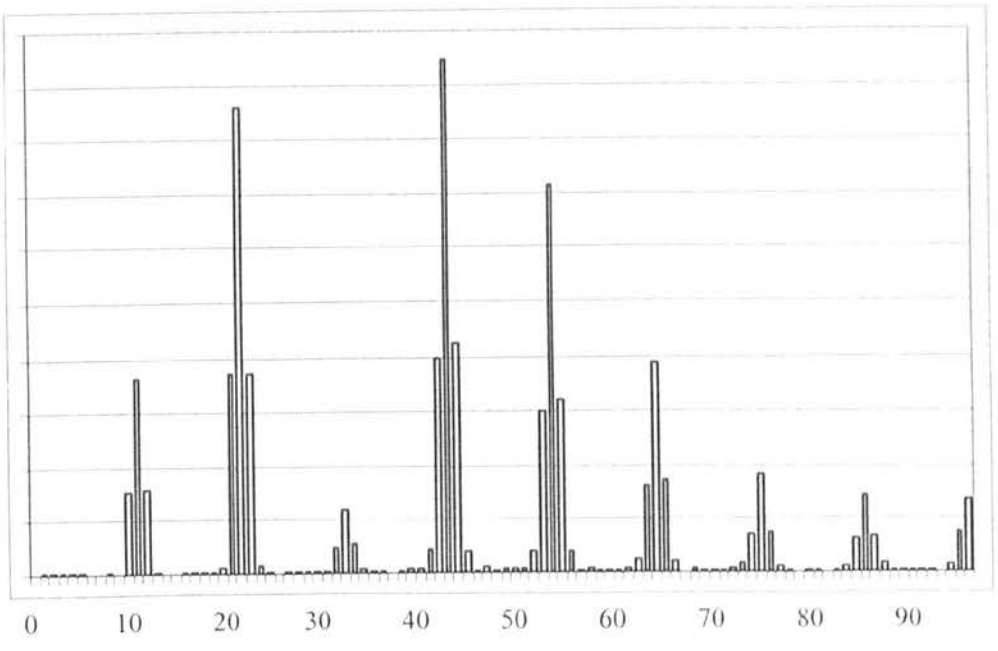

Figure 4.34 Spectrum obtained from data with Hammimg window applied

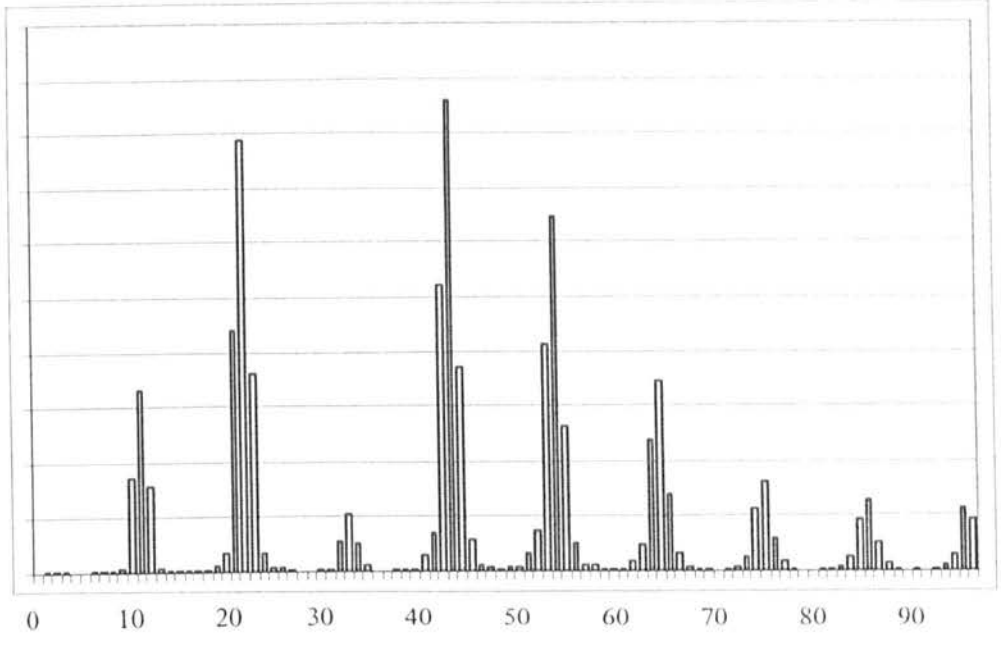

Figure 4.35 Spectrum obtained from data with Hanning window applied

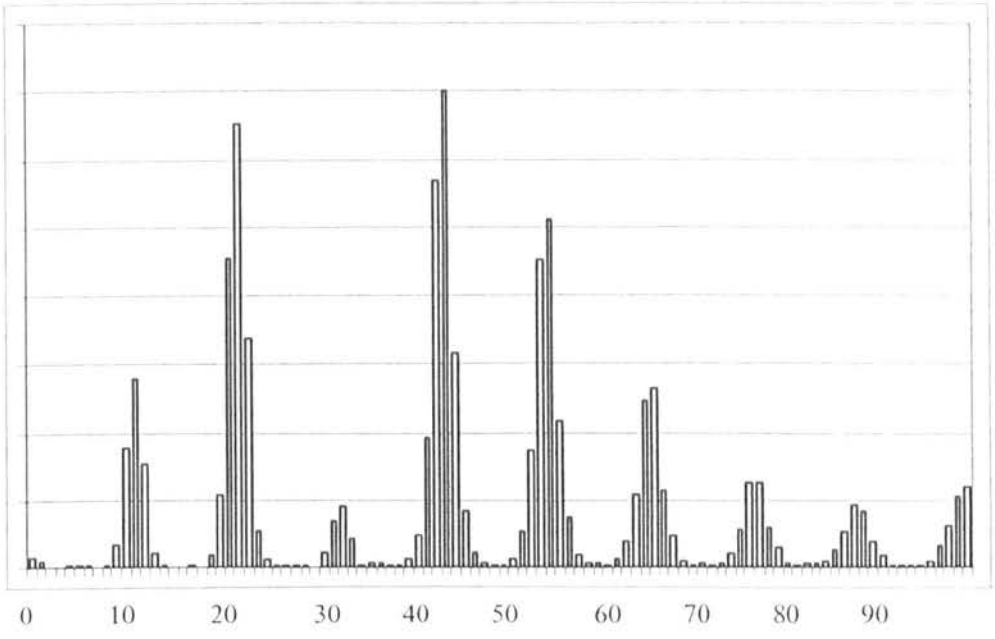

Figure 4.36 Spectrum obtained from data with Blackman window applied

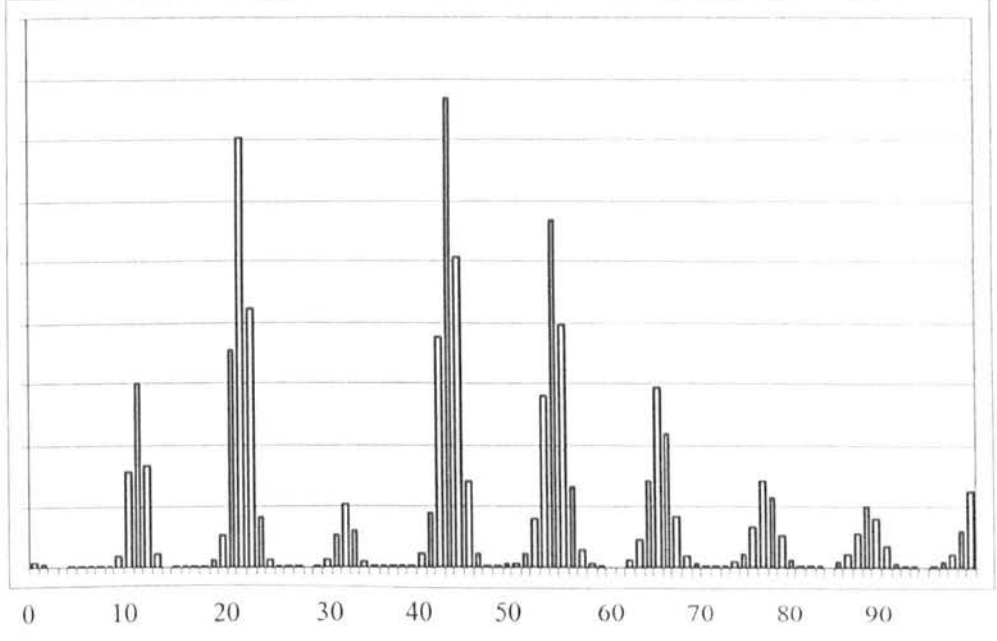

Figure 4.37 Spectrum obtained from data with Blackman Harris 3 term window applied

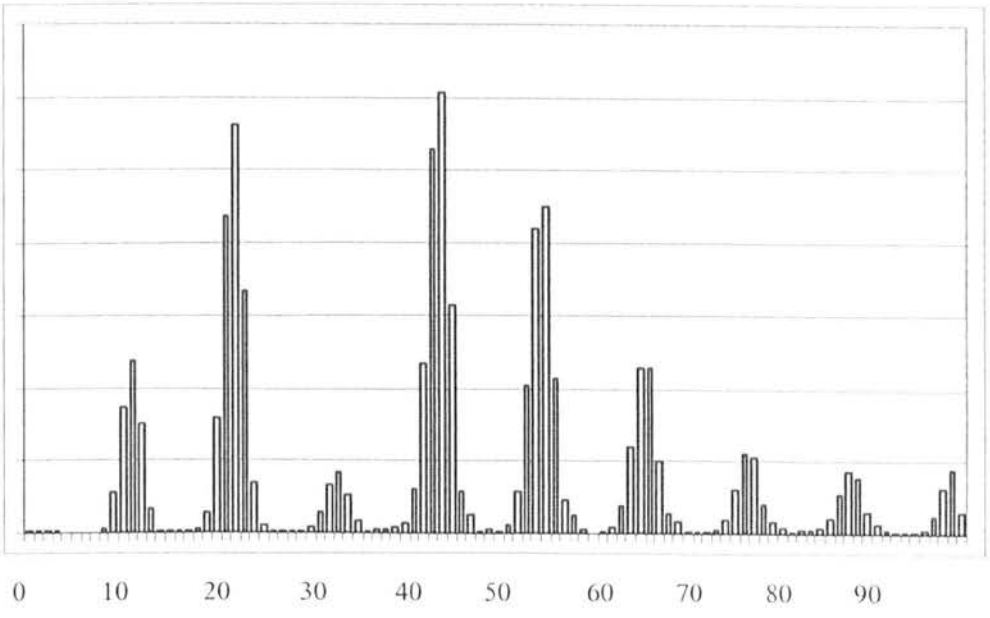

Figure 4.38 Spectrum obtained from data with Blackman Harris 4 term window applied

	0 to 1st	1st to 2nd	2nd to 3rd	3rd to 4th	4th to 5th	5th to 6th
Rect	5.4	9.2	3.2	41.9	6.8	23.4
Hamming	1.1	0.8	2.5	6.3	0.7	1.9
Hanning	1.5	1.1	5.7	2.9	1.0	0.15
Blackman	1.3	1.4	6.8	11.9	0.9	2.3
Blackman Harris 3 term	0.8	1.5	1.9	4.3	1.4	0.5
Blackman Harris 4 term	1.0	0.8	5.3	5.3	1.1	0.4

Table 4.2 Comparison of the percentage background noise in between harmonic peaks for spectra of various windows shown in Figures

From Table 4.2 it can be seen that all the windows give a significant reduction in background noise compared to the standard Rectangular window. With the exception of the Blackman window, which has noticeably higher background noise between the second and third, third and forth, and fifth and sixth harmonics, the other weighted windows are all broadly similar in this respect.

	0 to 1st	1st to 2nd	2nd to 3rd	3rd to 4th	4th to 5th	5th to 6th
Rect	11.6	20.9	19.0	38.7	51.1	66.7
Hamming	43.2	46.1	45.2	43.5	43.7	43.4
Hanning	49.7	50.4	52.9	51.8	52.4	54.0
Blackman	59.3	60.4	61.2	63.3	65.2	68.5
Blackman Harris 3 term	54.4	55.3	56.8	57.8	59.7	61.8
Blackman Harris 4 term	67.7	68.4	71.1	69.5	70.4	71.6

Table 4.3 Comparison of percentage power contained in sidelobes relative to their main peak for spectra of various windows shown in Figures

Table 4.3 shows that the Hamming window has the lowest sidelobes of the windows considered with a slight advantage over the Hanning window that becomes more pronounced in the higher order harmonics. The Rectangular window gives distinct peaks in the lower order harmonics but the peaks become indistinct at higher orders.

The windows calculated using more sample function sequences do not appear to give a better performance to that of the Hamming and Hanning windows. In fact it is clear from examining the spectra of Figures 4.34 to 4.38 that the Blackman family of windows cause the power present in each peak to be spread over five bins rather than three for the Hamming or Hanning windows. This greater spreading makes peak identification more difficult since the peaks are less pronounced and this difficulty might be significant in less distinct spectra.

4.4 Peak ratio analysis

As seen in the previous section the spectral peaks of the higher order harmonics often outweigh the peak associated with the fundamental frequency, as shown in Figure 4.40, Figure 4.39 shows three complete cycles of the signal reflected from a shaft rotating at 13 Hz that produced this spectrum. The surface profile of the shaft shows a number of detectable features of varying prominence contained in each period that cause the strong higher order harmonic peaks to be produced by the FFT analysis as illustrated by the spectrum. It can be seen that the second and third harmonics are twice as powerful as the fundamental and that a dozen harmonic peaks have a magnitude greater than 20% of that of the highest peak. An algorithm was developed to check the ratios of the frequency values of the peaks to determine whether a peak of lower power relative to succeeding peaks might represent the fundamental frequency.

Figure 4.39 250 out of 1024 points of signal resulting in spectrum with many harmonics.

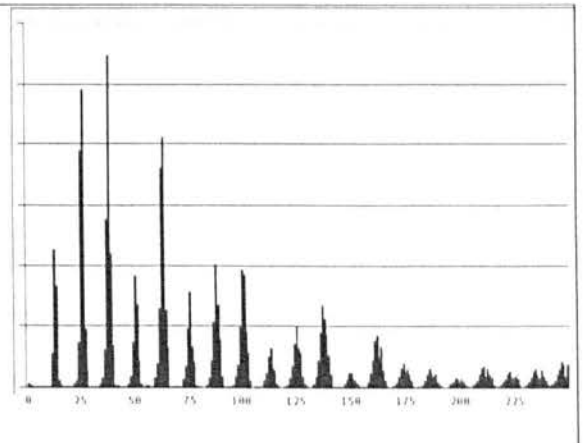

Figure 4.40 Spectrum produced by signal shown in Figure 3.35. F_s = 1.024 kHz.

The algorithm functioned by first identifying and storing the frequency and magnitude of all the peaks in the spectrum up to a frequency of 100 Hz whose power was greater than 10% of the value of the highest peak. This level was chosen arbitrarily to reduce the chance of spurious low power noise signals causing erroneous results since it was found that in none of the shafts tested was the value of the fundamental peak less than

20% of that of the maximum higher order peak. Initially it is assumed that if the highest peak detected is also the first peak in the list then it is assumed that the frequency at which this peak occurs is that of the fundamental frequency.

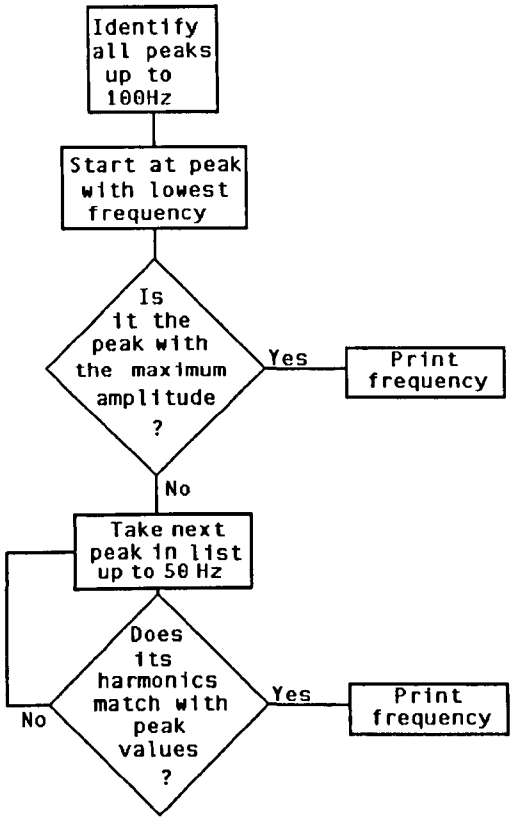

Figure 4.41 Flow chart showing basic logic of fundamental determining algorithm

If the first peak does not possess the greatest magnitude then the possible higher order harmonic frequencies that would be generated by that peak are compared to the frequency of all the succeeding peaks in the list. If the system is producing results to a resolution of 1 Hz then the maximum systematic error in each reading is $\pm$ ½ Hz., therefore for the shaft rotating at 13 Hz an error of up to 3.8% could be present in the result. This error could propagate through to the value of the higher order harmonics. If more than 75% of the values fall close enough to the product of the suspected

fundamental times the harmonic number being tested for it is assumed that this represents the fundamental frequency. If the frequency being tested does not give higher harmonics that match well then the process is repeated by testing the next peak on the list by the same process. If none of the peaks give a good correlation of possible harmonics to the higher frequency peaks then a warning message is printed. The system may be checked in order to ascertain if a problem exists with the set up or if a bad section of shaft is being monitored.

The values of each harmonic present in the spectrum from Figure 4.40 are shown in Table 4.4 compared to the expected harmonic values.

Harmonic	1	2	3	4	5	6	7	8	9	10
Expected frequency Hz	13	26	39	52	65	78	91	104	117	130
Actual frequency Hz	13	26	38	51	63	75	87	100	112	125
Difference %	0	0	2.6	1.9	3.1	3.8	4.4	3.8	4.3	3.8

Table 4.4 Harmonic frequency data from Figure 4.40

This set of results narrowly satisfies the 75% criteria. It can be seen that the second harmonic matches exactly and that the maximum error present is 4.4%. The spectrum was generated from the data of the signal shown in Figure 3.35 and it can be seen that the surface detail is randomly spaced within each revolution and does not form a continuously distributed pattern resulting in different shaped harmonic peaks. The peak ratio analysis will work better when the frequency of the fundamental is close to a whole number. This means that the power within the fundamental peak is distributed symmetrically about the central bin.

Figure 4.42 120 out of 1024 points of signal resulting in spectrum with many harmonics.

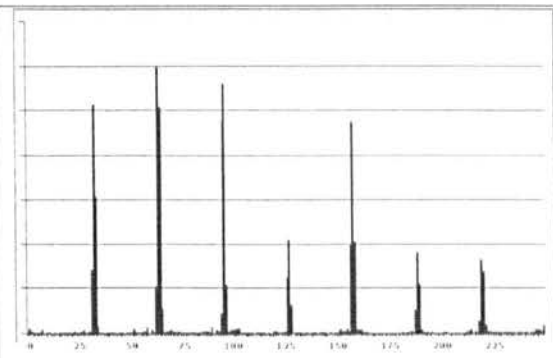

Figure 4.43 Spectrum produced by signal shown in Figure 3.35. F_s = 1.024 kHz.

Figures 4.42 and 4.43 show the signal and resultant FFT spectrum obtained from the same shaft rotating at 32 Hz. At the higher speed of rotation the fundamental peak is more prominent than at the slower speed but is still outweighed by the second and third harmonics. Table 4.5 shows the comparison between the frequency of the peaks and their expected values. The ±½ Hz range gives a maximum systematic error of 1.6 % in the fundamental reading for a shaft rotating at 32 Hz. It can be seen that two of the harmonic peak frequencies fall right on the limit of this error meaning that this set of readings would just pass the criterion. The balance of the adjacent bins to the fundamental peak is above 32 Hz whereas the position of the second harmonic at 63 Hz is lower than expected value of 64 Hz. This trend is continued in the fourth, fifth and sixth harmonics.

Harmonic	1	2	3	4	5	6
Expected frequency Hz	32	64	96	128	160	192
Actual frequency Hz	32	63	96	126	158	188
Difference %	0	1.6	0	1.6	1.2	2.1

Table 4.5 Harmonic frequency data taken from Figure 4.43

In all the tests conducted the first significant peak present was always that of the fundamental harmonic. When consistent readings were not obtained it was generally due to poor alignment of the fibre optic detectors. If the fundamental frequency, or the frequency value of the first peak, has a value below 5 Hz then the higher order harmonic peaks will naturally be packed closely together meaning that there is more chance of the multiples matching. At the lowest extreme, if there is a peak at 2 Hz then all of the peaks of even number frequency will match to a higher harmonic meaning that there is a high possibility of erroneous results being given.

4.5 Auto-correlation

The use of auto-correlation is accepted as a powerful method of overcoming noise and improving the clarity of periodic signals. The discrete correlation of two sampled functions x_1 (n) and x_2 (n), each containing N data points, is defined as follows [4]

$$R_{x_1x_2}(p) = \sum_{m=0}^{m=N-1} x_1(m)x_2(p+m) \quad \text{.....(5)}$$

The correlation of a function with itself is known as auto-correlation. The cross multiplication of the sequence by itself has the effect of enhancing the periodic components of the signal whilst nullifying non-periodic noise components. If the signal is periodic with each period consisting of P samples then it can be shown that

$$R_{x_1x_1}(p) = R_{x_1x_1}(p+P) \quad \text{.....(6)}$$

meaning that the auto-correlation function of a periodic function is also periodic with an identical period. Other relevant properties include it being an even function, i.e. $R_{xx}(p) = R_{xx}(-p)$, and that the greatest value of R_{xx} is always at p=0. Using these properties the period of the signal can be accurately estimated by substituting the signal with R_{xx}.

Therefore the data sequences obtained by the system were windowed with the Hamming window and then auto-correlated and the raw data was replaced with the auto-correlation function. The windowing process has the effect of tapering the data series towards its extremes with the effect that the values with larger relative lags are attenuated. This means that small perturbations in frequency will not cause a drastic degradation of the results. This procedure is known as the Blackman-Tukey method [5]. Although the potential improvements in the signal clarity are desirable the drawback with the auto-correlation process is that it increases the amount of computation required.

The following series of graphs and spectra are taken from the same point on the shaft. These show the original signal, the auto-correlation function after the data from the signal has been windowed with the Hamming window and the Fourier transform spectra of the original data after it has been windowed with the Hamming window and of the windowed auto-correlation function.

4.5.1 Results from auto-correlated data

Four sets of readings, which are plotted in Figures 4.44 to 4.47, Figures 4.48 to 4.51, Figures 4.52 to 4.55, and Figures 4.56 to 4.59, were taken from a shaft rotating at 10 Hz, 20 Hz, 34 Hz, and 61 Hz respectively. Each set of graphs shows a portion from the sample of 1024 points of the original signal taken with a sampling rate of 1.024 kHz and the auto-correlation function of the complete sample after the Hamming window has been applied to the data. The resultant frequency spectra from FFT analysis are shown for the original windowed data and auto-correlation function of the windowed data. The frequency resolution of the spectra is one Hz.

Figure 4.44, the graph of the raw data for the 10 Hz signal shows a considerable amount of surface detail with approximately 100 points captured during each period of revolution of the shaft. Figure 4.45 shows the auto-correlation function of the data points shown in Figure 4.44 after they have been windowed with the Hamming window. The auto-correlation function shows a clear peak periodically every tenth of the way along the graph. Within each period three smaller peaks, two maximum and one minimum, may be observed. These observations are confirmed by inspecting the spectra shown in Figure 4.46 and Figure 4.47. It may be seen that the amplitude of the auto-correlation attenuates rapidly at higher lags, this being due to the windowing process cutting down the end values of the data sample. Also the smaller peaks within each period cross the zero line meaning that the counting of zero crossings could not be used as a method for determining the rotational frequency with any confidence.

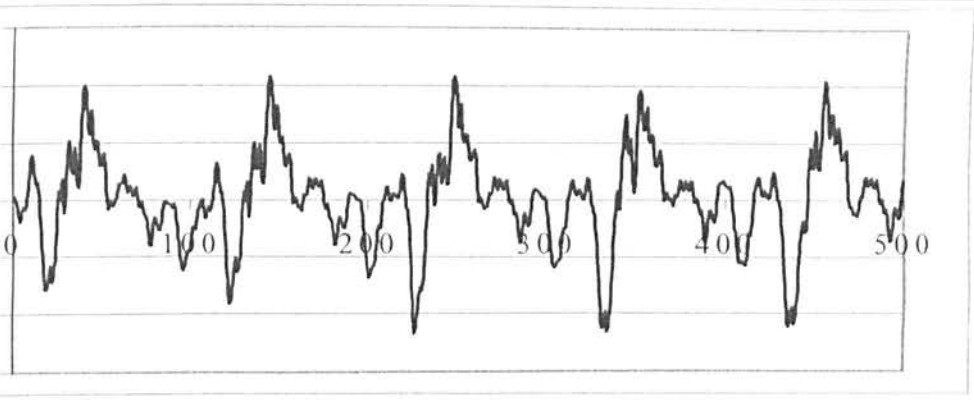

Figure 4.44 Original data, shaft rotating at 10 Hz, 500 out of 1024 points.

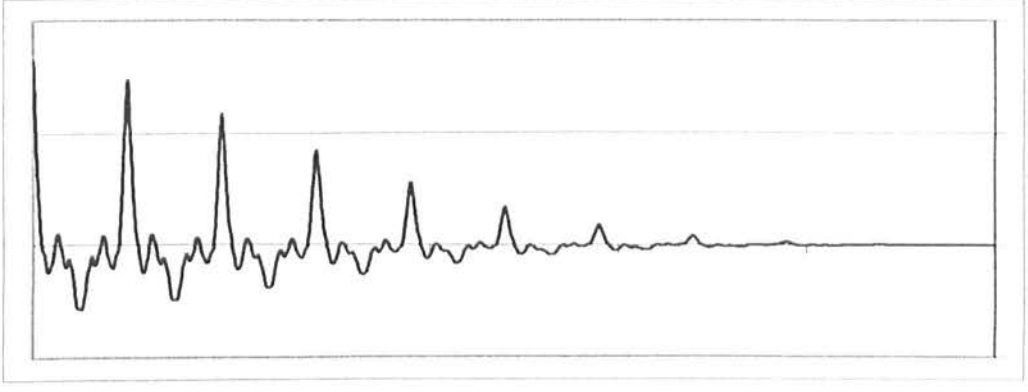

Figure 4.45 Auto-correlation function after sampling with Hamming window, 10 Hz signal.

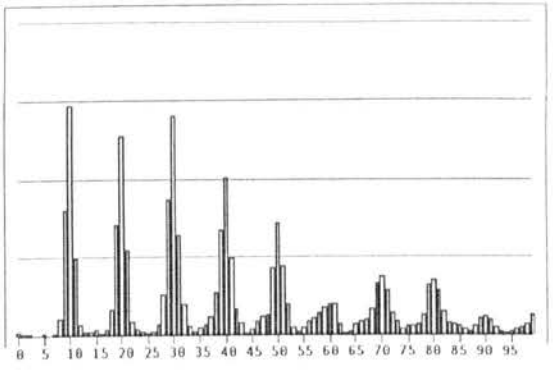

Figure 4.46 FFT spectrum, Hamming window.

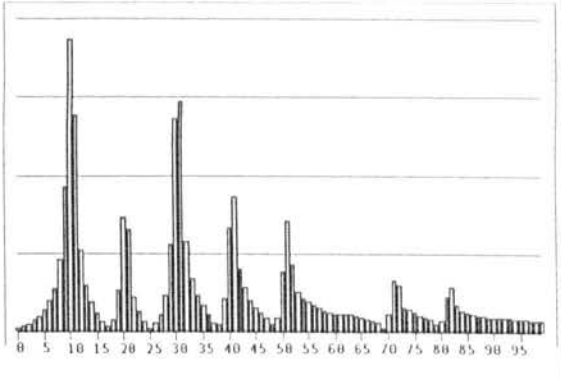

Figure 4.47 FFT spectrum of auto-correlation function after Hamming window.

Figure 4.46, the FFT spectrum of the data that has not been correlated, indicates that the power associated with the second and third harmonics is almost equal to that of the fundamental and there is a significant amount of power in the fourth and fifth harmonics. From Figure 4.47, the FFT spectrum of the auto-correlation function, shows that the second harmonic has been attenuated by a factor of two whilst the third harmonic has only been slightly reduced. The forth and fifth harmonics still contain

significant amounts of power. These results demonstrate the benefit that auto-correlation provides in enhancing the dominance of the fundamental frequency over the higher order harmonics during the FFT process.

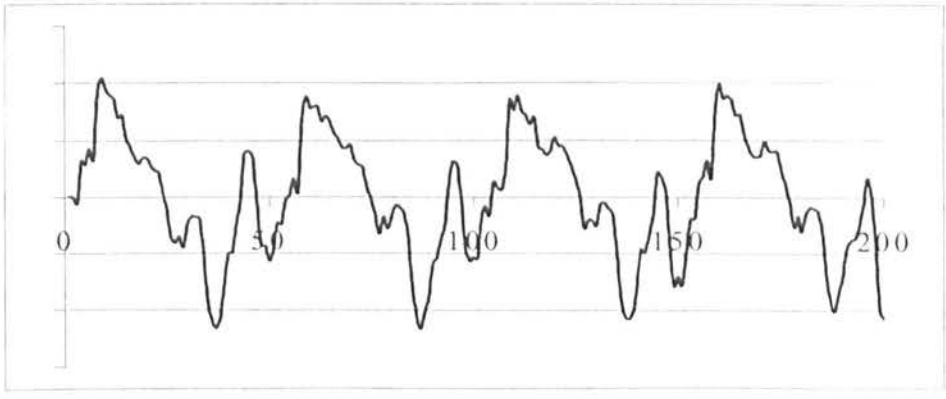

Figure 4.48 Original data, shaft rotating at 20 Hz , 200 out of 1024 points.

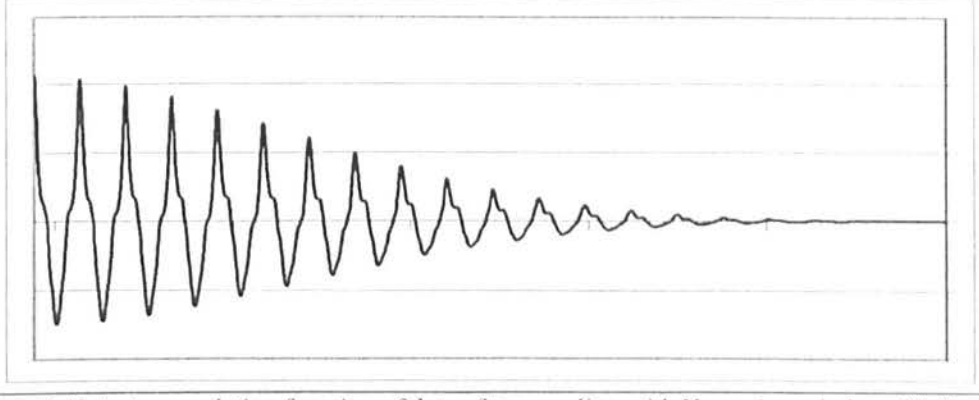

Figure 4.49 Auto-correlation function of data after sampling with Hamming window, 20 Hz signal.

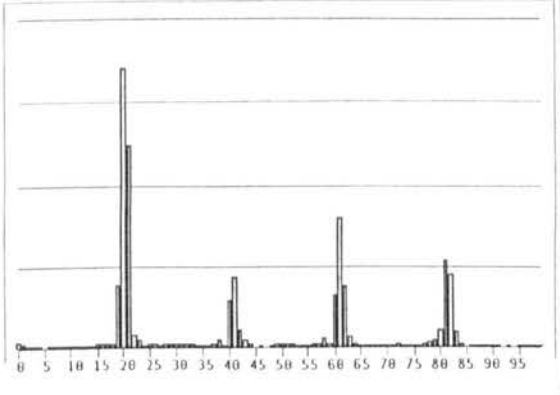

Figure 4.50 FFT spectrum, Hamming windowed data.

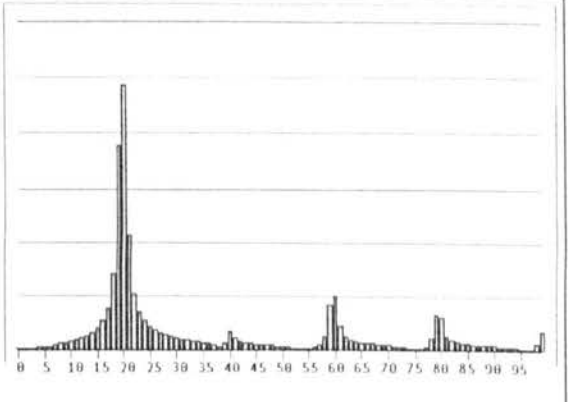

Figure 4.51 FFT spectrum of auto-correlation function after Hamming window.

Figures 4.48 to 4.51 show a similar set of graphs and FFT spectra for data captured from a graph rotating at 20 Hz. In Figure 4.48, with the same sampling rate and sample length as previously, there are now only about 50 samples per period of revolution,

meaning that less of the surface detail is visible in the graph but there are twice as many periods within the sample length. From Figure 4.49 it can be seen that there are no sub peaks in the auto-correlation function but that the peaks have a characteristic shape to them. The FFT spectra of Figure 4.50 and Figure 4.51 show that the peak of the fundamental frequency stands out clearly before auto-correlation has been carried out on the data and that the process of auto-correlation enhances the dominance of the fundamental peak further.

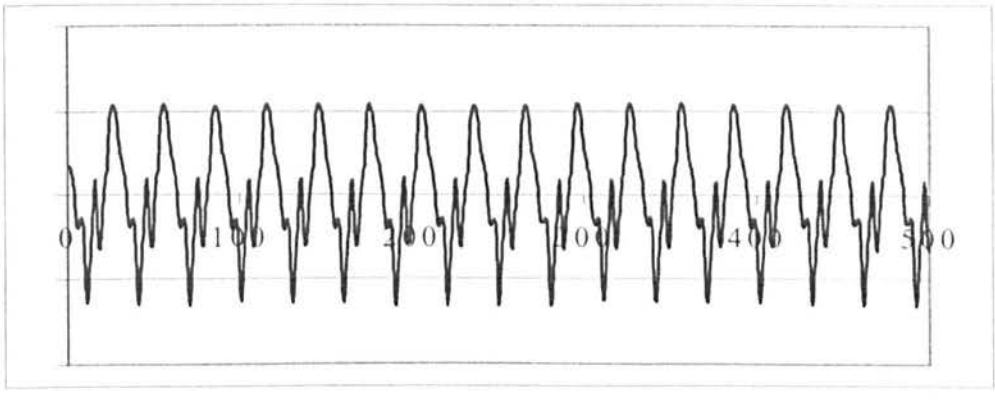

Figure 4.52 Original data, shaft rotating at 34 Hz, 500 out of 1024 points.

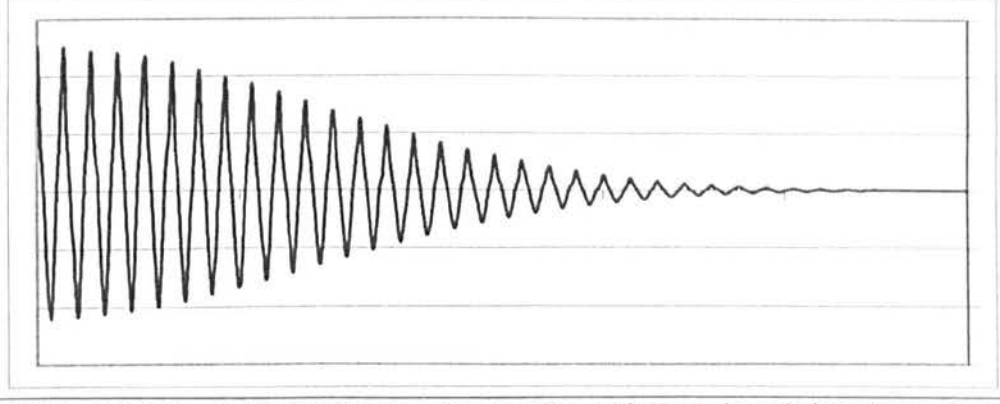

Figure 4.53 Auto-correlation function after sampling with Hamming window, 34 Hz signal

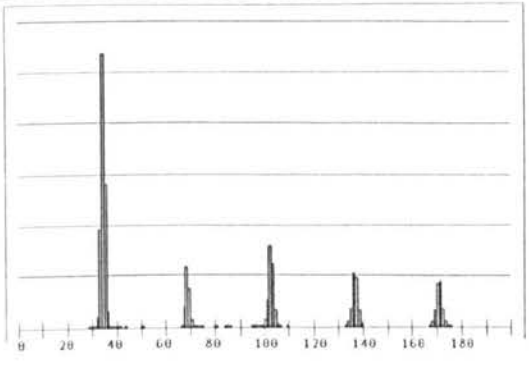

Figure 4.54 FFT spectrum, Hamming window.

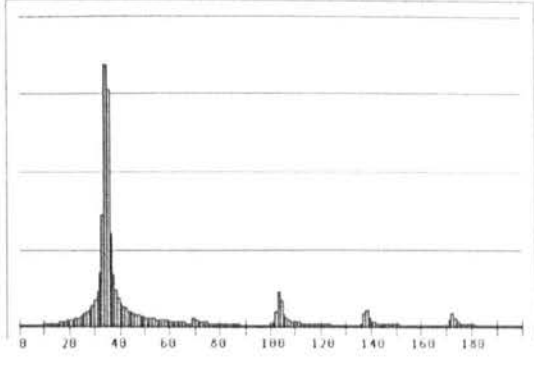

Figure 4.55 FFT spectrum of auto-correlation function after Hamming window.

Figures 4.52 to 4.55 show the results of the same processes when applied to the shaft when it is rotating at 34 Hz. The raw data shown in Figure 4.52 shows very little surface detail at all and the auto-correlation function shown in Figure 4.53 appears to be a triangular wave. This data gives the extremely dominant peaks of the fundamental frequency from the FFT spectra shown in Figures 4.54 and 4.55.

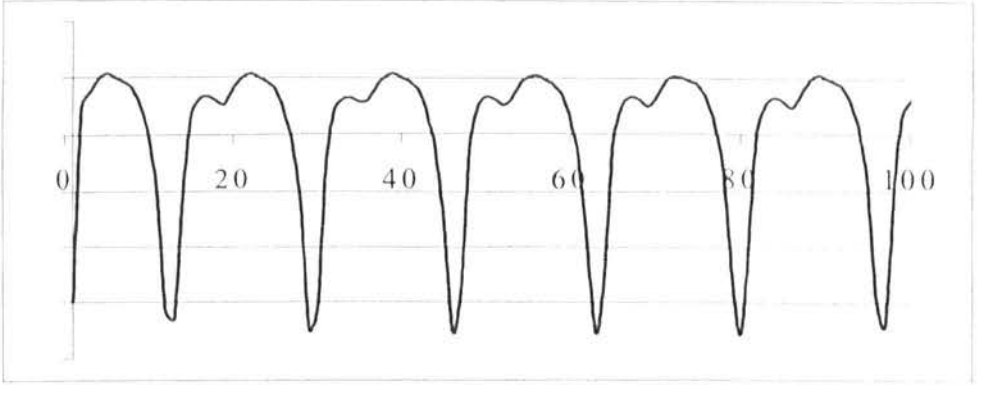

Figure 4.56 Original data, shaft rotating at 61 Hz, 100 out of 1024 points.

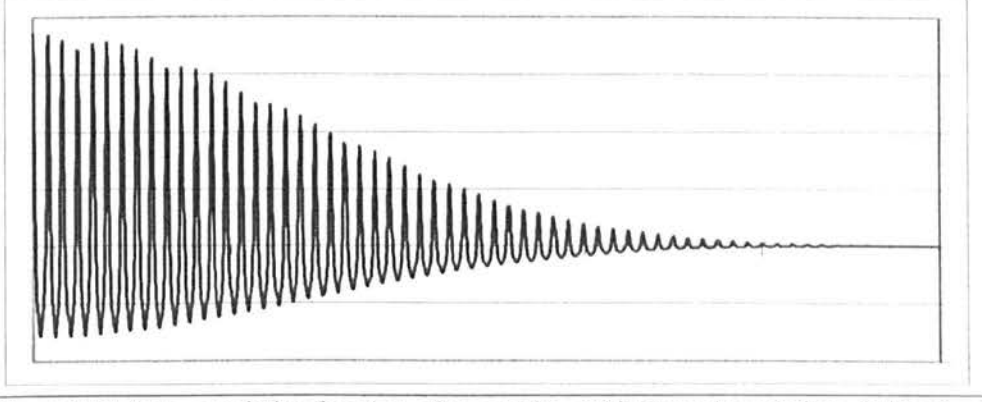

Figure 4.57 Auto-correlation function, after sampling with Hamming window, 61 Hz signal.

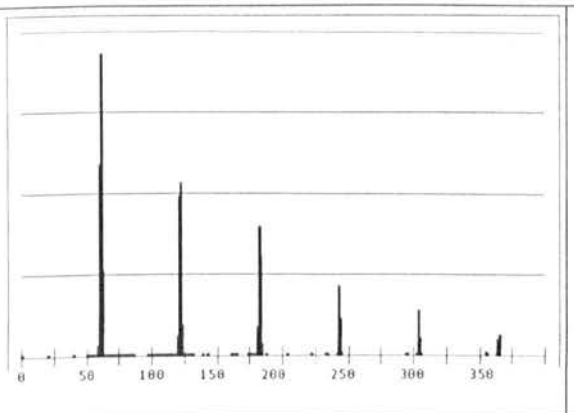

Figure 4.58 FFT spectrum, Hamming windowed data.

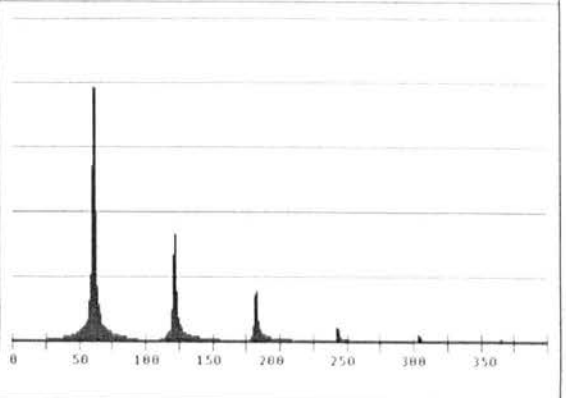

Fig 4.59 FFT spectrum of auto-correlation function after Hamming window.

The smoothing effect of capturing a low number of samples per shaft revolution is further demonstrated in Figures 4.56 to 4.59 where the shaft is rotating at 61 Hz. However due to the responsivity of the electronic detector system there is now a single sub peak in the data graph that causes the FFT spectrum shown in Figure 4.58 to show clear peak for the second harmonic. This second harmonic peak has been reduced by auto-correlation as shown in Figure 4.59.

4.6 Conclusion

A device that can accurately measure the angular velocity of rotating shafts to a resolution of one Hertz using the signal processing technique of fast Fourier transforms has been successfully developed. Different types of data sampling windows have been tested and these shown to enhance the clarity of the spectra produced by the fast Fourier transforms. The Hamming window proved to be the best window in terms of the reduction of the background noise and the maintenance of the clarity of the peaks. Auto-correlation has been shown to be a powerful technique for reducing the effects of random noise on periodic signals and for enhancing the strength of the fundamental frequency over the higher order harmonics.

4.7 References

[1] RS Datasheets, "Photodiodes", www.rswww.com, September 1995.

[2] R. D. Strum, D. E. Kirk, *First Principles of Discrete Systems and Digital Signal Processing*, Addison-Wesley Publishing, Reading Massachusetts, 1988.

[3] E. C. Ifeachor, B. W. Jervis, *Digital Signal Processing – A Practical Approach*, Addison-Wesley Publishing, Reading Massachusetts, 1993.

[4] W. H. Press, B. P. Flannery, S. A. Teukolsky, W. T. Vetterling, *Numerical Recipes – The Art of Scientific Computing*, Cambridge University Press, Cambridge, 1986.

[5] R. B. Blackman, J. W. Tukey, *The Measurement of Power Spectra*, Dover, New York, 1958.

Chapter 5

Two Channel System

5.1 Introduction to cross correlation

Cross-correlation is a statistical technique that is useful in detecting the similarity between two signals. It works by calculating the correlation coefficient between the two signals at a range of different time delays. By monitoring the position of the main peak of the cross correlation function changes in the relative phase of the two signals may also be detected. Systems based on cross correlation are used for determining the flow rate of liquids along pipes [1] and the technique has also been investigated by NASA for monitoring torque in rotating shafts [2].

The correlation of two functions is defined as follows [3]

$$R(g,h) = \int_{-\infty}^{\infty} g(\tau + t)h(\tau)d\tau \quad \text{.....(1)}$$

where g and h are the two signal data sequences being correlated. The correlation is a function of t, which is known as the lag. Figure 5.1 shows the optical set up of the two channel system. A second identical optical fibre detector channel the same as that described for the single channel system in Chapter 4 has been added and multiplexed with the original channel to the ADC so that signals from different points along the axis of the shaft may be collected and stored. The two data series may then be cross-correlated and movement in the relative position of the peaks in the cross-correlation function used to detect changes in the phase of the signals from the two points on the shaft. In the test rig frictional retarding torques of up to 0.2 Nm may be applied to the

shaft that is driven by an electric motor of maximum power 60 W and the resulting twist calculated. FFT analysis may be performed on either channel to determine the frequency of rotation.

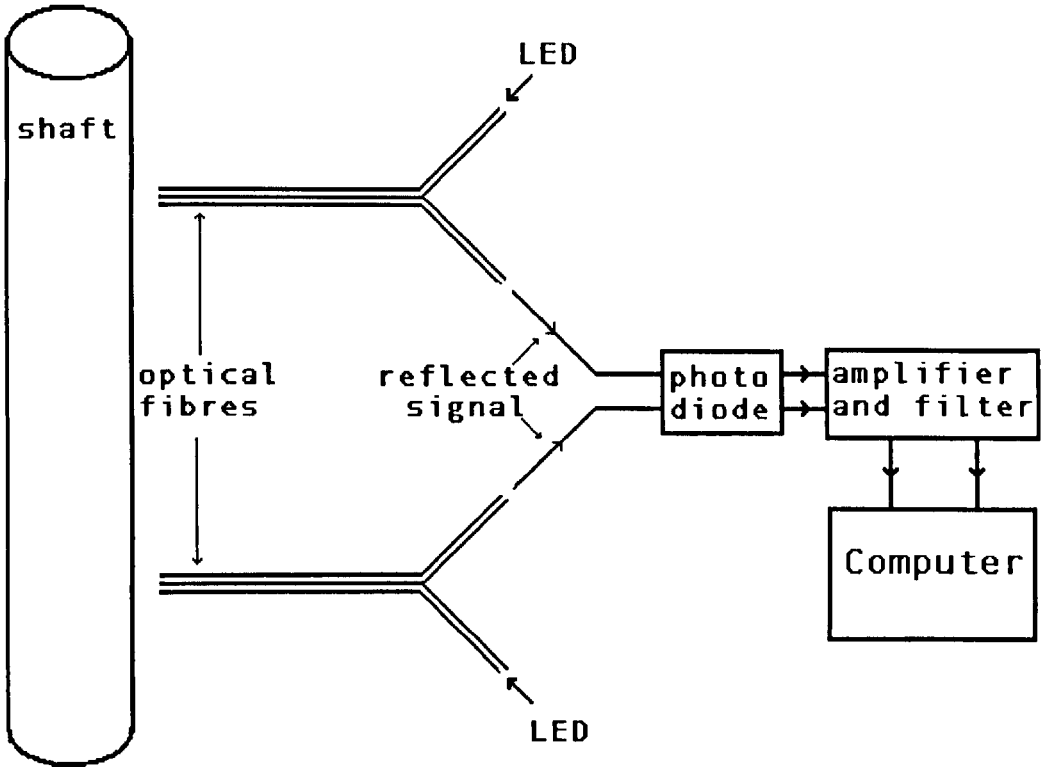

Figure 5.1 Optical arrangement of two channel system.

Due to the repeated multiplication, sum and then shift procedure of cross-correlation the process is very time consuming. Therefore the length of the two data series being cross-correlated must be shorter than those processed using FFT analysis for determining the angular velocity, in order to obtain the result in a similar time span. Since the optimum sampling decided upon for the calculation of the Fourier spectra was 1.024 kHz this value was used as the starting point for the cross-correlation calculations. As noted before the calculation of the cross-correlation functions is computationally time intensive. Using a 33 MHz 486 PC with data series of 1024

points the calculation of each cross-correlation takes five seconds, which is too long a period of time to gain an accurate picture of the shaft behaviour. The data series were reduced to 512 points, which gave a more acceptable total calculation time of one and a half seconds. This reduction in sample length signifies that if the shaft were to be rotating at 40 Hz, then approximately 20 periods of rotation would be captured in each series of data.

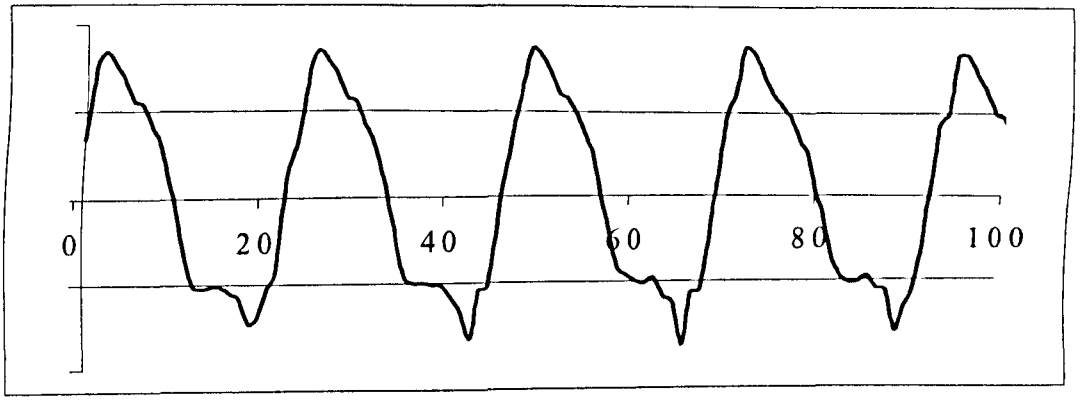

Figure 5.2 Signal 1 from shaft rotating at 43 Hz with sampling rate 1.024 kHz.

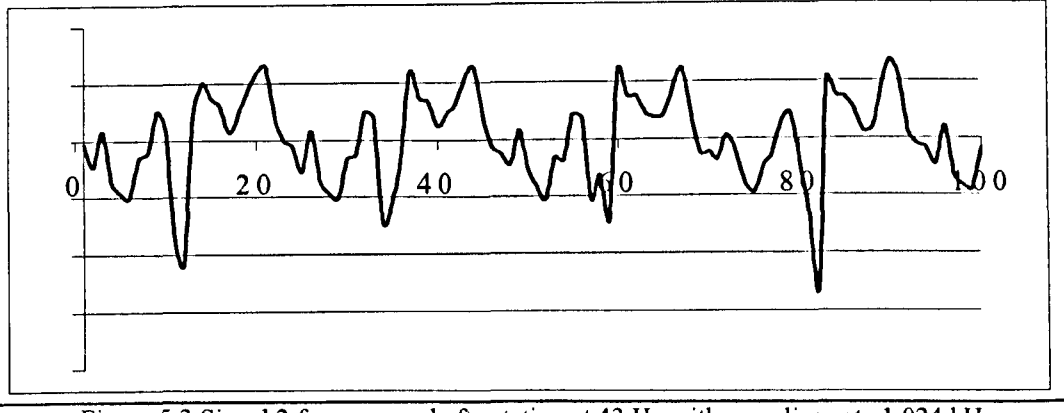

Figure 5.3 Signal 2 from same shaft rotating at 43 Hz with sampling rate 1.024 kHz.

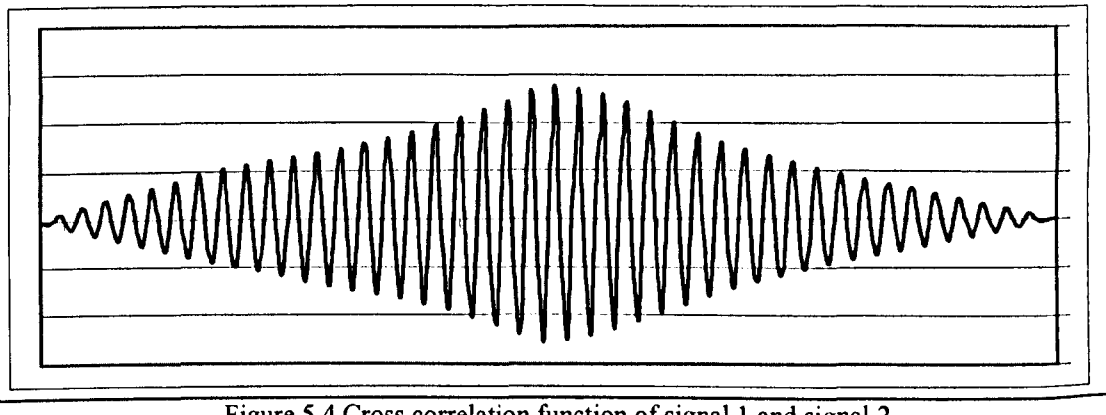

Figure 5.4 Cross correlation function of signal 1 and signal 2.

As shown in Figures 5.2 to 5.4, which show the signals from an unrestrained shaft, this results in a very clearly defined cross-correlation function but means that the system resolution for measuring twist is over 10°, which is clearly not sensitive enough. Therefore higher sampling rates were tried in order to gain a better surface resolution.

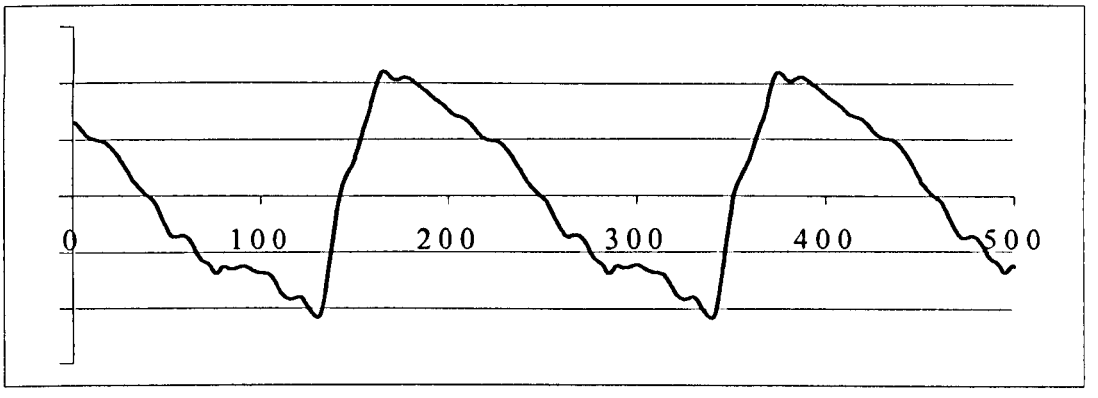

Figure 5.5 Signal 1, shaft rotating at 43 Hz, sampling rate 10.24 kHz.

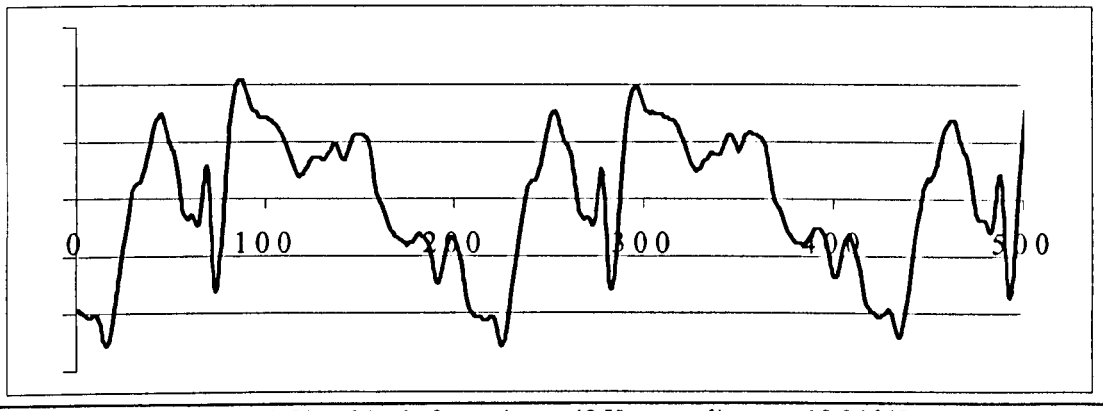

Figure 5.6. Signal 2, shaft rotating at 43 Hz, sampling rate 10.24 kHz.

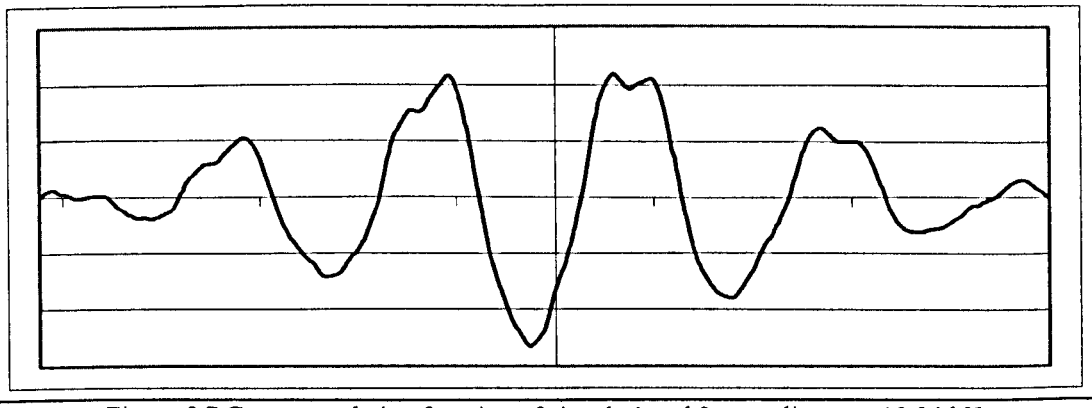

Figure 5.7 Cross-correlation function of signals 1 and 2, sampling rate 10.24 kHz.

Figures 5.5 to 5.7 show the outcome of speeding the sampling rate up to 10.24 kHz. It can be seen that signal 1 is fairly featureless whereas signal 2 reveals more detail of the surface profile. The peaks of the cross-correlation function are indistinct and equally spaced either side of the centre point of the graph. When the cross-correlation function is viewed in free running mode the shape of the peak changes continuously and the maximum point swaps between the two central points making tracking changes in phase impossible.

With the shaft rotating at about 40 Hz two and a half periods are captured per data series giving 200 points to map each revolution of the shaft. This results in a surface resolution is 1.8^{o} meaning the shaft would have to be twisted by this amount to register a one point shift in the cross-correlation function. This amount of twist would require an enormous amount of force and leaves no margin for the errors caused by the changes in shape of the peaks. To overcome these problems reflective spots were attached to the shaft at each of the sensor locations so that the signal to noise ratio is improved and so that each revolution is clearly defined by a distinct peak. Also a commercially available pliable connector was introduced between the motor and the shaft to improve the torsional displacement.

5.2 Results

The test shaft coupled using the pliable detector was restrained using a variable friction brake. Four sets of graphs, which include four graphs each, Figures 5.8 to 5.11, Figures 5.12 to 5.15, Figures 5.16 to 5.19 and Figures 5.20 to 5.23 are presented showing the effects of increased braking being applied to the shaft. The motor driving the shaft provided 40 W of power to the shaft. The outputs from the two detectors situated either

side of the coupling consisting of two series of data 512 points long, together with the complete cross-correlation function and an enlargement of the central peak of the cross-correlation function are shown.

It can be seen that the reflective spots give a clearly identifiable peak for each revolution of the shaft that results in a cross-correlation function with a distinct peak. It can be seen from the first set of graphs, which show the system under no load, that there is a slight initial phase difference between the two signals. As the torque is increased it may be observed from the graphs showing the enlargement of the cross-correlation functions that the central peak of the cross-correlation function shifts towards the left indicating that the phase shift between the two signals is increasing.

The stability of the results obtained in this set of readings was good with the exception of those taken at 0.06 Nm torque. For the readings taken from 0 to 0.04 Nm torque once the readout had settled it remained constant on one value of shift very rarely flickering by one digit up or down. In all these cases there are at least two signals from the reflective spot captured in the data series; however, in the graphs taken at 0.06 Nm torque there is the possibility that only one spot might be captured per series. If this occurs it means that the periodicity of the cross-correlation function will be uncertain therefore providing variable results.

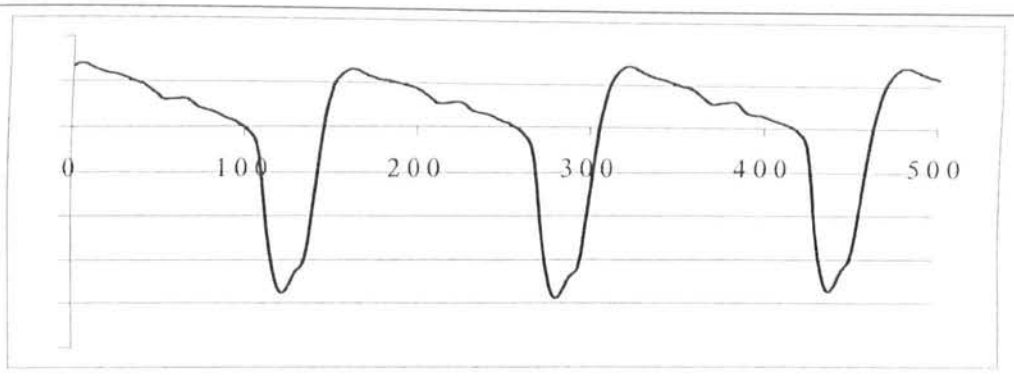

Figure 5.8 Signal 1, unrestrained shaft rotating at 65 Hz.

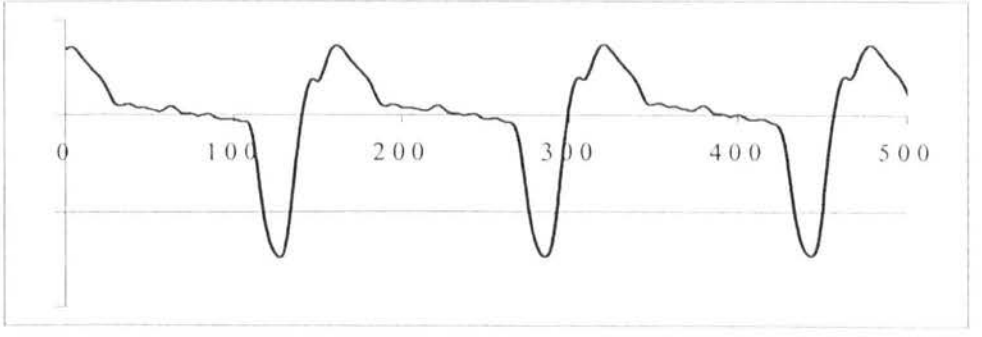

Figure 5.9 Signal 2, unrestrained shaft rotating at 65 Hz.

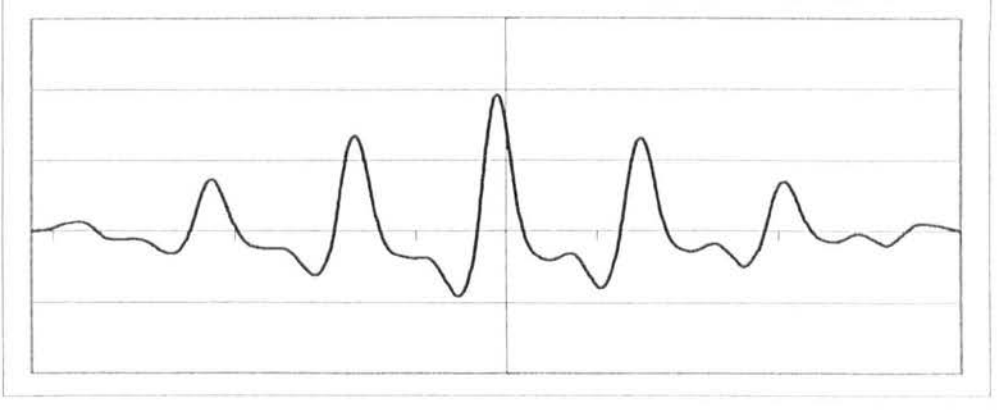

Figure 5.10 Cross-correlation function of signal 1 and 2 from shifts of +500 to -500 points.

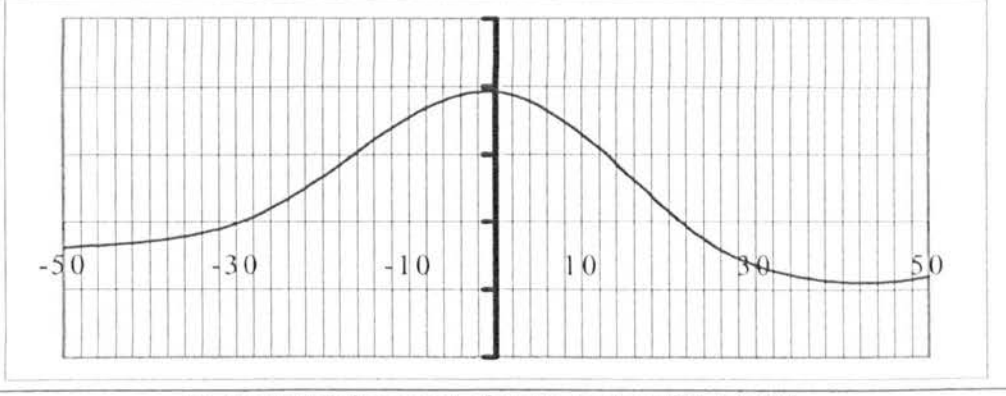

Figure 5.11 Enlargement of centre section of Figure 5.9.

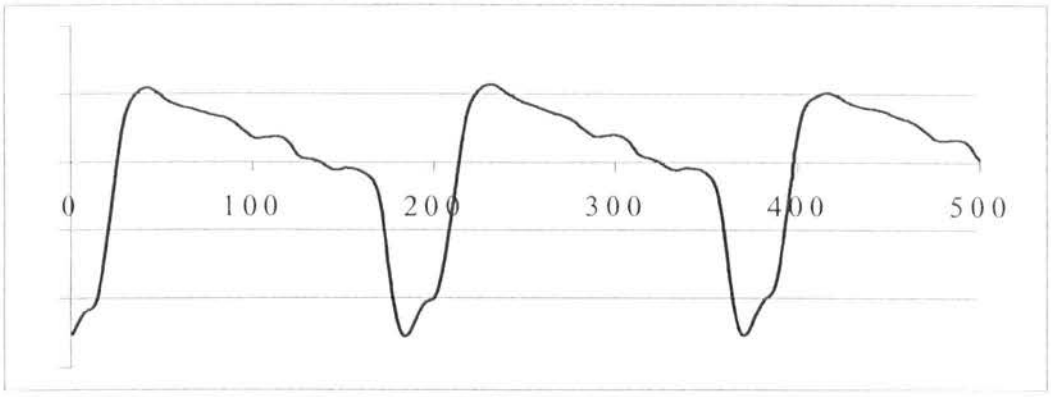

Figure 5.12 Signal 1, shaft restrained by 0.02 Nm torque rotating at 54 Hz.

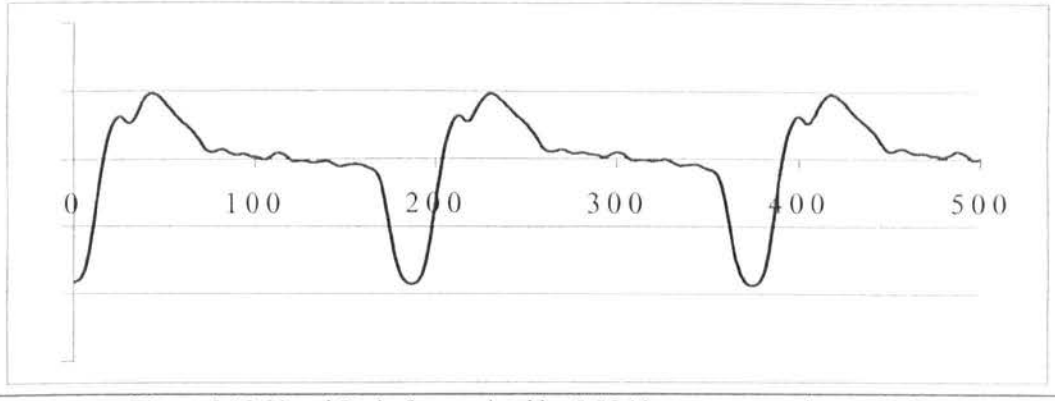

Figure 5.13 Signal 2, shaft restrained by 0.02 Nm torque rotating at 54 Hz.

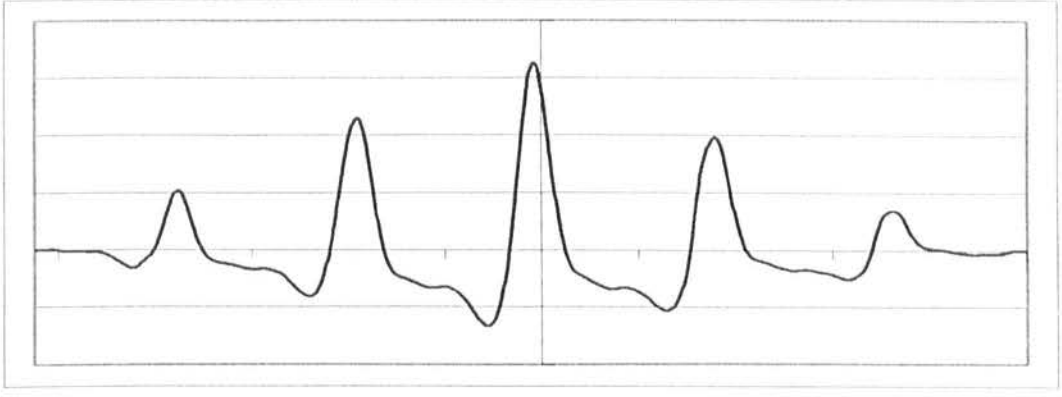

Figure 5.14 Cross-correlation function of signal 1 and 2 from shifts of +500 to –500 points.

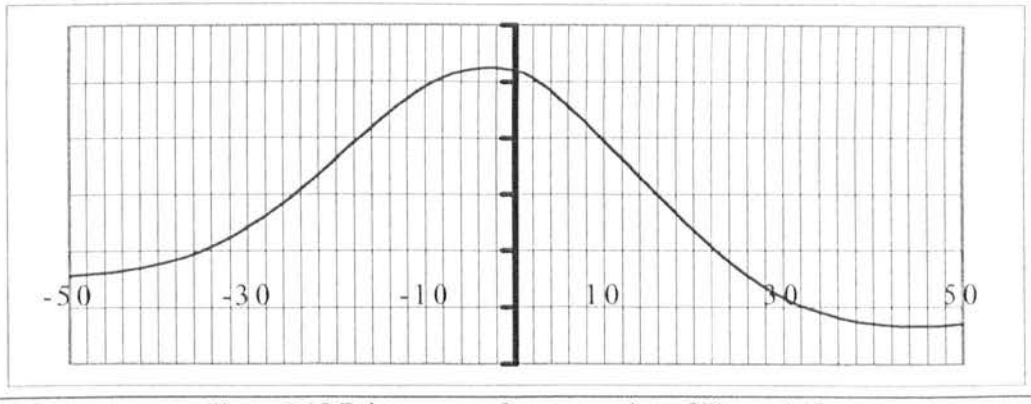

Figure 5.15 Enlargement of centre section of Figure 4.13.

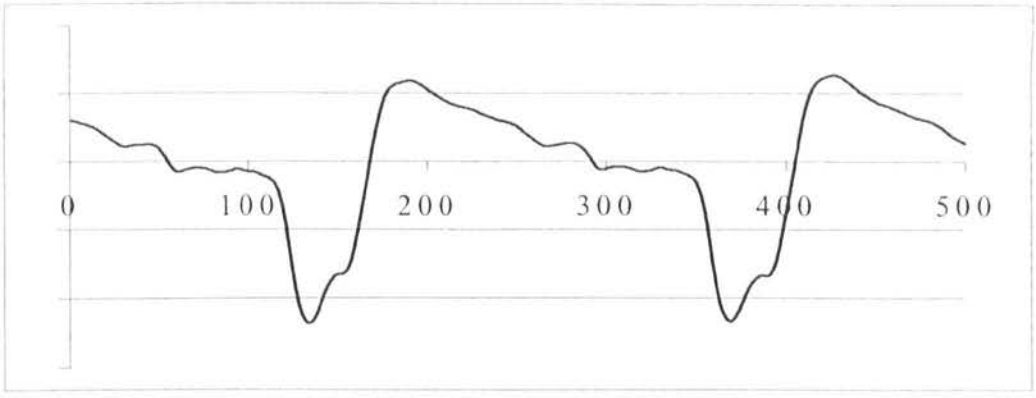

Figure 5.16 Signal 1, shaft restrained by 0.04 Nm torque rotating at 39 Hz.

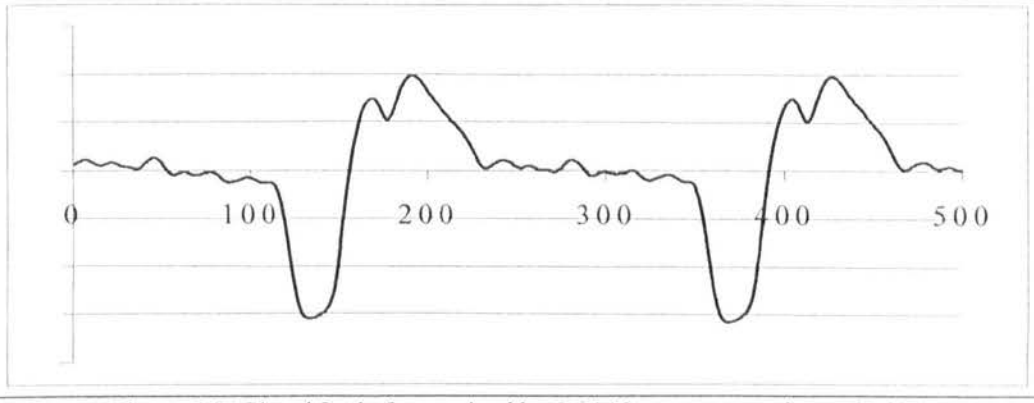

Figure 5.17 Signal 2, shaft restrained by 0.04 Nm torque rotating at 39 Hz.

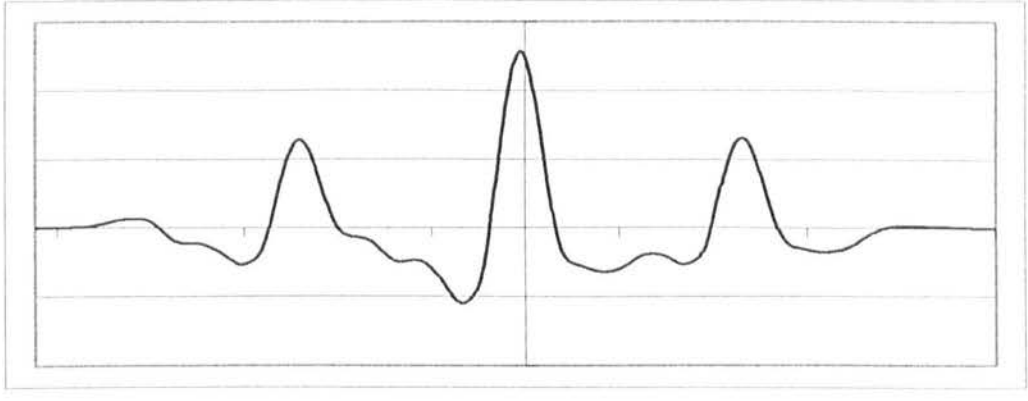

Figure 5.18 Cross-correlation function of signal 1 and 2 from shifts of +500 to –500 points.

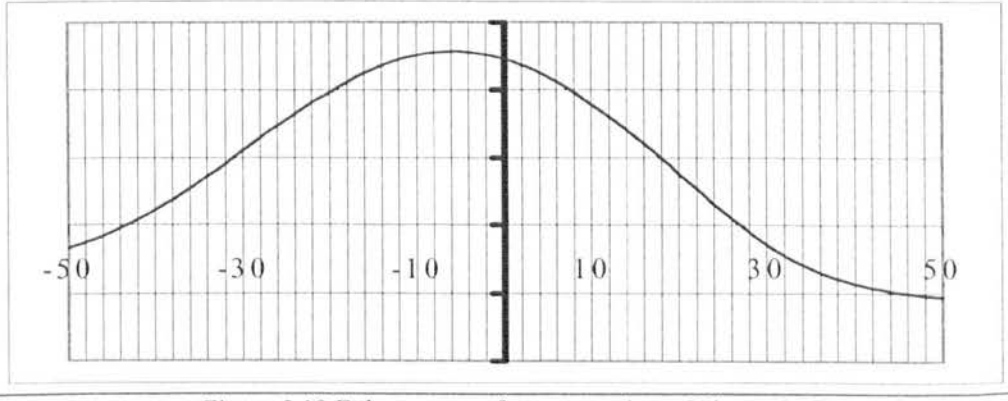

Figure 5.19 Enlargement of centre section of Figure 5.17

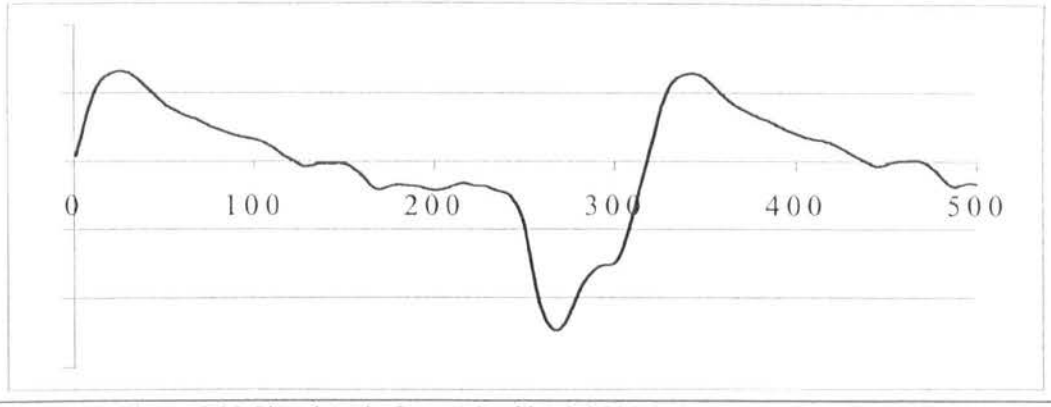

Figure 5.20 Signal 1, shaft restrained by 0.06 Nm torque rotating at 31 Hz.

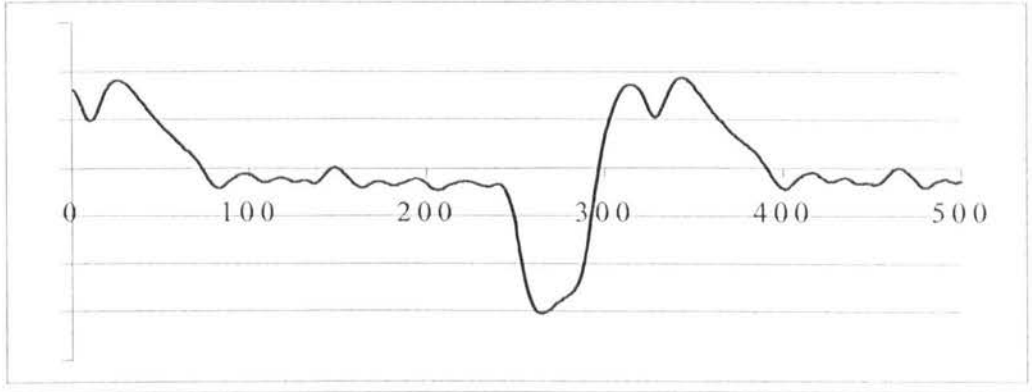

Figure 5.21 Signal 2, shaft restrained by 0.06 Nm torque rotating at 31 Hz.

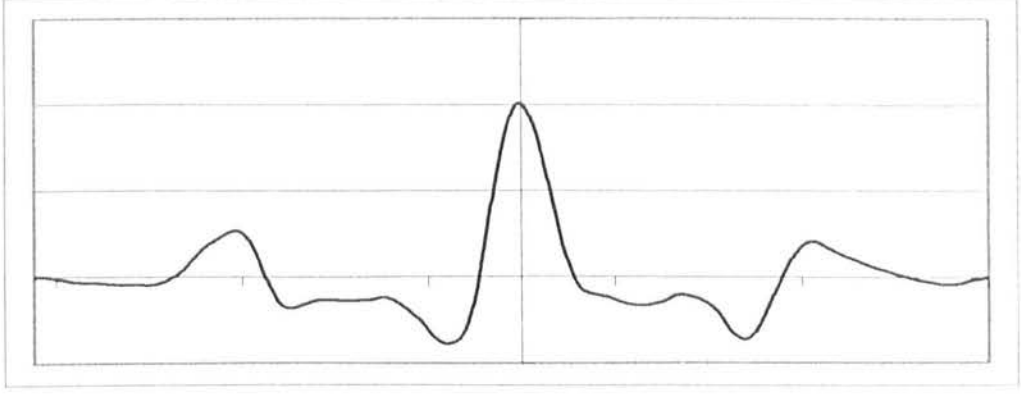

Figure 5.22 Cross-correlation function of signal 1 and 2 from shifts of +500 to -500 points.

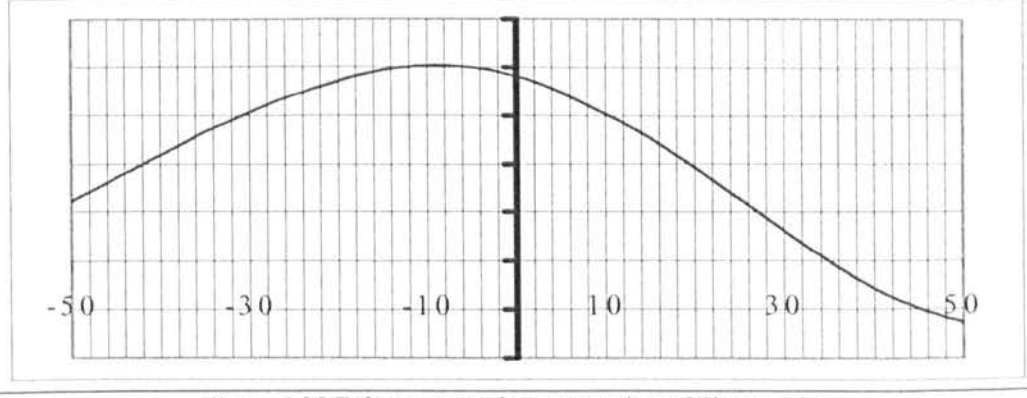

Figure 5.25 Enlargement of centre section of Figure 4.21.

Figure 5.24 shows the relationship of the twist measured against the applied torque as given in the data in Table 5.1. It can be seen the response is linear.

Torque / Nm	Speed of shaft revolution / Hz	Points per revolution	Shift (points)	Twist (°)
0	65	156.6	0	0
0.02	54	189.6	2	3.8
0.04	43	262.1	5	6.8
0.06	31	330.3	8	8.7

Table 5.1 Results obtained from data shown in Figures 5.12 to 5.23

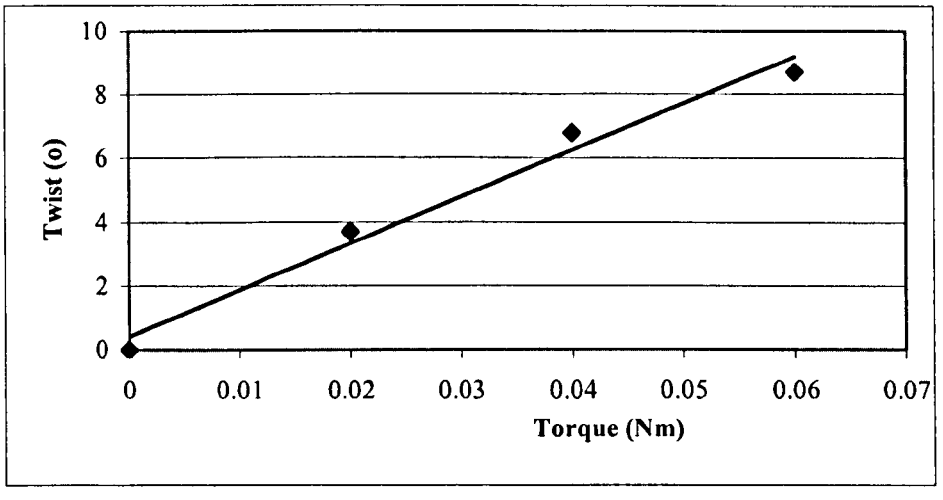

Figure 5.24 Graph of twist against torque for rotating shaft

A more extensive calibration of the system was carried out, the results of which are shown in Table 5.2. The motor was supplying 45 W of power to the shaft in this case.

Torque / Nm	Speed of shaft revolution / Hz	Points per revolution	Shift (points)	Function resolution (°)	Twist (°)
0	80.0	128.0	0	2.8	0
0.01	64.5	158.8	1	2.3	2.3
0.02	54.1	189.3	2	1.9	3.8
0.03	50.0	204.8	3	1.8	5.3
0.04	47.6	215.1	3	1.7	5.0
0.05	45.5	225.1	4	1.6	6.4
0.06	44.4	230.6	5	1.6	7.8
0.08	43.5	235.4	6	1.5	9.2
0.10	36.4	281.3	7	1.3	9.0
0.12	33.3	307.5	9	1.2	10.5

Table 5.2 Results of torque against torque calibration for rotating shaft.

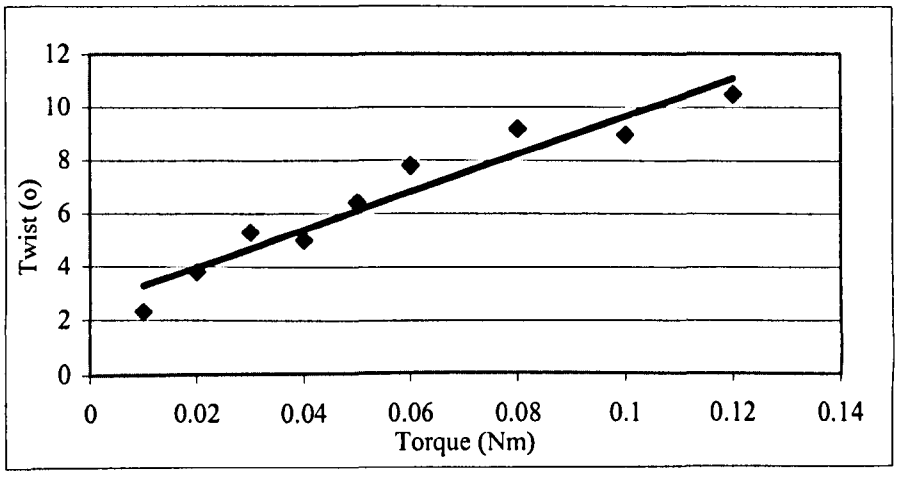

Figure 5.25 Graph of twist against torque for rotating shaft.

The graph shown in Figure 5.25 again shows good linearity. The fact that it crosses the y-axis at about 2.5° is due to slack in the coupling being taken up when the retarding force is initially applied. With the higher power being applied to the shaft the readout took longer to settle down and was less stable. It can be seen from Table 5.2 that the resolution of the cross-correlation function, especially at the higher speeds of

revolution, was about two degrees per unit shift. Since the change in the amount of shift being registered was of the order one unit from reading to reading this means there is a high uncertainty in the results.

5.3 Conclusions

It has been demonstrated that it is possible to monitor the torque versus twist relationship in a rotating shaft through calculating relative changes in the position of the peaks present in the cross-correlation function of reflected light signals taken at two points along the axis of the shaft. However, to achieve a reliable system it was necessary to introduce a flexible coupling between the drive motor and the shaft and to attach reflective spots to the surface of the shaft. For this system to function reliably at a suitable rate of update a processor with superior processing capacity and computational speed would be required. A working system was developed using a Texas Instruments TMS 320C5x DSP Starter Kit but the results were disappointing due to lack of memory and only marginally better computational speed.

The decision to add reflective spots to the shaft was made to allow the principle of using cross correlation for the monitoring of shafts to be demonstrated. However once they have been added it is simple to devise a system similar to that reported by Madzder [2] that calculates twist from changes in the time lag between the detection of the spots by the photodiodes. In such a system far greater sensitivity could be achieved by using the fastest available A to D converter since the constraints of storing data would not apply. The frequency of rotation of the shaft could be measured by timing the period of passing of one spot.

5.4 References

[1] M. S. Beck, A. Plascowski, *Cross Correlation Flow Meters: Their Design and Applications,* IOP Publishing, Bristol, 1987.

[2] G. C. Madzer, *"A fibre optic sensor for non-contact measurement of shaft speed, torque and power,"* LEW-15099, National Technical Information Center, Springfield, VA.

[3] W. H. Press, B. P. Flannery, S. A. Teukolsky, W. T. Vetterling, *Numerical Recipes – The Art of Scientific Computing*, Cambridge University Press, Cambridge, 1986.

Chapter 6

Conclusion

A versatile system using optical fibre for monitoring rotating shafts has been constructed and tested. The system is controlled by a PC and is able to display graphically in real time rotational characteristics of the shaft either in the time domain or the frequency domain. The rate of update of the display is dependent on the resolution required and a resolution of 1 Hz for the determination of frequency of rotation is achievable using FFT analysis with a response time of just over a second. The addition of a second channel enables the data from different points along the axis of the shaft to be collected and cross-correlated. Through monitoring changes in the relative phase of the cross-correlation function, the torsional displacement present in the shaft may be determined and a linear relationship between torsional displacement and torque has been obtained.

The use of windowing techniques, such as the application of the Hanning window, has also been explored in an effort to overcome limitations of the sampling process. A significant improvement in noise reduction and overall reliability of the data was observed, which tended to enhance the visibility of the fundamental peak. This effect was more pronounced at higher values of the fundamental frequency.

Algorithms were developed ab initio to extract the fundamental frequency from the observed FFT spectra when the peak of greatest energy was not necessarily that of the lowest frequency. These involved primarily establishing a correlation between the ratios of the frequencies at which the peaks occurred and possible integer values.

Checking whether these correlations lie within the possible error limits of the harmonic multiples due to the frequency resolution of the system proved to be a reliable method for establishing the fundamental frequency.

As an alternative to, and an ancillary for, the use of FFT techniques to determine the frequency of rotation the use of auto-correlation methods was explored. It was demonstrated that the use of auto-correlation prior to performing an FFT greatly enhances the visibility of the fundamental frequency of the signal.

The single channel rotational frequency device that has been developed could easily be set up for use on industrial machinery and adapted for particular shaft situations in many operating environments. The principle of operation of the dual channel device has been shown to work but greater computational processing capacity is required before a system with sufficient range for industrial purposes can be produced. Considerable effort was expended on improving the system using dedicated DSP circuitry. This work was based on a Texas Instruments TMS320C5x DSP Starter Kit and some advances were made. However, reflective spots were still required to be attached to the surface of the shaft to achieve accurate results and working with the TI Kit was not nearly as convenient as working on a PC.

The extension of the work to a dual-channel system in order to monitor angular acceleration, torsional displacement and torque was a natural progression from the work on single-channel measurement. The techniques developed for the auto-correlation of single signal are readily adaptable for the cross-correlation of two signals.

Following the introduction of a commercially available pliable connector, used with other electrically-based methods of torque measurement, a clear relationship between the braking torque and the torsional displacement was established. A resolution of approximately 2^{o} in torsional displacement was achieved, corresponding to a torque of 0.018 Nm. However, allowing the use of surface treatments, such as adding grooves or spots, permits the use of less computationally-intensive techniques based on measurements in the time domain rather than the frequency domain.

Other similar work has been reported on the remote monitoring of rotating shafts, most notably by NASA, but ours is the only system known to the author that has been reported so far for measuring rotational frequency using the naturally occurring surface profile without substantial treatment.

One of the main advantages of the work reported here is that it is, in principle, retrofittable on existing shaft-based machinery. Although in some cases minor surface treatment has taken place in order to optimise system performance, for instance the addition of painted white spots, the technique has proven its applicability with an absolute minimum of treatment of this kind. Such treatments would not be envisaged to affect the performance of the machinery adversely in any way.

It is in the field of torque measurement that I believe the greatest opportunities lie for fibre optic sensors to make advances since existing systems are generally cumbersome. The well established traditional industries are conservative and cost conscious, so whilst hazardous environments such as oil rigs appear to provide obvious applications for the use of fibre optic sensors their uptake will continue to be slow. The rapidly

expanding area of automated manufacture, especially in areas using robotics, offers a good opening for the implementation of compact, high-tech devices that can be integrated into computer controlled systems and it is here that fibre optic sensors have a bright opportunity for future growth.

Chapter 7

List of Publications

M.L.Everington and A.T.Augousti, *"A Simple Fibre Optic Shaft Monitor for Measurement of Rotational Frequency"*, Sensors and their Applications VI, Manchester, September 1993

M.L.Everington and A.T.Augousti, *"Non-contact Measurement of Rotating Shaft Characteristics"*, Applied Optics and Electro-Optics, York, September 1994.

M.L.Everington and A.T.Augousti, *"A Dual Channel Fibre Optic System for Monitoring Rotating Shafts"*, Sensors and their Applications VII, Dublin, September 1995.

M.L.Everington and A.T.Augousti, *"Remote monitoring of Angular Velocity and Torque using an Optical Fibre System"*, Applied Optics and Electro-Optics, Reading, September 1996.

M.L.Everington and A.T.Augousti, "*Non-contact Measurement of Rotating Shaft Characteristics using Optical Fibre Techniques*", Optical Fiber Technology, Vol 2, Number 4, October 1996.

Appendices

Appendix A. Computer program listings.

A.1 Single channel data capture, FFT, auto-correlation and windowing.

```
/* Use A:D converter to capture data                    */
/* Then perform FFT to determine frequency of i/p signal */

#include"stdio.h"
#include"math.h"
#include"conio.h"
#include"graphics.h"
#include"stdlib.h"

float ar[4100], wind[4100];
int no,z,n2;

void four1(float ar[], int N, int n2);
void corr1(float ar[], int N);
void readad(float ar[], int N, unsigned port);
void hanning(float ar[], int N);

main(void)
{
        int fmax, st, val, xpos, xh, xl, y, z, N;
        double avg, mean_sq_power, rms, rmsmax;
        unsigned port = 0x170;

/* Initialise graphics */

        int gdriver = DETECT, gmode, errorcode;
        initgraph(&gdriver, &gmode, "");
        errorcode = graphresult();
        if(errorcode != grOk)
        {printf("Graphics error: %s\n", grapherrormsg(errorcode));
         printf("Press any key to halt:");
         getch();
         exit(1);
        }

/* Select number of samples and transform type. */

        printf("Select number of samples?1024,2048 max:");      /* Must be power of 2 */
        scanf("%d", &N);
        printf("Choose transform or inverse(+1/-1)\n");
        scanf("%d",&n2);
        clrscr();
        setcolor(1);

/* Infinite loop broken when any key hit */

        for(;;)
        {
                if(kbhit())break;
                else
                {
                        readad(ar, N, port);        /* Open and read ADC port */

/* Apply Hanning window if required                     */

/*                      hanning(ar, N);                 */

/* Call auto-correlation routine if needed */
```

```
/*                          corr1(ar, N);                   */


/* Call FFT routine */

                            four1(ar, N, n2);
                            clrscr();

/* Calculate power at each point and plot result. */

                            rmsmax = 0;
                            for(z=1;z<=N;z+=2)
                            {
                                    mean_sq_power = pow(ar[z]/N, 2) + pow(ar[z+1]/N, 2);
                                    rms = sqrt(mean_sq_power);
                                    if (rms > rmsmax)                   /* Check for point */
                                    {                                   /* of max power    */
                                            fmax = (z+1)/2;
                                            rmsmax = rms;
                                    }
                                    setcolor(6);
                                    xpos = 20 + z;
                                    moveto(xpos, 340);
                                    lineto(xpos, (340-rms/10));          /* X1000000 for acf */
                            }
                            printf("Frequency = %4d\n", fmax-1);        /* PRINT RESULT */
                    }
            }
            getch();
            closegraph();
            return 0;
}

void readad(float ar[], int N, unsigned port)
{
            int chan, st, sum, xh, xl, y, z;
            double avg, tot;

/*** Open and read A.D port ***/

            for(z=1;z<=2*N;z++)
            {
                    ar[z]= 0.0;
            }
            outp(port+9, 0x70);
            outp(port+8, 1);
            outp(port+2, 0);
            outp(port+1, 0);
            outp(port+2, 1);
            outp(port+1, 0);
            outp(port+2, 0x00);


/* Data stored in alternate points to facilitate FFT processing*/

            for(z=1;z<=2*N;z+=2)
            {
                    outp(port, 0);
                    do{                                     /* Check for EOC   */
                            st= inp(port+ 8);               /*                 */
                    }while((st&&0x80)==0x80);               /*                 */
                    xl= inp(port+ 0);
                    xh= inp(port+ 1);
                    ar[z]= 16*xh+ xl/16;
                    sum=0;
```

```
                for(y=1;y<=92;y++)
                {
                        sum+=sum;
                }
        }

/* Subtract average to remove d.c. value */

        tot= 0.0;
        for(z=1;z<=2*N;z+=2)
        {
                tot+= ar[z];
        }
        avg = tot/(double)N;
        for(z=1;z<=2*N;z+=2)
        {
                ar[z]-= avg;
        }
}

void hanning(float ar[], int No)
{
        int z;
        float wind[4100];

/*** Calculate Hanning Window ***/

        for(z=1;z<=2*No;z+=2)
        {
                wind[z] = 0.5*(1 - cos(2*3.14159*(z-1)/(2*No)));
        }
        for(z=1;z<=2*No;z+=2)
        {
                ar[z] *= wind[z];
        }
}

void four1(float data[], int nn, int isign)
{
        int n, mmax, m, j, istep, i;
        double wtemp, wr, wpr, wpi, wi, theta;
        float tempr, tempi;


/*** Perform Fast Fourier Transform ***/

/*   Routine replaces data with its discrete Fourier transform  */

        n=nn << 1;
        j=1;
        for (i=1;i<n;i+=2)
        {
                if(j>i)
                {
                        tempr=data[j];data[j]=data[i];data[i]=tempr;
                        tempr=data[j+1];data[j+1]=data[i+1];data[i+1]=tempr;
                }
                m=n >> 1;
                while(m >= 2 && j > m)
                {
                        j -= m;
                        m >>=1;
                }
                j += m;
        }
        mmax = 2;
        while(n > mmax)
```

```
        {
                istep = 2* mmax;
                theta = 6.28318530717959/(isign*mmax);
                wtemp = sin(0.5*theta);
                wpr = -2.0*wtemp*wtemp;
                wpi = sin(theta);
                wr = 1.0;
                wi = 0.0;
                for (m=1;m<mmax;m+=2)
                {
                        for (i=m;i<=n;i+=istep)
                        {
                                j = i + mmax;
                                tempr = wr*data[j] - wi*data[j+1];
                                tempi = wr*data[j+1] + wi*data[j];
                                data[j] = data[i] - tempr;
                                data[j+1] = data[i+1] - tempi;
                                data[i]+= tempr;
                                data[i+1]+= tempi;
                        }
                        wr = (wtemp=wr)*wpr - wi*wpi + wr;
                        wi = wi*wpr + wtemp*wpi + wi;
                }
                mmax = istep;
        }
}

void corr1(float data[], int no)
{
/*** Calculate auto correlation function ***/

        int a, b, c;
        double val;
        float cor[4100];

        for(a=1;a<=2*no;a++)
        {
                cor[a] = 0.0;
        }

        for(a=1;a<=2*no;a+=2)
        {
                val = 0.0;
                for(b=1;b<=a;b+=2)
                {
                        val += data[b]*data[2*no-1-a+b];
                }
                cor[a] = val;
        }
        for(c=1;c<=2*no;c+=2)
        {
                data[c] = cor[c];
        }
}
```

A.2 Subroutine for calculating harmonic ratios

```
void base1(float harm[], double big, int N, int fmax)
{
        int fmx, m, n, nit, p, trunc, w, x, y, z;
        double min, res;
        int fq[50], fm[20];
        float resq[20];

        p=0;
        m=0;
        for(x=1;x<=N-2;x+=2)
        {       if(harm[x] < harm[x+2])                         /* look for peaks */
                {       if(harm[x+2] > harm[x+4])
                        {       if(harm[x+2] > big/10)          /* check peak for size */
                                {
                                        p= p+1;
                                        fq[p]= (x+3)/2;         /* store peak position */
                                        if(harm[x+2] > big/5)
                                        {
                                                m= m+1;
                                                fm[m]= fq[p];
                                        }
                                }
                        }
                }
        }
        for(z=1;z<=20;z++)
        {
                resq[z]= 0.0;
        }
        nit = 0;
        for(w=1;w<=m;w++)               /* Select peak and test against suceeding peaks */
        {
                if(fm(w)<fmax)                                          /* Stop if biggest peak */
                {                                                       /*      is reached      */
                        n= 0;
                        for(y=w+1;y<=p;y++)
                        {       if(fq[y] > fm[w])
                                {       trunc= fq[y]%fm[w];             /* Find remainder */
                                        res= (double)trunc/(double)fm[w];
                                        if(res > 0.5)
                                        {
                                                res= 1- res;
                                        }
                                        resq[w]+= res;                  /* Sum remainders */
                                        n+= 1;                          /*   and store    */
                                }
                        }
                        resq[w] /= n;                                   /* Divide by number */
                }                                                       /* of peaks tested  */
                nit += 1;
        }
        if(p > 1)
        {
                fmx= fm[1];
                min= resq[1];
                for(x=1;x<=nit-1;x++)
                {       if(resq[x+1] < min)             /* Find peak with smallest */
                        {                               /*   remainder quotient    */
                                fmx= fm[x+1];
                                min = resq[x+1];
                        }
                }
        }
        printf("Low com harm = %3d\n", fmx);            /* PRINT RESULT */
}
```

A.3 Double channel data capture and cross correlation.

```
/* Program to plot signals from two channels of A:D card and cross-correlate      */
/* Use A:D converter to capture data                                              */

#include"stdio.h"
#include"dos.h"
#include"math.h"
#include"conio.h"
#include"graphics.h"
#include"stdlib.h"

double ar[2050][3];
int no, z, n2, n3;
unsigned port = 0x170;
void four1(double ar[][3], int N, int n2);
void readad(double ar[][3], int N, unsigned port);
void corr1(double ar[][3], int N);

main(void)
{
        int del, fcal, fHz, fmax, val, xpos, x, y, z, N;
        double avg, mean_sq_power, rms, rmsmax, tot;

/* Initialise graphics */

        int gdriver= DETECT, gmode, errorcode;
        initgraph(&gdriver, &gmode, "");
        errorcode= graphresult();
        if(errorcode != grOk)
        {printf("Graphics error: %s\n", grapherrormsg(errorcode));
         printf("Press any key to halt:");
         getch();
         exit(1);
        }

/* Select number of samples and transform type. */

        printf("Select number of samples? 64 :");
        scanf("%d", &N);
        n2= 1;

/* Set up screen for output */

        clrscr();
        setcolor(1);

/* Initialise ar */

        for(z=0;z<=2*N;z++)
        {
                ar[z][1]= 0.0;
                ar[z][2]= 0.0;
                ar[z][3]= 0.0;
        }


        for(;;)
        {
                if(kbhit())break;
                else
                {
                        readad(ar, N, port);          /* Open and read ADC port */
                        corr1(ar, N);                 /* Call cross correlation function */
                        clrscr();
                        setcolor(5);
```

```
                        moveto(257, 400);
                        lineto(257, 0);
                        setcolor(1);
                        moveto(1, 50-ar[1][1]/100);                    /* Plot chan 1 */
                        for(z=1;z<=2*N;z+=2)
                        {
                                lineto(2*(z+1), 50-ar[z][1]/100);
                        }
                        moveto(1, 150-ar[1][2]/100);                   /* Plot chan 2 */
                        for(z=1;z<=2*N;z+=2)
                        {
                                lineto(2*(z+1), 150-ar[z][2]/100);
                        }
                        setcolor(4);
                        moveto(1, 300-ar[1][3]/10000);                 /* Plot xcf */
                        for(z=1;z<=4*N;z+=2)
                        {
                                lineto(2*(z+1), 300-ar[z][3]/1000000);
                        }
                }
        }
        getch();
        closegraph();
        return 0;
}

void readad(double ar[][3], int N, unsigned port)
{
        int chan, del, gap, nxch, sc, st, sum, w, xh, xl, z;
        int ch[2050], chx[2050];
        double avg[2], tot[2];

/* Open and read A.D port */

        for(z=1;z<=2*N;z++)
        {
                for(w=1;w<=3;w++)
                {
                        ar[z][w]= 0.0;
                }
        }
        outp(port+9, 0x70);                    /* Set for two channel */
        outp(port+8, 1);                       /*     alternate       */
        outp(port+2, 0);                       /*     capture         */
        outp(port+1, 0);
        outp(port+2, 1);
        outp(port+1, 0);
        outp(port+2, 0x10);
        do{                                    /*   Make sure     */
                st=inp(port+ 8);               /*  first channel  */
                chan= st&0x0F;                 /*  set correctly  */
        }while(chan!=0x00);                    /*                 */
        for(z=0;z<=2*N;z++)
        {
                for(w=1;w<=2;w++)
                {
                        st=inp(port+ 8);
                        chan= st&0x0F;
                        outp(port, 0);
                        do{                                    /* Check for EOC */
                                st= inp(port+ 8);              /*               */
                        }while((st&&0x80)==0x80);              /*               */
                        xl= inp(port+ 0);
                        xh= inp(port+ 1);
                        ar[z][chan+1]= 16*xh+ xl/16;
                        do{
                                st=inp(port+ 0);
```

```
                                nxch= st&0x0F;
                        }while(chan!=nxch);
                        chx[z]= xl&0x0F;
                }
                gap= 2000;                                      /* Set delay loop */
                sum=0;
                for(del=1;del<=gap;del++)
                {
                        sum+=1;
                }
        }

/* Subtract average to remove d.c. value */

        w=1;
        {
                tot[1]= 0.0;
                tot[2]= 0.0;
                for(z=1;z<=2*N;z++)
                {
                        tot[1]+= ar[z][1];
                        tot[2]+= ar[z][2];
                }
                avg[1]= 0.5*tot[1]/(double)N;
                avg[2]= 0.5*tot[2]/(double)N;
                for(z=1;z<=2*N;z++)
                {
                        ar[z][1]-= avg[1];
                        ar[z][2]-= avg[2];
                }
        }
}


void corr1(double ar[][3], int N)
{
        int n, p, z;
        double coef;

/*** Cross correlate two data channels ***/

        for(n=0;n<=4*N;n++)
        {
                ar[n][3]= 0.0;
        }
        for(p=-2*N;p<=2*N-1;p++)
        {
                for(n=1;n<=2*N;n++)
                {
                        if(n+p>2*N)
                                coef= 0.0;
                        else if(n+p<=0)
                                coef= 0.0;
                        else
                                coef= ar[n][1]* ar[p+n][2];
                        ar[p+2*N+1][3]+= coef;
                }
        }
}
```

Appendix B. Copies of published works

APPENDIX B PAGES 163 ONWARDS HAVE NOT BEEN SCANNED ON INSTRUCTION FROM THE UNIVERSITY